



Gerhard Erlacher, BSc

Feasibility Study of Temperature Measurements in Turbine Center Frames by Infrared Thermography

Master's Thesis

to achieve the university degree of

Master of Science

Master's degree programme: Mechanical Engineering

submitted to

Graz University of Technology

Supervisor:

Ao.Univ.-Prof. Dr.techn. Jakob Woisetschläger

Dott. Dott. Mag. dr Federica Farisco



Institute of Thermal Turbomachinery and Machine Dynamics

Head: Univ.-Prof. Dr.-Ing. Franz Heitmeir

This thesis was funded by LuFo, Project OPTI-TCF D-131900042

Faculty of Mechanical Engineering and Economic Sciences

Graz, December 2019

Affidavit

I declare that I have authored this thesis independently, that I have not used other than the declared sources/resources, and that I have explicitly indicated all material which has been quoted either literally or by content from the sources used. The text document uploaded to TUGRAZonline is identical to the present master's thesis.

Eidesstattliche Erklärung

Ich erkläre an Eides statt, dass ich die vorliegende Arbeit selbstständig verfasst, andere als die angegebenen Quellen/Hilfsmittel nicht benutzt, und die den benutzten Quellen wörtlich und inhaltlich entnommenen Stellen als solche kenntlich gemacht habe. Das in TUGRAZonline hochgeladene Textdokument ist mit der vorliegenden Master's Thesis identisch.

Datum/Date

Unterschrift/Signature

Abstract

Keywords: Jet Engine, Thermography, Heat Transfer

For future heat transfer measurements via thermography a feasibility study is carried out at the Transonic Test Turbine Facility (TTTF) at Graz University of Technology. The considered measuring area, the so-called turbine center frame (TCF), is located between the high-pressure and low-pressure turbine in aero-engines.

In order to measure heat transfer and surface temperatures in this section, infrared recordings of the surface covered by heating foils are made through a window. The recorded temperature fields serve as a basis for further calculations of heat transfer and film cooling, which is the subject of an ongoing dissertation.

Within the scope of this master thesis a concept for the measurement of temperature fields by IR thermography was developed. For this purpose, a simplified, yet engine representative test rig was designed and assembled using additive manufacturing processes in order to validate the planned measurements at the TTTF in advance by representative pilot tests.

The two-dimensional thermal images generated during pilot tests were transformed into a temperature field along the three-dimensionally shaped surface with the use of software routines developed in this thesis. This temperature field forms the basis for the data evaluation and the calculation of further characteristic values. The errors inherent to such a procedure are also discussed in this thesis.

All data and experience gathered in the context of this thesis will be used in the planning of the measurement at the TTTF and provided to support the ongoing dissertation.

Kurzfassung

Stichworte: Flugzeugtriebwerk, Thermographie, Wärmetransport

Für zukünftig geplante Wärmestrommessungen mittels Thermographie an der transsonischen Versuchsturbine (Transonic Test Turbine Facility TTTF) der Technischen Universität Graz wird eine Machbarkeitsstudie durchgeführt. Der betrachtete Messbereich, der sogenannte Turbinenzwischenkanal (Turbine Center Frame TCF), befindet sich zwischen Hoch- und Niederdruckturbine in Flugantrieben.

Zur Bestimmung von Wärmeübergangszahlen und zur Messung von Oberflächentemperaturen in diesem Bereich werden über einen optischen Zugang Infrarotaufnahmen, der mit Heizfolien ausgekleideten Messoberfläche, angefertigt. Diese aufgenommenen Temperaturfelder dienen als Grundlage für weitere Berechnungen von Wärmeübergang und Filmkühlung, welche in einer laufenden Dissertation behandelt werden.

Im Rahmen dieser Diplomarbeit wurde ein Konzept für die Messung von Temperaturfelder erarbeitet. Dazu wurde ein vereinfachter, dennoch der Originalgeometrie entsprechender Prüfstand unter Verwendung von additiven Fertigungsverfahren konstruiert und aufgebaut, um die geplanten Messungen am TTTF durch repräsentative Pilotversuche im Vorhinein zu validieren.

Die durch Pilotversuche erzeugten zweidimensionalen Wärmebilder wurden mithilfe von in dieser Arbeit entwickelten Softwareroutinen in ein Temperaturfeld entlang der räumlich geformten Oberfläche zusammengeführt. Dieses Temperaturfeld bildet die Basis für die Messdatenauswertung und die Berechnung weiterer Kennzahlen. Die Fehler, die ein solcher Versuchsaufbau mit sich bringt, werden ebenso diskutiert.

Alle im Rahmen dieser Arbeit gesammelten Daten und Erfahrungen gehen in die Planung der Messung am TTTF ein und werden einer aktuell laufenden Dissertation unterstützend zur Verfügung gestellt.

Vorwort

Die vorliegende Masterarbeit entstand am *Institut für Thermische Turbomaschinen und Maschinendynamik* der *Technischen Universität Graz* und wurde zwischen September 2018 und Dezember 2019 bearbeitet. Die Wahl dieser Arbeit wurde durch den umfangreichen und sehr interessanten Wahlfachkatalog des Masterstudiums Maschinenbau (Kennzahl UF 066 445) initiiert. Angebotene Lehrveranstaltungen wie „*Laser in der Schwingungs- und Strömungsmesstechnik*“ im Sommersemester 2018 motivierte mich, nach einer Abschlussarbeit im Bereich der Messtechnik zu suchen.

An dieser Stelle möchte ich mich beim gesamten Team des *Instituts für thermische Turbomaschinen und Maschinendynamik* für die herzliche Aufnahme in die Arbeitsgruppe und die tatkräftige Unterstützung bei der Erstellung dieser Arbeit bedanken. Ein besonderer Dank gilt hier meinem betreuenden Professor, Herrn **Ao.Univ.-Prof. Dipl.-Ing. Dr.techn. Jakob Woisetschläger** und meiner postdoktoralen Betreuerin, Frau **Dott. Dott. Mag. Dr Federica Farisco**, für die vielschichtigen Einblicke in die Thematik der optischen Messtechnik und dem angewandten wissenschaftlichen Arbeiten im Bereich der thermischen Turbomaschinen, sowie Herrn, **Assoc.Prof. Dipl.-Ing. Dr.techn. Emil Göttlich**, und seinem Team für die allseitige Hilfsbereitschaft und ein stets offenes Ohr bei Fragen.

Ein ganz herzlicher Dank gilt meiner Familie und meinen Freunden, allen voran meinen Eltern **Josef** und **Helga** und meiner Schwester **Andrea** – Sie alle haben mich auf meinem Weg durch das Studium begleitet und stets unterstützt.

Graz, am 12. Dezember 2019

Gerhard Erlacher

Contents

Abstract	III
Kurzfassung	IV
Vorwort	V
Nomenklatur	IX
1 Motivation	1
1.1 Modern Civil Aviation	1
1.2 Modern Turbofan Engines and their Future Technologies	3
2 Introduction	6
2.1 Turbine Center Frame	6
2.2 Objectives and Initial Situation	8
2.2.1 Infrared Camera	9
2.2.2 Optical Access	10
2.2.3 Heating Foils	11
2.3 Structure of this Thesis	12
3 Theoretical Background	13
3.1 Temperature Recording by Radiation	13
3.1.1 State of the Art	13
3.1.2 Radiation Theory	15
3.1.2.1 Radiation of Black Bodies	16
3.1.2.2 Radiation of Real Bodies	17
3.1.3 Radiometric Calibration	19
3.2 Image Processing	21
3.2.1 Pinhole Camera Model	21
3.2.2 Homogeneous Coordinates	22
3.2.3 Principal Point Offset	22
3.2.4 Camera Rotation and Translation	23
3.2.5 Finite Projective Camera	24
3.2.6 Computation of the Camera Matrix	24
3.2.7 Reprojection Error	25

3.2.8	Decomposition of the Camera Matrix	25
4	Preliminary Experiments for Thermography Postprocessing	26
4.1	MATLAB Camera Calibration Tool	26
4.2	Angular Dependency Study	29
5	Development of an IR-Image Postprocessing Routine	32
5.1	Custom-made MATLAB routine for the geometric mapping of measured infrared images	32
5.1.1	Input	33
5.1.2	Transformation	37
5.1.3	Output	38
5.1.4	Data Visualization in Tecplot	39
6	Development of a TCF Test Rig for IR Measurements	40
6.1	Mechanical Design and Construction	40
6.1.1	Requirements	41
6.1.2	Given TCF Geometry	42
6.1.3	Rapid Prototyping TCF	42
6.1.4	Defined Mounting	44
6.1.5	Cavity Replication and Wake Generator	45
6.1.6	Inlet Nozzle	47
6.1.7	Outlet	49
6.2	Assembly	50
6.3	Main Components	53
6.4	Instrumentation	56
6.4.1	Thermocouple Calibration	57
6.5	Commissioning Test	58
7	Results and Discussion	60
7.1	Transformation of two Representative IR Recordings	61
7.2	Spatial Mapping Error	62
7.3	Influence of Spatial Error on Temperature Measurement Accuracy	65
7.4	Influence of Depth of Field (DoF) in Thermography	68
8	Conclusion and Outlook	71
	List of Figures	75
	List of Tables	76



References	77
Field of View Calculator	i
Thermocouple Calibration Curves	ii

Nomenklatur

Abbreviations

ASCII	<i>American Standard Code for Information Interchange</i>
ATM	<i>Air Traffic Management</i>
ATT	<i>Advanced Thermal Technologies</i>
CC	<i>Combustion Chamber</i>
CFD	<i>Computational Fluid Dynamics</i>
CoC	<i>Circle of Confusion</i>
CORSIA	<i>Carbon Offsetting and Reduction Scheme for International Aviation</i>
DLT	<i>Direct Linear Transformation</i>
DoF	<i>Depth of Field</i>
ECU	<i>Electronic Control Unit</i>
FAA	<i>Federal Aviation Administration</i>
FDM	<i>Fused Deposition Modeling</i>
FLIR	<i>Forward Looking InfraRed</i>
FoV	<i>Field of View</i>
FTIR	<i>Fourier-transform infrared spectroscopy</i>
GTF	<i>Geared Turbofan</i>
GUI	<i>Graphical User Interface</i>
HPC	<i>High-pressure Compressor</i>
HPT	<i>High-pressure Turbine</i>
ICAO	<i>International Civil Aviation Organization</i>
IEC	<i>International Electrotechnical Commission</i>
IR	<i>Infrared</i>
ITTM	<i>Institut für Thermische Turbomaschinen und Maschinendynamik</i>
LDV	<i>Laser Doppler Velocimetry</i>
LPC	<i>Low-pressure Compressor</i>
LPT	<i>Low-pressure Turbine</i>
LuFo	<i>Luftfahrtforschungsprogramm</i>
MTU	<i>Motoren- und Turbinen-Union</i>
PIV	<i>Particle Image Velocimetry</i>
SESAR	<i>Single European Sky Air Traffic Management Research</i>
STL	<i>Stereolithography</i>

TCF	<i>Turbine Center Frame</i>
TC	<i>Thermocouple</i>
TSFC	<i>Thrust-specific Fuel Consumption</i>
TTTTF	<i>Transonic Test Turbine Facility</i>

Physics Constants

σ	Stefan-Boltzmann constant	$5.67032 \times 10^{-12} \text{ W m}^{-2} \text{ K}^{-4}$
b	Wien constant	$2.8977685 \times 10^{-3} \text{ m K}$
c	Speed of light in vacuum	299792458 m/s
h	Plank's constant	$6.62607 \times 10^{-34} \text{ J s}$

Symbols

α	<i>Absorptivity</i>	$[-]$
λ	<i>Wavelength</i>	$[m, \mu m, nm]$
K	<i>Calibration matrix</i>	$[-]$
P	<i>Camera matrix</i>	$[-]$
ν	<i>Frequency</i>	$[\text{Hz}]$
Φ	<i>Flux (power)</i>	$[W]$
ρ	<i>Reflectivity</i>	$[-]$
τ	<i>Transmissivity</i>	$[-]$
ε	<i>Emissivity</i>	$[-]$
B	<i>Calibration constant</i>	$[K]$
F	<i>Calibration constant</i>	$[V]$
U	<i>Calibration constant</i>	$[-]$
e	<i>Energy</i>	$[J]$
M	<i>Radiant emittance</i>	$[W m^{-2}]$
λ	<i>Spectral radiation emittance</i>	$[W m^{-2} \mu m^{-1}]$
M_λ	<i>Wavelength</i>	$[m, \mu m, nm]$
T	<i>Temperature</i>	$[K, ^\circ C]$
U	<i>Sensor signal</i>	$[V]$
λ	<i>Wavelength</i>	$[m, \mu m, nm]$

1 Motivation

1.1 Modern Civil Aviation

For more than hundred years, the world of aviation has been driven by ongoing innovation. The evolution and constant improvement in the field of aviation can be seen in every branch of it, including materials, engines, airframes, controls and airline business models. In the early stages of aerospace engineering around the 1920s, the principal drivers of innovation have been speed, range and capacity [30]. However, at the beginning of the 1990s, these initial targets were all reached in one form or another, and the boundary conditions of innovation have started to shift in the direction of economical and environmental interest. Eversince, the transportation of passengers and cargo worldwide have been rising steadily.

Despite continuous efficiency optimizations of aircraft engines over time, the transport growth has been rising disproportionately. Figure 1.1 summarizes the evolution and increase of air traffic, showing the associated emissions of greenhouse gases over the last 50 years. Nowadays, commercial aviation consists of about 13% of all CO₂ emission from the transport sector, which is about 2% of the global CO₂ emission (Figure 1.2). The continuously growing commercial air transportation sector is part of the uprising climate change aswell and sets new challenges, not only regarding carbon emission, but also with respect to nitrogens oxied, particles and noise.

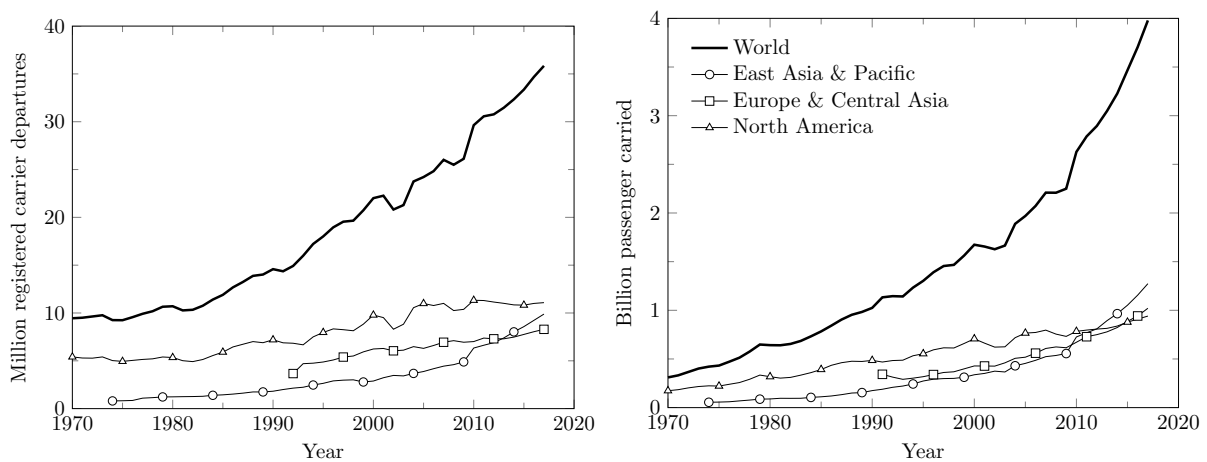


Figure 1.1: World Air Traffic Growth. Registered carrier departures worldwide (left) and passengers carried worldwide (right). Data provided by [19] and [18].

In the interests of climate protection, several initiatives have been launched in recent years to define a longer-term climate protection strategy for aviation. These include:

- ICAO CORSIA [20]
- SESAR including the European ATM Master Plan [2]
- FAA NextGen [11]
- CleanSky [5]
- ...

The visions and objectives of these initiatives have different aspects. Above all, ensuring sustainable development of aviation. Especially, ICAO mandates that the growth of international aviation shall be CO₂-neutral from 2020 on. The overarching ambition is that all aviation stakeholders will participate at this global undertaking.

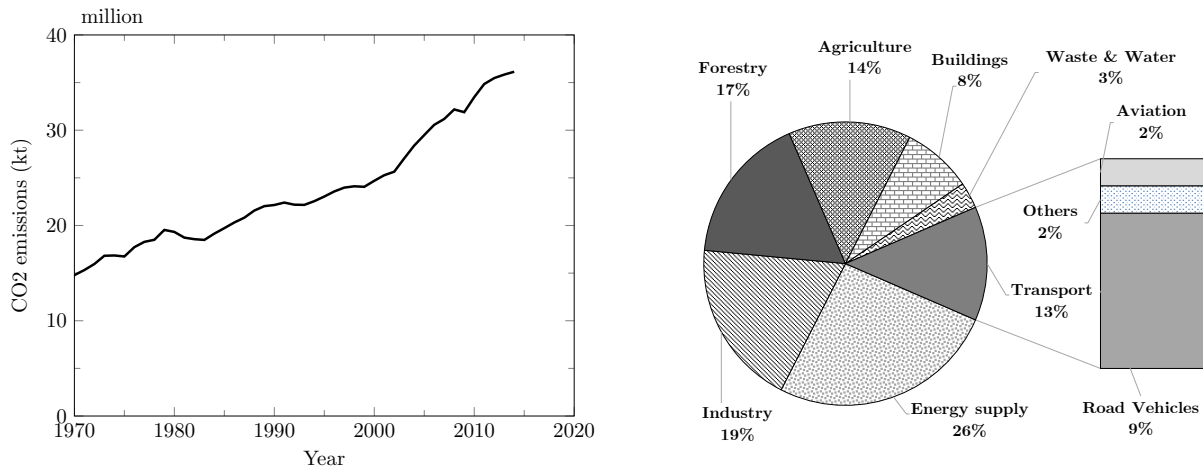


Figure 1.2: Global CO₂ Emission. Carbon dioxide produced during consumption of solid, liquid, and gas fuels and gas flaring worldwide (left) and global CO₂ emissions per sector (right). Data provided by [21] and [22]

1.2 Modern Turbofan Engines and their Future Technologies

As described in Section 1.1, future requirements regarding pollutants and noise challenge engine manufacturers. The aim is to reduce specific fuel consumption by about 20 to 25% by 2020. These targets can only be achieved through new key technologies.

The reduction of the pollutant emission of an engine essentially means a reduction in NO_x and CO_2 emissions. Cutting CO_2 emissions is directly proportional to the fuel reduction, which is achieved either through a higher thermal efficiency by means of higher component efficiencies, or by means of a higher overall pressure ratio of the engine circuit process together with a higher turbine inlet temperature.

Nowadays, the temperatures of modern engines in the combustion chamber and turbine inlet are far above the melting temperatures of the materials used. In order to withstand these high temperatures, blade cooling in the first high-pressure stages is essential. The cooling air is extracted from the compressor. The correct adjustment of the required cooling air is an important factor for efficiency. Since the production of NO_x in the combustion process rises rapidly at temperatures above 1900 K, turbine inlet temperature can be increased only within limits.

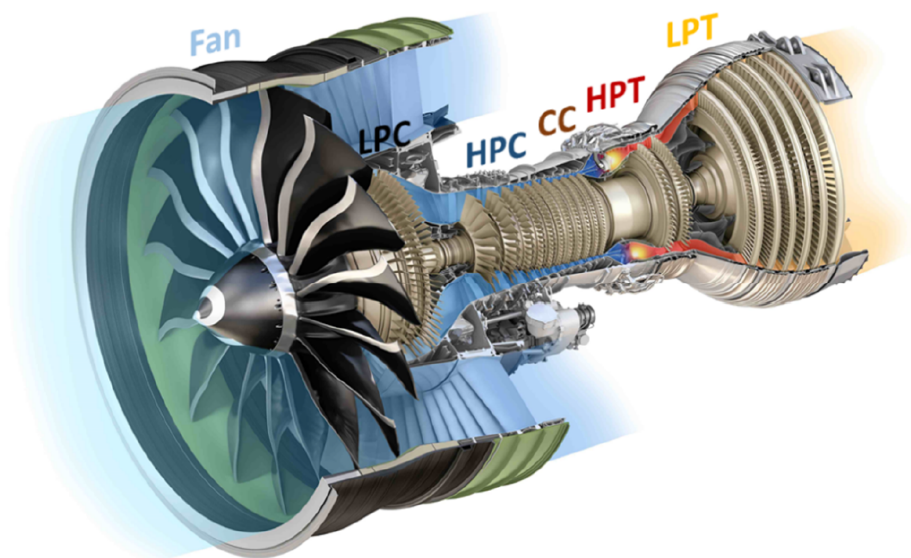


Figure 1.3: Modern two-shaft high-bypass turbofan engine GE9X [3], image adapted from [39]

Figure 1.3 shows the main components of a modern turbofan engine. It is a high bypass ratio two-shaft engine. The bypass ratio is defined by the ratio of the air mass flow through

the fan (outer secondary circuit) to the air mass flow through the core engine (inner primary circuit). [4] The engine consists of a combustion chamber (CC), a downstream two-stage high-pressure turbine (HPT) driving the high-pressure compressor (HPC), and a co-rotating six-stage low-pressure turbine (LPT) driving the low-pressure compressor (LPC) and the fan. [39]

The basis for further improvements in engine efficiency is a high propulsion efficiency, which can only be achieved through a high bypass ratio. On the basis of the engines shown in Figure 1.4 the trend of ongoing development work can be seen.

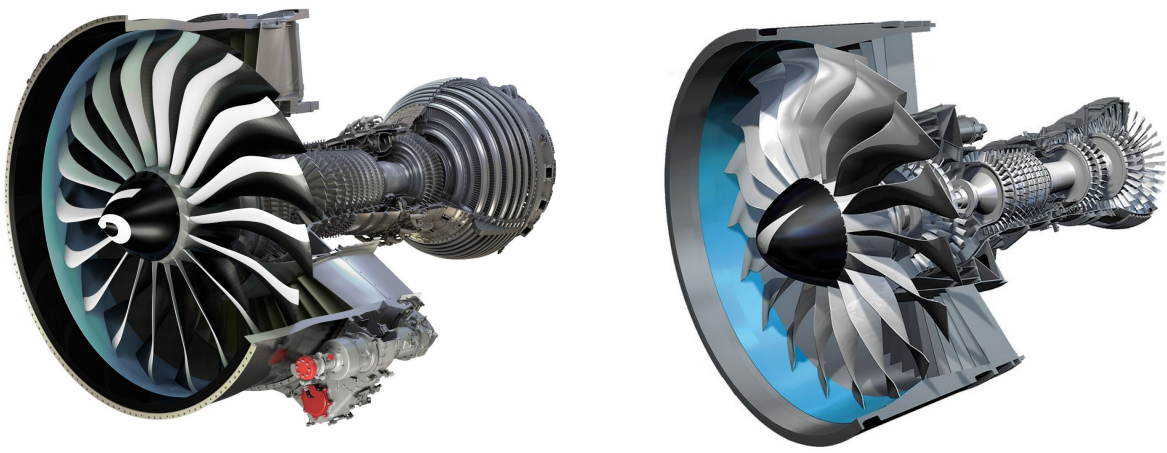


Figure 1.4: Modern engine concepts. CFM LEAP-X (Advanced Turbofan) (left) and PW1000G (Geared Turbofan) (right). Images courtesy of [24] and [29]

Table 1.1: Modern engine concepts. Data from [8] and [9]

Model	CFM LEAP-1A	PW1100G
Manufacturer	GE, Safran Aircraft Engines	International Aero Engines
Configuration	Twin-spool, high-bypass turbofan	high-bypass geared turbofan
Compressor	1 fan, 3-stage LP, 10-stage HP	1 geared fan, 3-stage LP, 8-stage HP
Turbine	2-stage HP, 7-stage LP	2-stage HP, 3-stage LP
Bypass ratio	11:1	12:1
Speed Limits LPR	3894 rpm	10047 rpm ¹
Speed Limits HPR	19391 rpm	22300 rpm
Fan diameter	198 cm (78 in)	206 cm (81 in)
Take-off thrust	106.8 to 143.05 kN	147.28 kN
Weight	2990 kg	2857.6 kg
Introduction	August 2016	January 2016
Unit cost	USD 14.5 million	USD 12 million
Application	A320neo family	A320neo family

¹The Fan Speed (NFAN) is directly proportional to the LPR speed by a gear ratio of 1:3.0625.

A promising concept for very high bypass ratios is the so-called Geared Turbofan (GTF), where the fan is connected to the low-pressure shaft by a gear box. This allows much higher speeds of the low-pressure compressor and the associated low-pressure turbine, which ultimately leads to a larger overall pressure ratio in the core engine. The fan and the LPT can operate closer to their optimum speed range. One advantage of the high-speed LPT is the greatly reduced number of stages. This shortens the overall length and reduces the number of parts. One disadvantage is the loss in the planetary gear, which must be dissipated by an additional cooling system.

Figure 1.5 schematically shows the relationship between fuel consumption and noise development of the two previously mentioned engine concepts. The possibilities of the GTF are clearly demonstrated. Although larger diameter geared engines have a better Thrust-specific fuel consumption (TSFC), they will have higher fuel burn due to weight and drag penalties.

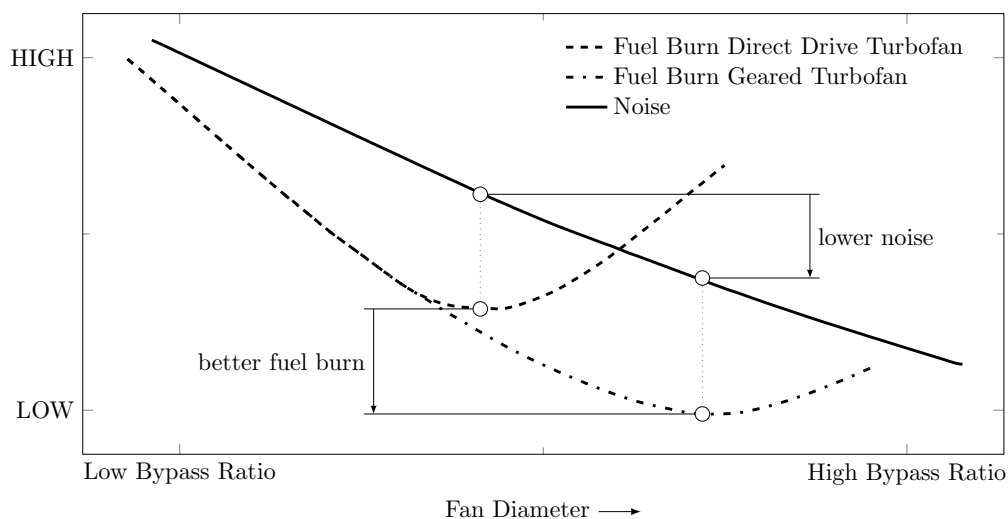


Figure 1.5: Conventional Propulsion System Fundamentals. Image adapted from [7]

2 Introduction

2.1 Turbine Center Frame

The Turbine Center Frame (TCF) is located between the high-pressure turbine (HPT) and the low-pressure turbine (LPT) (Figure 2.1 & 2.2) and performs two important functions. "It connects the high-pressure shaft's rear bearing with the housing and forms an aerodynamic transition duct between the high-pressure and low-pressure turbine." [17]

A TCF essentially consists of two main components [17]:

- The so-called Hub-Strut-Case is the supporting structure and represents a housing with several support struts. They, in turn, hold the hub in which the bearing is located.
- The strut casing, also called flowpath hardware, forms the flow channel for the hot gas from the high-pressure turbine. Additionally, there are a variety of seals, oil lines and cooling air lines that lead air and oil through the TCF to the turbines and bearing.

Research work on the TCF engine component is one of the main tasks at the *Institute of Thermal Turbomachinery and Machine Dynamics* at *Graz University of Technology*. In cooperation with manufacturers, flow-theoretical phenomena are analyzed by simulation and measurement technology at the Institute's Transonic Test Turbine Facility (TTTF). The TTTF is able to generate full flow similarity in transonic gas turbine stages due to a 3 MW compressor station. Conventional measurements can be carried out using pressure and temperature sensors, but optical methods such as laser Doppler velocimetry (LDV), particle image velocimetry (PIV) and thermography can also be used. The focus here is to study the behaviour of these components with the aim to increasing the efficiency of the turbofan engine. [25]

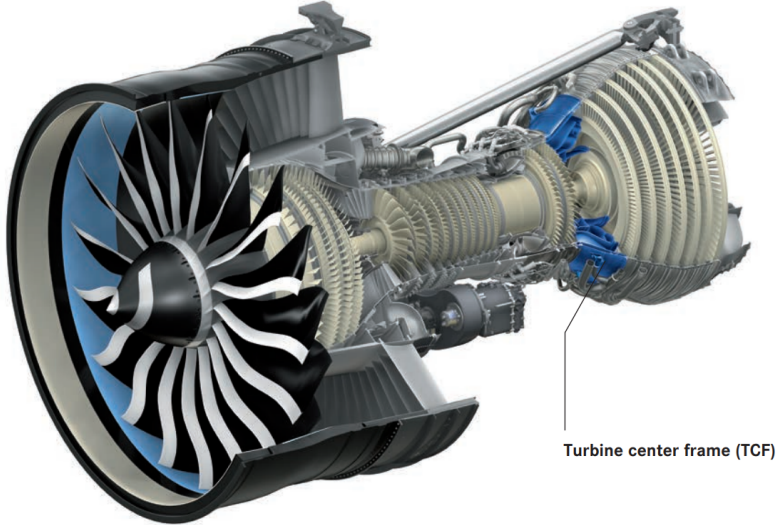


Figure 2.1: GE90 engine. Location of the TCF highlighted in blue. Image courtesy of MTU Aero Engines[28]

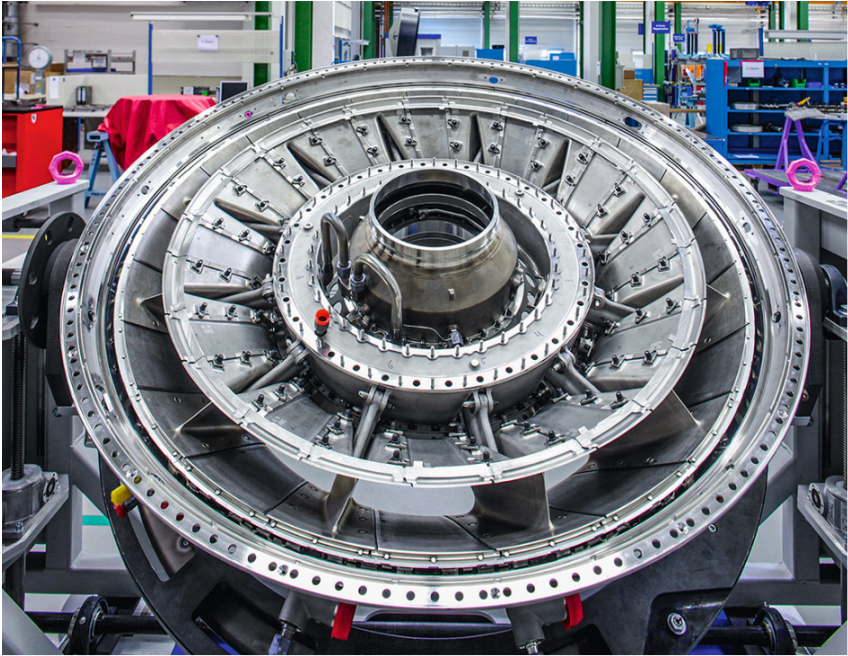


Figure 2.2: Turbine Center Frame. Assembly of a GE90 Turbine Center Frame for the Boeing 787 Dreamliner at MTU Munich. Image courtesy of MTU Aero Engines [17]

2.2 Objectives and Initial Situation

The overall objective of this thesis is to develop a feasibility study for future planned heat flux and film cooling measurements in a turbine centering frame (TCF) component using thermography.

The work was initiated within the framework of the LuFo V3 OptiTCF project [6] and is intended to create the boundary conditions for the measurement methodology through preliminary tests. The knowledge gained will serve as the basis for the planned measurements at the Transonic Test Turbine Facility (TTTF) at the *Institute of Thermal Turbomachinery and Machine Dynamics*. As previously mentioned, this work creates a framework for measurements.

Specifically, the aim of this thesis is to provide the hardware for the experimental execution of temperature measurements in a TCF and to implement a measurement methodology for surface temperatures with their data evaluation.

As a starting point of the examination contained in this thesis, several constraints have been defined, including the geometry and material of the optical access to the turbine intermediate channel, the available thermographic camera. The use of heating foils in the defined measuring region had already been discussed before the realization of this work.

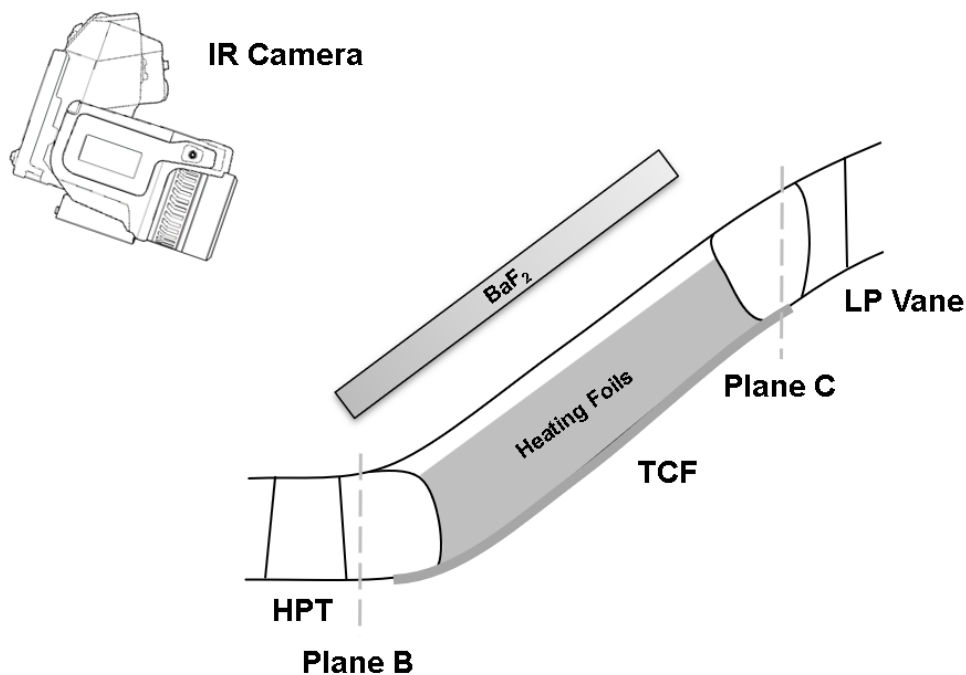


Figure 2.3: Schematic initial specification. Turbine Centering Frame (TCF) with its characteristic S-shaped duct located between the HPT rotor and the LP stator vane. Optical access via BaF₂, Heating foils in the measuring zone.

The concept of temperature measurement in the flow duct via heated foils with constant heat flux on the strat wall needed to be tested for feasibility. Data for the design of these heating foils were collected in advance by our project partner through CFD simulations in the TCF area and communicated to the manufacturing company ATT Advanced Thermal Technologies. In addition, it was necessary to develop processing algorithms for the captured temperature images. Figure 2.3 schematically shows the initial plan for the experiment with the above mentioned components.

2.2.1 Infrared Camera

For the acquisition of the surface temperatures the handheld infrared camera *T650SC* by *FLIR* with a resolution of 640×480 is used (Figure 2.4). The camera is equipped with an *uncooled microbolometer* detector type and the spectral range is 7.5 and $14\mu m$. The camera has an integrated 18 mm lense which is leading to a field of view of approximately $25^\circ \times 19^\circ$. The most important specifications are summed up in Table 2.1.

Table 2.1: Camera specifications provided by [13].

Manufacturer	Flir Systems Inc.
Model	T650SC
Detector Type	Uncooled Microbolometer
Spectral Range	$7.5 \div 14 \mu m$
Operating Temperature Range	$-15^\circ C$ to $50^\circ C$
Camera f-number	f/1.0, Integrated Lens $18 mm(25^\circ)$
Detector Pitch	$17 \mu m$
Field of view (FOV)	$25^\circ \times 19^\circ$
Frame Rate	30 Hz
Resolution	640×480
Accuracy	$\pm 1^\circ C$ or $\pm 1\%$ of reading for limited temperature range for measuring object within $-15^\circ C$ to $120^\circ C$ and ambient temperatures of $10^\circ C$ to $35^\circ C$
Bump/Vibration	25 g (IEC 60068-2-29) / 2 g (IEC 60068-2-6)



Figure 2.4: FLIR TC650SC. High resolution handheld infrared camera. Image courtesy of FLIR systems

2.2.2 Optical Access

The decision for the material of the optical access was already made in advance of this thesis. Barium fluoride (BaF_2) is optically transparent over a wide wavelength range from ultraviolet to infrared, which is why it is commonly used in IR measurement technology. Figure 2.5 shows different materials and their transmission behavior over the wavelength range and the dependence of the transmission on the thickness of the optical material. In the current case, the covered wavelength range of the camera from $7.5 \div 14 \mu\text{m}$ (see section 2.2.1) in the far infrared range was taken into account and barium fluoride was selected as the material.

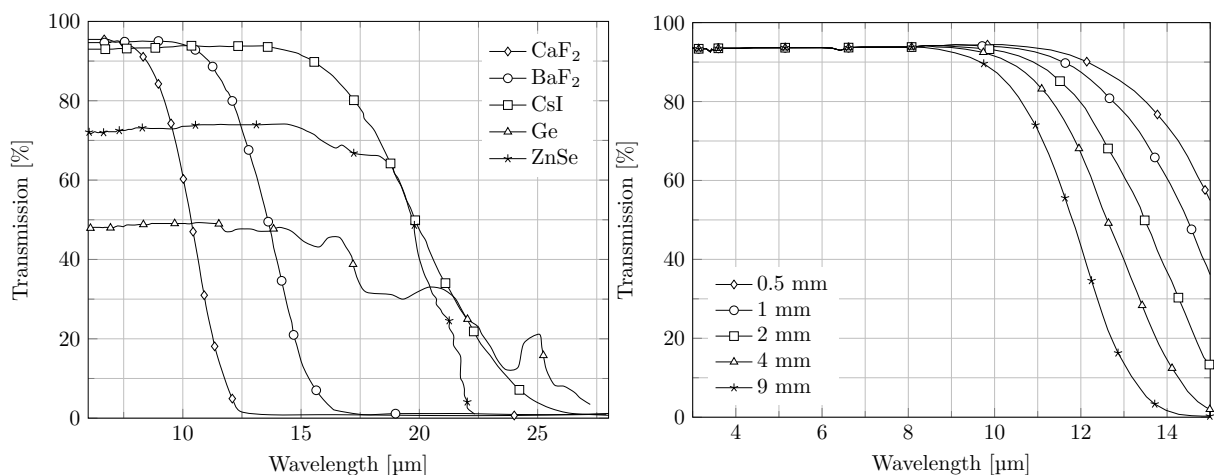


Figure 2.5: Spectral transmission of optical materials. Transmission FTIR spectra for 2 mm thick windows of CaF_2 , BaF_2 , CsI , Ge and ZnSe (left) and transmission curves of BaF_2 windows with different thickness (right). Data provided by [35] and [34]

2.2.3 Heating Foils

The heating foils were developed by ATT Advanced Thermal Technologies. At the beginning of the work several options of heating foils for the use in the planned test procedure had already been discussed with the help of the manufacturer's experience. The development happened parallel to this thesis. Figure 2.6 shows the structural design of the heater, whereby the top layer (a) was selected for thermographic measurements according to the later application in the course of this thesis. The coating was applied internally as recommended by the manufacturer. This special paint from Nextel (NEXTEL[®] Velvet-Coating 811-21 [26]) has particularly good emissivity properties. Furthermore, the emissivity of this coating is almost constant in a wide angular range. The rough coating is extremely sensitive to contamination and external mechanical influences and should therefore be treated as carefully as possible.

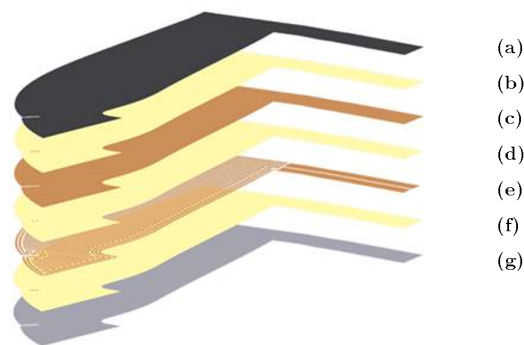


Figure 2.6: Structural design of the heater. (a) Black coating $10\mu m$, (b) Coverlayer (Polyimide) $50\mu m$, (c) Heat dissipation layer (copper) $35\mu m$, (d) Substrate (Polyimide) $50\mu m$, (e) Heating meander (copper) $35\mu m$, (f) Coverlayer (Polyimide) $50\mu m$, (g) Adhesive $200\mu m$

2.3 Structure of this Thesis

This work is divided into a theoretical and a constructive or experimental part.

The theoretical part is again divided into two chapters and is intended to reflect the necessary basics of radiation in the context of thermography. On the other hand also an insight into the used theory of coordinate transformations for the applied image processing is given. It is a compact summary of the correlations, without long derivations and proofs, that can be taken from the referenced literature.

The second part contains the work and results carried out. It deals with the development of the measurement methodology for thermographic measurements in a TCF and the test bench built within the scope.

The work concludes by summarizing the findings.

3 Theoretical Background

3.1 Temperature Recording by Radiation

3.1.1 State of the Art

Nowadays, thermographic recordings are often used in industries. Modern systems can provide important information for the user quickly and without effort. The range of available devices spreads from simple handheld units for common usage to high-performance cameras for complex research purposes. The following list summarizes the broad spectrum of thermographic applications: [23][14]

- **Building thermography.** Thermal imaging is used to diagnose and improve the energy efficiency of buildings. It can detect thermal bridges, air leaks, moisture intrusions and other information. Since the provision of heat for living space accounts for a very large proportion of the energy consumed, an increase in efficiency is of great importance.
- **Material testing.** Infrared thermography as a non-destructive testing method can detect various defects. It is used for stress analysis, crack detection or to detect delaminations and water inclusion in composites.
- **Security applications.** Thermography is also used for various safety applications like observation, search and rescue, border control or facility protection.
- **Monitoring and inspection.** Thermal imaging can be implemented in production cycles to support quality assurance, optimize processes or to observe safety margins in real time.
- **Medical applications.** The measurement of body temperature and its distribution has always been an indication tool for people's health. The non-contact and non-invasive thermography is used for various application in medicine.
- **Spectral thermography.** Spectral IR thermography allows material specific precision measurements. Emissivity and transmissivity vary in the infrared spectrum. The focus of the IR measurements on spectral ranges allow the detection of special regions and effects. For example, background radiation can be filtered or areas with

a very high or low transmission can be located. This method is often used for flame investigations.

- **High-speed infrared imaging.** The possibility of recording rates of modern high-speed devices up to 10.000 frames per second opens new doors for thermography. "Research applications exist in the areas of ballistics, supersonic projectiles, explosives, combustion processes, lasers, and more." [14, p.5]
- **Infrared microscopy.** Modern systems also operate in the micro-region and are able to accurately measure temperature on targets down to 3 microns. An industry in which micro thermography is mainly used is electronics. According to *Moore's law*, the number of transistors on integrated circuit chips doubles every two years [27]. Complex electronic assemblies are becoming ever more powerful and smaller, so that thermal management is becoming increasingly important in their development.

Infrared thermography has been used as a tool for many research investigations regarding Thermo-Fluid-Dynamics. One major challenge in the field of turbomachinery is the experimental thermographic measurement of complex fluid flows. The evaluation of wall convective heat fluxes in fluid flows leads to a better understanding of fluid dynamics phenomena, such as flow separation or instability and help to achieve highest efficiencies in modern aerodynamic systems. Thermal measurements by means of thermography are very error-sensitive, since external influences can strongly affect the measurements. In order to carry out accurate measurements, appropriate measuring methods must be developed.

A recently introduced measurement methodology, so-called "**Thermoblitz**", recently introduced by the Bundeswehr University Munich and supported by the joint program AG TURBO and MTU Aero Engines is one innovative example. [37] This transient infrared measurement method allows the non-contact and two-dimensional representation of heat transfers in boundary layers. Thermal energy is brought into the surface of an object by a short light pulse. The subsequent temperature decay is recorded with a high temporal resolution by an infrared camera and a quantity proportional to the heat transfer is calculated. By means of a suitable calibration, not only qualitative processes but also quantitative statements should be possible. A large potential of the measuring method is the possible applicability in hard-to-reach and rotating systems in order to characterize flow field behaviour, e.g. in turbines.

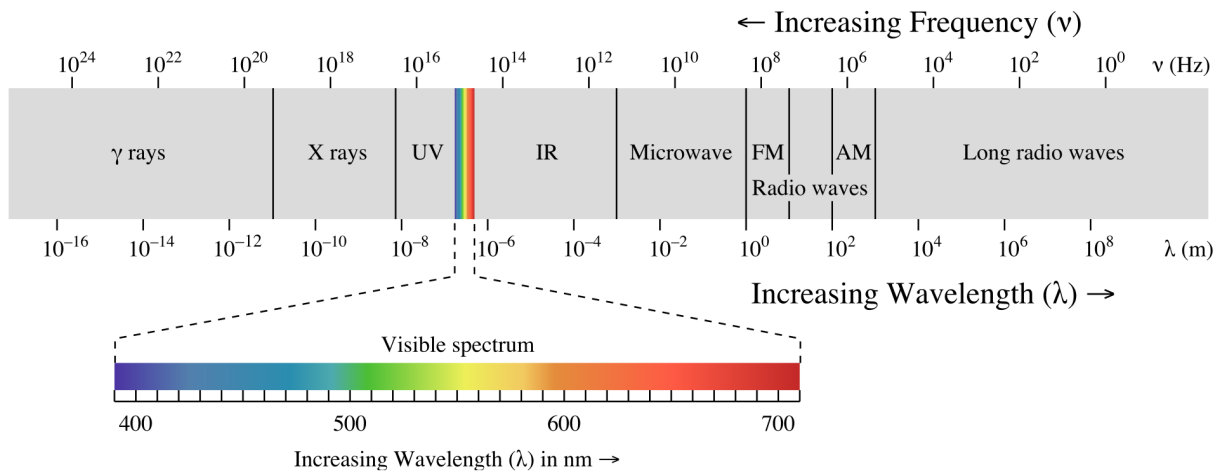


Figure 3.1: The electromagnetic spectrum. Image courtesy of [32]

3.1.2 Radiation Theory

Energy transmission occurs in the form of conduction, convection or radiation. In this chapter, the focus is on heat transferred by radiation. This energy transport mechanism is based on emission of electromagnetic waves. Any material, solid, liquid or even gas emits electromagnetic waves at a temperature above the absolute zero. Heat transferred by radiation does not require a transport medium as conduction or convection. Energy can even be exchanged between two unconnected bodies in absolute vacuum by means of photon transport. Described by the wave–particle duality elementary particles like photons do have properties of both waves and particles. The wavelength λ depends on the speed of light in the material c and the frequency of the wave ν [1]:

$$\lambda = \frac{c}{\nu} \quad (3.1)$$

Another important relationship described by quantum theory, states that the energy of each emitted photon is defined as:

$$e = h\nu = \frac{hc}{\lambda} \quad (3.2)$$

where $h = 6.626 \times 10^{-34} Js$ is named *Planck's constant*. [1]

The whole electromagnetic spectrum can be divided into wave regions or bands. These bands are defined by the process electromagnetic waves are emitted. Either by the nucleus, or by inner or outer electrons, by molecular vibrations, molecular rotations, or by electric currents. These bands are shown in figure 3.1. Regarding heat transfer, the International Electrotechnic Commission (IEC) defines the *IRA* band from 0.7 to $1.4\mu m$, the *IRB* and

IRC bands from 1.4 to $3\mu m$ and 3 to $1000\mu m$, respectively. For thermography we define the bands as follows: *near infrared* ($0.76 \div 3\mu m$), *middle infrared* ($3 \div 6\mu m$), *far or long infrared* ($6 \div 15\mu m$) and *extreme infrared* ($15 \div 1000\mu m$). For practical use and due to the absorption spectra of water and carbon dioxide in the atmosphere the bands can be also defined as short-wave (SW) band from 2 to $5\mu m$ and long-wave (LW) band from 8 to $14\mu m$. In comparison to this, the spectrum of visible light for the human eye is in the range from 0.38 and $0.78\mu m$. [1]

3.1.2.1 Radiation of Black Bodies

The amount of emitted radiation from a real body depends on many factors like temperature, material, wavelength and more. In order to be able to establish physical laws, a conceptual body the so-called *black body* is introduced. A black body is a perfect emitter and absorber of radiation, which means a black body emits the maximum possible amount of radiation for a fixed temperature and wavelength, regardless of direction. In practice, a dull black surface is a good estimation of a black body. [1] The mentioned assumptions for a black body lead to *Planck's law* of radiation [38]:

$$M_\lambda(T) = \frac{2\pi hc^2}{\lambda^5} \frac{1}{e^{hc/\lambda kT} - 1} \times 10^{-6} \quad (3.3)$$

where the factor 10^{-6} is used since the spectral radiant emittance M_λ is expressed in $[\frac{W}{m^2\mu m}]$. Equation (3.3) leads to a family of curves for various temperatures shown in figure 3.2. It can be observed that a temperature rise leads to a shift of the peak towards shorter wavelengths. This phenomenon is described by *Wien's displacement law*. The wavelength with the highest spectral radiance can be calculated as in eq. (3.4):

$$\lambda_{\max} = \frac{b}{T} \quad (3.4)$$

By integrating *Planck's law* over the whole range of wavelengths we obtain the total radiant emittance of a black body, the *Stefan-Boltzmann's law*. Equation (3.5) shows that the total emittance of a black body correlates with the fourth power of the absolute body temperature.

$$M(T) = \int_0^\infty M_\lambda(T) d\lambda = \sigma T^4 \quad (3.5)$$

The *radiant emittance* $[\frac{W}{m^2}]$ (*Abstrahlungsstärke*) emitted from a surface becomes an *irradiance* (*Bestrahlungsstärke*) when absorbed by a surface. When related to a spectral range

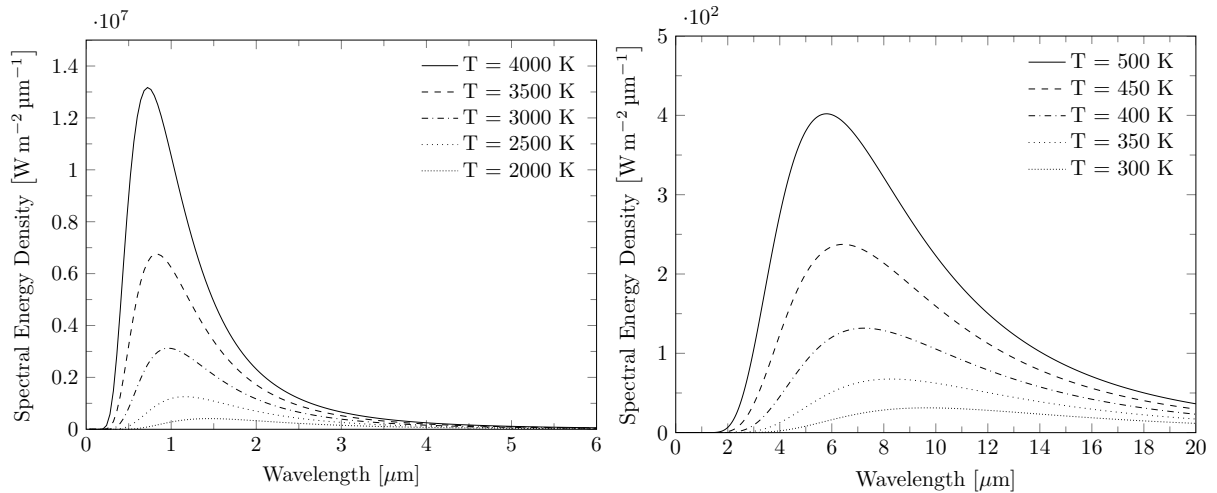


Figure 3.2: Spectral radiation emittance. Curves plotted for a range of temperatures from 2000 K to 4000 K (left) and from 300 K to 500 K (right).

radiant emittance is called *spectral radiant emittance* [$\frac{W}{m^2 \mu m}$] (*spektrale Abstrahlungsstärke*) or *spectral irradiance* (*spektrale Bestrahlungsstärke*), respectively. When related to the direction (steradian) and emitted from a surface this number is called *radiance* [$\frac{W}{m^2 sr}$] (*Strahldichte*). The IR power transmitted between emitter and absorber is called (*radiant*) *flux* (*Strahlungsleistung*).

3.1.2.2 Radiation of Real Bodies

Generally speaking real objects hardly ever behave like a black body over a wide range of wavelength. While a black body absorbs all incident radiation (also called irradiance), a real body can also experience transmission and reflection. The balance of the radiation can be written as the *total power law* [38] which is illustrated in figure 3.3 and shown in eq. (3.6):

$$\Phi_{\text{absorbed}} + \Phi_{\text{reflected}} + \Phi_{\text{transmitted}} = \Phi_{\text{incident}} \quad (3.6)$$

or in a normalised form :

$$\alpha(\lambda) + \rho(\lambda) + \tau(\lambda) = 1 \quad (3.7)$$

Emissivity is defined as the ratio of the spectral radiant emittance of a given body to that of a black body. [38]

$$\varepsilon(T) = \frac{M_{\lambda}(\lambda, T)}{M_{\lambda}^{BB}(\lambda, T)} \quad (3.8)$$

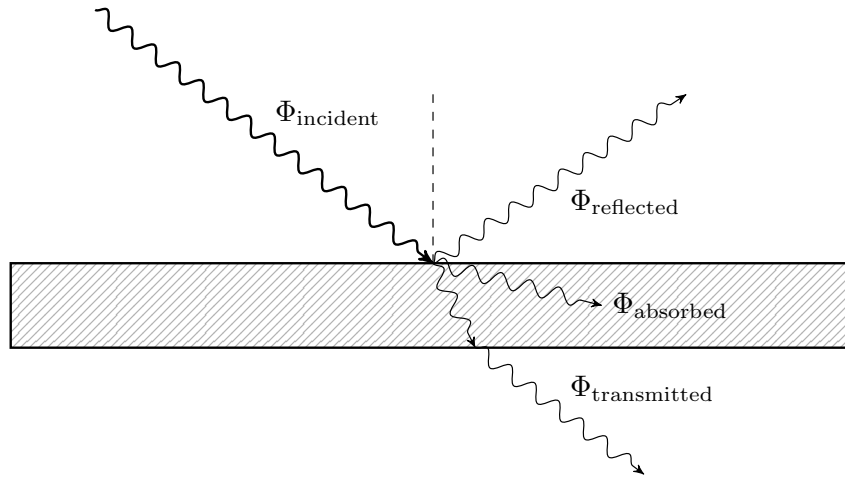


Figure 3.3: Reflection, absorption and transmission.

Materials with an emissivity below one which is not changing with wavelength are called *gray body*, materials with emissivity changing with the wavelength are called *spectral body* or *selective radiator* (figure 3.4).

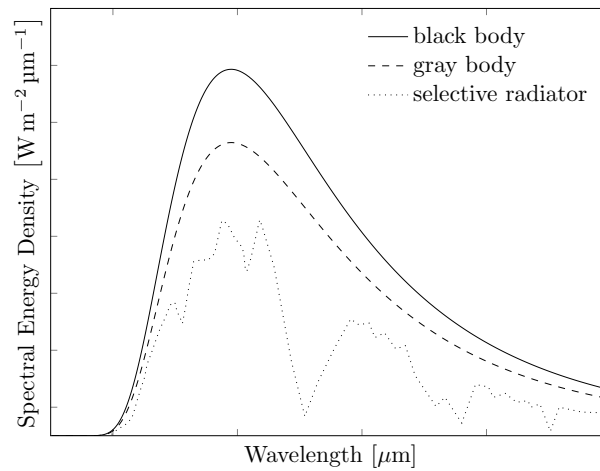


Figure 3.4: Spectral radiant emittance of three types of radiators.

The *Stefan-Boltzmann's law*, strictly speaking only valid for black bodies as seen in equation (3.5) can now also be applied to grey bodies:

$$M(T) = \varepsilon(T)\sigma T^4 \quad (3.9)$$

3.1.3 Radiometric Calibration

This section provides a summary of the radiometric calibration theory described in the book *"Infrared Thermography for Thermo-Fluid-Dynamics"* [1, p. 44 ff]. The electrical signal of the IR detector is related to the radiation emittance (power) from the sampled surface. The following equations (3.10) to (3.14) lead to a calibration function which connects the output signal of the detector with the object target temperature. Most modern thermography systems are already calibrated and calculate the object temperature internally using appropriate calibration curves, or even use build-in black bodies to recalibrate the system. Despite this, sometimes it is necessary to get a more accurate output which can be achieved with a custom recalibration in a specific temperature range. This is especially the case when special optics or window glasses are used with the thermographic system.

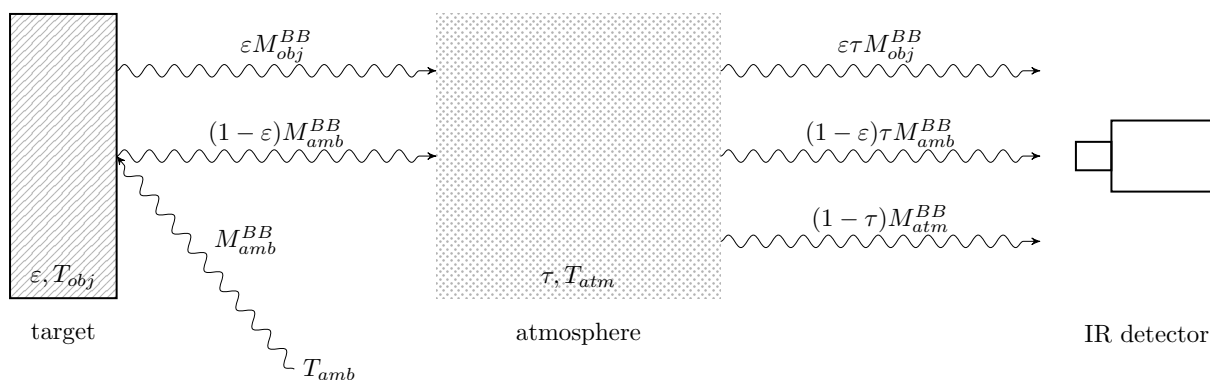


Figure 3.5: General thermographic measurement situation.

In figure 3.5 a general thermographic measurement situation is shown. One can see that not only the target emittance is collected by the sensor, but there is also an influence of ambient radiation and the atmosphere itself. The surrounding ambient environment can be considered as a black body with the constant Temperature T_{amb} and the emitted radiation M_{amb}^{BB} and gets reflected on the target. The reflectivity coefficient can be evaluated as $(1 - \epsilon)$ for opaque objects. The influence of a viewing window between the camera and the measurement target can be included in the atmospheric fraction of the equation. All radiation fractions summed up lead to:

$$M_t = \epsilon \tau M_{obj}^{BB} + (1 - \epsilon) \tau M_{amb}^{BB} + (1 - \tau) M_{atm}^{BB} \quad (3.10)$$

With the given equation (3.10) it can be assumed a linear proportional behaviour of the detector signal U and the total radiant flux M_t :

$$U = \varepsilon\tau U_{obj} + (1 - \varepsilon)\tau U_{amb} + (1 - \tau)U_{atm} \quad (3.11)$$

The output signal can be approximated by a function similar to *Planck's law* depending on temperature and the introduced calibration constants R , B and F . This calibration constants depend on the characteristics of the complete infrared camera system.

$$U = \varepsilon\tau \frac{R}{e^{\frac{B}{T_{obj}}} - F} + (1 - \varepsilon)\tau \frac{R}{e^{\frac{B}{T_{amb}}} - F} + (1 - \tau) \frac{R}{e^{\frac{B}{T_{atm}}} - F} \quad (3.12)$$

Rearranging equation (3.12) leads to the object temperature:

$$T_{obj} = \frac{B}{\ln\left(\frac{\varepsilon\tau R}{U - (1 - \varepsilon)\tau U_{amb} - (1 - \tau)U_{atm}} + F\right)} \quad (3.13)$$

For calibration purposes one may choose a black body ($\varepsilon = 1$) placed close in front of the camera ($\tau = 1$) to simplify the equation.

$$T_{obj} = \frac{B}{\ln\left(\frac{R}{U}\right) + F} \quad (3.14)$$

With a set of n independent measurement points at different black body temperatures, the calibration constants can be found by curve fitting.

3.2 Image Processing

This section is a summary of the principle ideas of projective transformations covered by the book "Multiple View Geometry in computer vision"[16]. It provides a basic understanding of the MATLAB routine written by the author (section 5.1) for image mapping used in postprocessing of the measured thermographic data obtained by an infrared camera. The objective of this chapter is to provide the basics how to link two-dimensional (2D) thermographic projections to the temperature distribution along a arbitrarily shaped surface (three-dimensional; 3D).

3.2.1 Pinhole Camera Model

The usual way to find the connection between a 3D scene and a 2D image plane is to find a simplified camera model. A reasonable approximation of a camera is based on the passage of ray of light pass through a single point in space (pinhole aperture). This projection is called *central projection*.

The simplest camera used to visualize this process is the pinhole camera. Figure 3.6 shows the central projection of a point $\mathbf{X} = (X, Y, Z)$ onto the *image plane* (or *focal plane*) $z = f$ through the center of projection C. By similar triangles the mapping of the point onto the image plane is described as:

$$\begin{pmatrix} X \\ Y \\ Z \end{pmatrix} \mapsto \begin{pmatrix} f \frac{X}{Z} \\ f \frac{Y}{Z} \end{pmatrix} \quad (3.15)$$

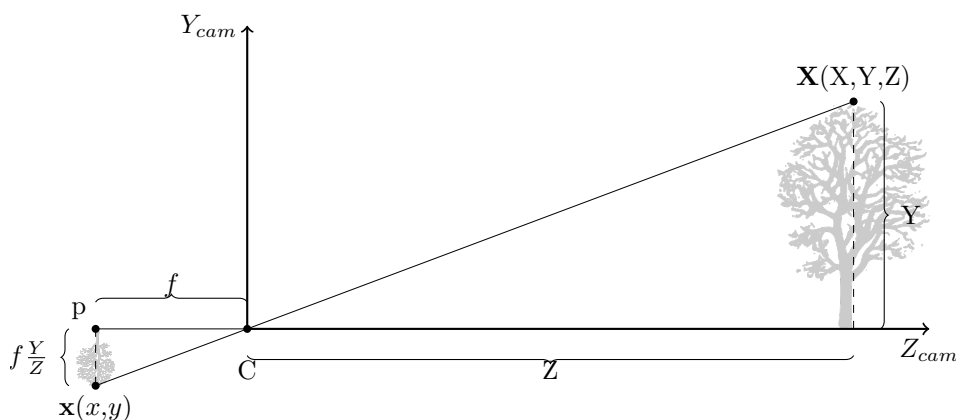


Figure 3.6: Pinhole camera geometry

”The center of projection is called the *camera center*. It is also known as the *optical center*. The line from the camera center perpendicular to the image plane is called the *principal axis* or *principal ray* of the camera, and the point where the principal axis meets the image plane is called the *principal point*. The plane through the camera centre parallel to the image plane is called the *principal plane* of the camera.” [16, p.154]

3.2.2 Homogeneous Coordinates

Homogeneous coordinates also called projective coordinates are a system of coordinates used in projective geometry. The use of this coordinates makes the central projection very simple due to the linear mapping of their homogeneous coordinates. Equation (3.15) in terms of matrix multiplication may be written as:

$$\begin{pmatrix} X \\ Y \\ Z \\ 1 \end{pmatrix}_{camera\,frame} \mapsto \begin{pmatrix} fX \\ fY \\ Z \end{pmatrix}_{camera\,frame} = \begin{bmatrix} f & 0 & 0 & 0 \\ 0 & f & 0 & 0 \\ 0 & 0 & 1 & 0 \end{bmatrix} \begin{pmatrix} X \\ Y \\ Z \\ 1 \end{pmatrix}_{camera\,frame} \quad (3.16)$$

This leads to the homogeneous 4-vector \mathbf{X} representing a point in space in the camera coordinate frame, the homogeneous 3-vector \mathbf{x} representing an image point in the camera coordinate frame and the 3×4 homogeneous camera projection matrix \mathbf{P} .

$$\begin{pmatrix} x \\ y \\ w \end{pmatrix} = \mathbf{P}_{3 \times 4} \begin{pmatrix} X \\ Y \\ Z \\ T \end{pmatrix} \quad (3.17)$$

The camera matrix for the pinhole model of central projection is defined as

$$\mathbf{P} = \begin{bmatrix} f & 0 & 0 & 0 \\ 0 & f & 0 & 0 \\ 0 & 0 & 1 & 0 \end{bmatrix} \quad (3.18)$$

3.2.3 Principal Point Offset

In expression (3.15) the image and camera coordinate frame overlap. In a more general case the origin of the image coordinate system can be shifted to the corner of the image

by implementing the coordinates of the principal point $(p_x, p_y)^T$. Now the following transformation is obtained:

$$\begin{pmatrix} X \\ Y \\ Z \\ 1 \end{pmatrix}_{cameraframe} \mapsto \begin{pmatrix} fX + Zp_x \\ fY + Zp_y \\ Z \\ 1 \end{pmatrix}_{imageframe} = \begin{bmatrix} f & 0 & p_x & 0 \\ 0 & f & p_y & 0 \\ 0 & 0 & 1 & 0 \end{bmatrix} \begin{pmatrix} X \\ Y \\ Z \\ 1 \end{pmatrix}_{cameraframe} \quad (3.19)$$

Now, writing

$$\mathbf{K} = \begin{bmatrix} f & 0 & p_x \\ 0 & f & p_y \\ 0 & 0 & 1 \end{bmatrix} \quad (3.20)$$

The matrix \mathbf{K} is called camera calibration matrix and contains the intrinsic parameters of the camera.

$$\mathbf{x}|_{imageframe} = \left[\begin{array}{c|c} \mathbf{K}_{3 \times 3} & \begin{matrix} 0 \\ 0 \\ 0 \end{matrix} \end{array} \right] \mathbf{X}|_{cameraframe} \quad (3.21)$$

3.2.4 Camera Rotation and Translation

The next step in the "case" generalization is to introduce the world coordinate frame. The two coordinate frames are related via a rotation and a translation in space. $\tilde{\mathbf{C}}$ represents the 3-vector of the camera center in the world coordinate frame. This leads to:

$$\mathbf{X}|_{cameraframe} = \overbrace{\left[\begin{array}{c|c} \mathbf{R}_{3 \times 3} & \begin{matrix} 0 \\ 0 \\ 0 \end{matrix} \end{array} \right]}^{rotation} \overbrace{\left[\begin{array}{c|c} \mathbf{I}_{3 \times 3} & -\tilde{\mathbf{C}}_{3 \times 1} \\ \hline 0 & 0 & 0 & 1 \end{array} \right]}^{translation} \mathbf{X}|_{worldframe} \quad (3.22)$$

Combining eq. (3.22) to our already derived eq. (3.21) leads to our searched connection between the image coordinate frame and the world coordinate frame of the pinhole camera model:

$$\mathbf{x}|_{imageframe} = \mathbf{P}\mathbf{X}|_{worldframe} \quad (3.23)$$

$$\mathbf{P} = \mathbf{KR} \left[\mathbf{I} \mid -\tilde{\mathbf{C}} \right] \quad (3.24)$$

”One sees that a general pinhole camera, $\mathbf{P} = \mathbf{KR} \left[\mathbf{I} \mid -\tilde{\mathbf{C}} \right]$, has 9 degrees of freedom: 3 for \mathbf{K} (the elements f, p_x, p_y), 3 for \mathbf{R} , and 3 for $\tilde{\mathbf{C}}$. The parameters contained in \mathbf{K} are called the internal camera parameters, or the internal orientation of the camera. The parameters of \mathbf{R} and $\tilde{\mathbf{C}}$ which relate the camera orientation and position to a world coordinate system are called the external parameters or the exterior orientation.” [16, p.156]

3.2.5 Finite Projective Camera

In a more general form, \mathbf{K} includes also the transformation from image coordinates to pixel coordinates, which may be non-squared, with a skew parameter s :

$$\mathbf{K} = \begin{bmatrix} \alpha_x & s & x_0 \\ & \alpha_y & y_0 \\ & & 1 \end{bmatrix} \quad (3.25)$$

$\alpha_x = fm_x$ and $\alpha_y = fm_y$ denote the focal lengths of the camera in terms of pixel dimensions, where m_x and m_y are the number of pixels per unit distance in the image coordinates. The principal point in terms of pixel dimensions is now written with $x_0 = m_x p_x$ and $y_0 = m_y p_y$. A camera of the form (3.24) with the calibration matrix (3.25) is called *finite projective camera* and has 11 degrees of freedom. [16]

3.2.6 Computation of the Camera Matrix

This section is about methods for finding a correlation of the camera matrix \mathbf{P} with a set of point correspondances $\mathbf{X}_i \leftrightarrow \mathbf{x}_i$. The Direct Linear Transformation (DLT) algorithm is about solving the following set of equations:

$$\begin{bmatrix} 0^T & -w_i \mathbf{X}_i^T & y_i \mathbf{X}_i^T \\ w_i \mathbf{X}_i^T & 0^T & -x_i \mathbf{X}_i^T \\ -y_i \mathbf{X}_i^T & x_i \mathbf{X}_i^T & 0^T \end{bmatrix} \begin{pmatrix} \mathbf{P}^1 \\ \mathbf{P}^2 \\ \mathbf{P}^3 \end{pmatrix} = 0 \quad (3.26)$$

Only two of those three rows can be used for the estimation of \mathbf{P} , because the three equations are linear dependend. By stacking up the equations of n point correspondances we obtain a $2n \times 12$ matrix \mathbf{A} . The camera matrix \mathbf{P} can be computed by solving an

overdetermined set of equations. For a solution of the equation $\mathbf{A}\mathbf{p} = \mathbf{0}$ at least $n \geq 6$ point correspondances are needed to calculate the 12 entries of \mathbf{P} . In this thesis the suggested Singular Value Decomposition (SVD) is compared with an alternative iterative solving method.

3.2.7 Reprojection Error

The point correspondances of section 3.2.6 used for the calculation of the camera matrix are now used to calculate the mean reprojection error of \mathbf{P} . This error in pixel units is an information about the projection quality and is calculated as:

$$\frac{1}{i} \sum_i d(\mathbf{x}_i, \mathbf{P}\mathbf{X}_i) \quad (3.27)$$

where $d(x, y)$ stands for the Euclidean distance between the points x and y . Basically a known point in space \mathbf{X}_i gets projected onto the image frame and compared in order of distance error to its corresponding reference point \mathbf{x}_i .

3.2.8 Decomposition of the Camera Matrix

With the now known camera matrix \mathbf{P} it is possible to reconstruct the calibration matrix \mathbf{K} and external camera parameters like orientation and position by matrix decomposition. Equation (3.24) can also be written as:

$$\mathbf{P} = \left[\mathbf{M} | -\mathbf{M}\tilde{\mathbf{C}} \right] = \mathbf{K} \left[\mathbf{R} | -\mathbf{R}\tilde{\mathbf{C}} \right] \quad (3.28)$$

Where \mathbf{K} and \mathbf{R} can be found by decomposing $\mathbf{M} = \mathbf{K}\mathbf{R}$ using the so-called RQ-decomposition. The calculation of the camera center $\mathbf{C} = (X, Y, Z, T)^\top$ can be done with:

$$\begin{aligned} X &= \det([\mathbf{p}_2, \mathbf{p}_3, \mathbf{p}_4]) & Y &= -\det([\mathbf{p}_1, \mathbf{p}_3, \mathbf{p}_4]) \\ Z &= \det([\mathbf{p}_1, \mathbf{p}_2, \mathbf{p}_4]) & T &= -\det([\mathbf{p}_1, \mathbf{p}_2, \mathbf{p}_3]) \end{aligned} \quad (3.29)$$

4 Preliminary Experiments for Thermography Postprocessing

4.1 MATLAB Camera Calibration Tool

In the early stages of the thesis, the possible use of reference patterns in the measurement area was investigated. The MATLAB workspace offers an implemented application for camera calibration. The tool can be used to estimate camera extrinsics, intrinsics, and lens distortion parameters. "These applications include removing the effects of lens distortion from an image, measuring planar objects, or reconstructing 3-D scenes from multiple cameras." [36] The recommended workflow for the Single Camera Calibration according to MATLAB is as follows: "...

1. Prepare images, camera, and calibration pattern.
2. Add images and select standard or fisheye camera model.
3. Calibrate the camera.
4. Evaluate calibration accuracy.
5. Adjust parameters to improve accuracy (if necessary).
6. Export the parameters object." [36]

For the experiments carried out in the thesis a checkerboard pattern with a known edge length was used as a reference for the calibration (Figure 4.1). This pattern was analyzed from as many positions as possible. The camera calibration app uses these images to estimate the intrinsic, extrinsic and lens distortion parameters of the particular used camera.

In order to see a reference pattern also in the infrared range, metallicly shiny foils were used on which the pattern was printed. Figure 4.2 shows such a reference pattern in the infrared and visible range.

Although the surface shown has the same ambient temperature, the pattern can be seen as significantly different temperature zones in the picture. These quasi higher temperatures on the reflecting surface are due to the different emissivity of the printed checkerboard

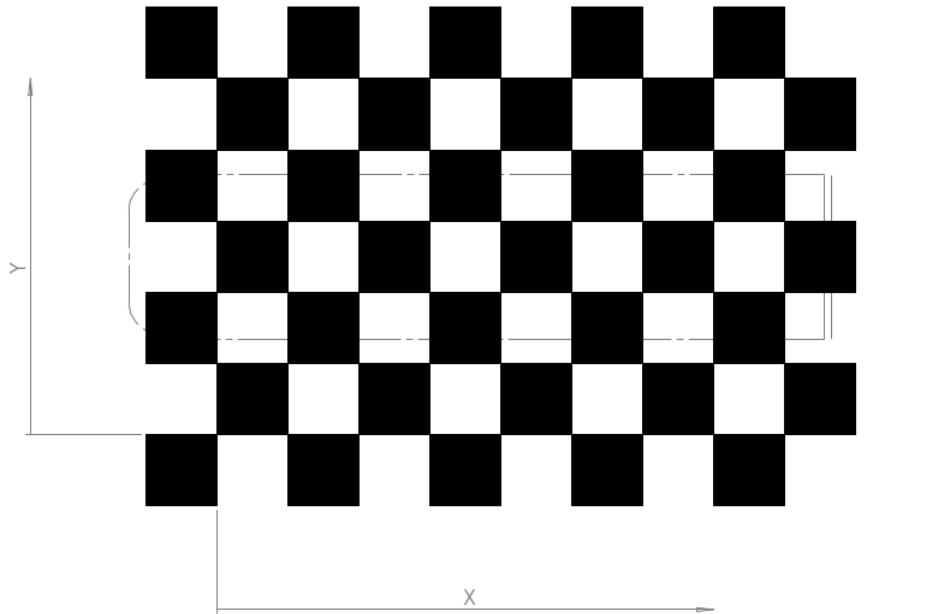


Figure 4.1: Checkerboard pattern. Edge length of 15 mm with a defined position of the measured object.

pattern and caused by the reflections of a background radiator in the infrared range. This clearly shows how important it is to know the emissivity of the observed surface in order carry out accurate measurements with a thermographic camera.

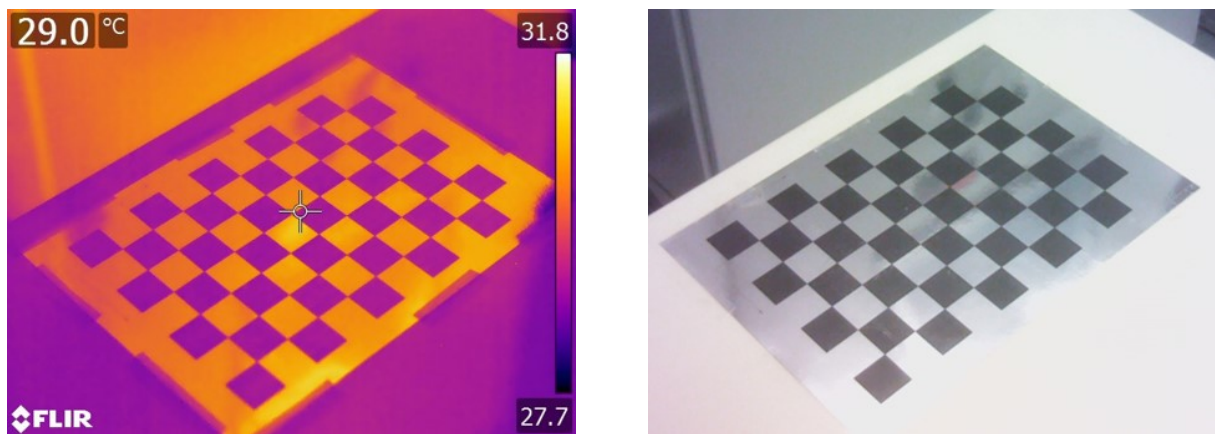


Figure 4.2: Checkerboard pattern for Camera Calibration. Infrared image (left), Digital image visible light (right).

Figure 4.3 shows the camera calibration process. After starting the application, the edge length of the used pattern must be entered to create a dependency of the spatial dimensions. After that, any number of multidirectional shots of the pattern can be loaded (Figure 4.3 (a)). MATLAB then loads each image and sorts out images that cannot be processed at this point. The calculation options for distortion can then be set. Since this calibration is an iterative procedure, internal parameters known from the camera used can also be

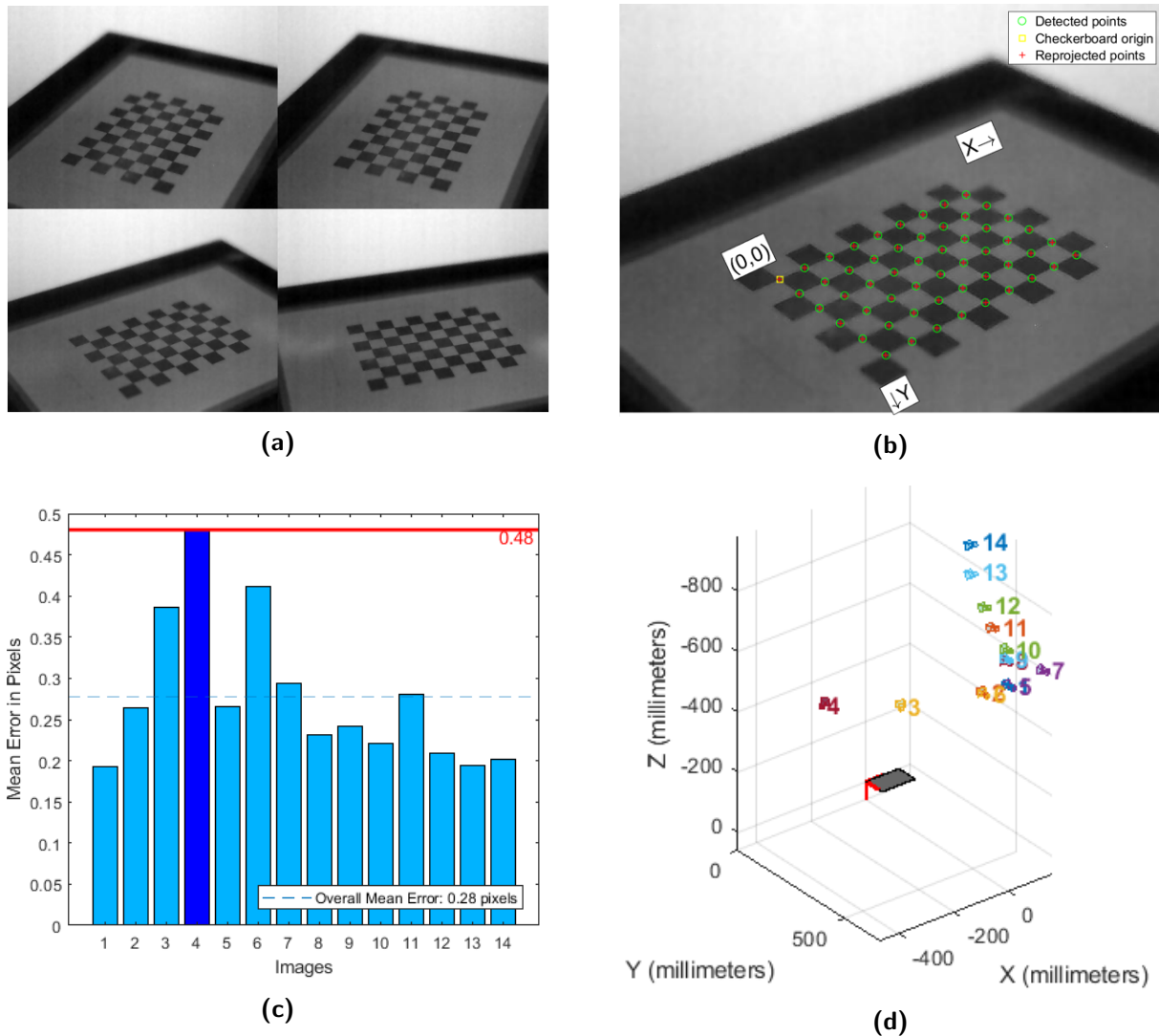


Figure 4.3: Camera Calibration Tool. (a) Multidirectional captured reference pattern, (b) Detected and reprojected checkerboard points, (c) Reprojection errors, (d) Extrinsic.

defined as initial conditions in order to optimize the solution. After these settings the calibration can be started. The application detects the corner points of the pattern in each image and can then estimate the unknown camera parameters. As quality criterion the average error of all pattern points is displayed (Figure 4.3 (c)). Bad images can be removed to improve quality during recalibration. Finally, the results are collected and exported as an object containing data about the camera's properties, the camera's extrinsics, the accuracy of the estimation, and the calibration settings. 4.3 (d)) shows the calculated camera positions of each shot.

4.2 Angular Dependency Study

For multi-directional observations, one of the first investigations done in this thesis was to figure out the dependency of thermographic temperature recording on angular position of the camera. For first measurements a model of the flow geometry was painted matt black and recorded from different angles.

In order to detect any possible angle dependency of the measured temperature, measurements were carried out at ambient conditions on a black painted strut profile. At the beginning, the scene was captured without an object to display the reference pattern. The Camera Calibration Tool described in Chapter 4.1 automatically detects the corners of the pattern and can recalculate the camera position in space with a camera calibration generated in advance. (Figure 4.4 (a))

The object to be measured was then placed at a defined position on the reference pattern. A set of 27 measuring points on the three-dimensional object was then assigned locally to the infrared image. The positions are marked green in Figure 4.4 (b).

To present the measurement situation used, the measurement points and the camera position is shown in Figure 4.4 (c).

Figure 4.4 (d) shows the vectorially calculated observation angles of the measurement points, where the value 0° stands for the perpendicular alignment of the object surface to the camera.

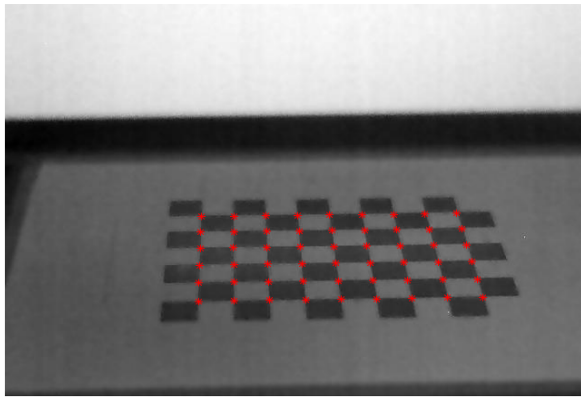
The measured temperatures of such a recording are shown in Figure 4.4 (e). A closer look at the values reveals that despite a theoretically constant object temperature, the temperature in the area around the vertical observation angle is relatively constant, but decreases with increasing observation angle (from about 20° upwards). This result can also be seen in Figure 4.4 (b). At the radius at the right edge of the object a kind of shading is recognizable in the infrared image, although the actual temperature of the entire object should be constant. Darker in this image means a lower temperature.

The emissivity is thus, as already mentioned in the theory chapter, wavelength and temperature dependent, but also angle dependent. ($\varepsilon = \varepsilon(\lambda, T, \delta)$)

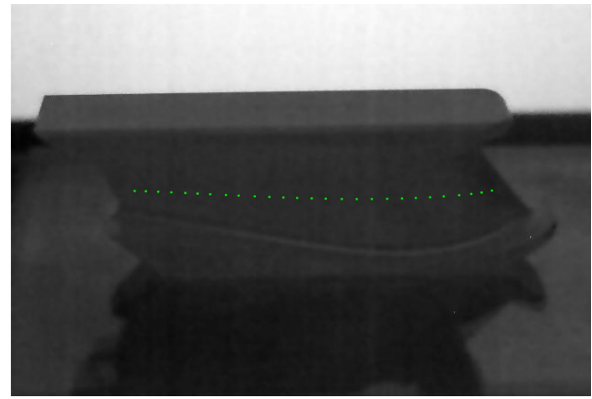
These first preliminary tests showed that the use of the reference pattern and the standard Matlab tool could not be used in the areas of the TTTF rig with a limited field-of-view (FOV). Also important calibration data for emissivity and transmissivity could only be carried out under engine relevant conditions in advance, because the thermographic measurement is strongly related on material, surface, observation angle and surrounding.



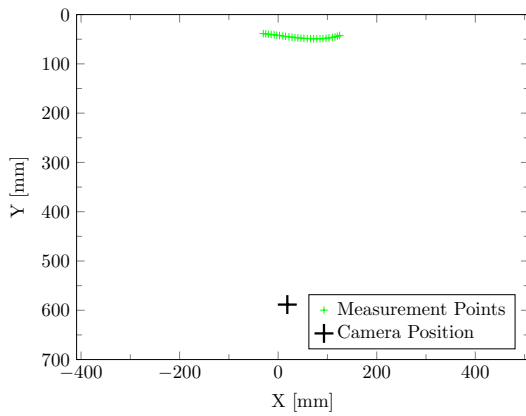
The outcome was to look for other options to perform the measurement and to set up a test bench for running pilot tests.



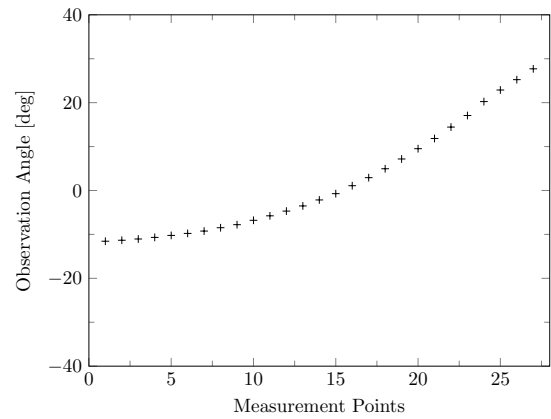
(a)



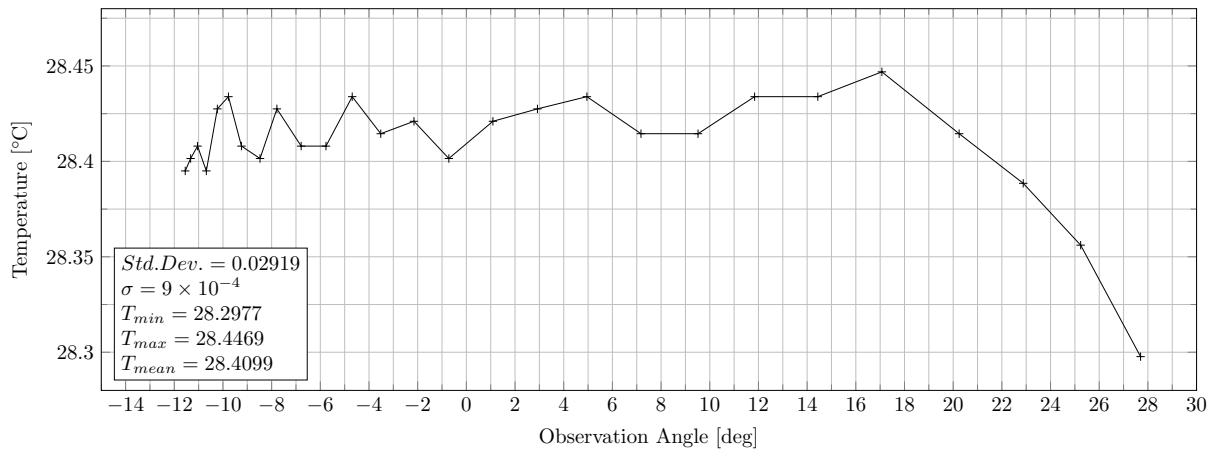
(b)



(c)



(d)



(e)

Figure 4.4: Directional observation. (a) Checkerboard pattern with detected corners marked in red; (b) Infrared image and measurement positions marked in green; (c) Bird's-eye view of the camera position and the measurement points; (d) Observation angle of the measurement points (0° is perpendicular to the surface); (e) Measured temperatures over the observation angle

5 Developement of an IR-Image Postprocessing Routine

This chapter describes the steps performed to develop post-processing routines for infrared images. The problem was to geometrically correlate the recorded thermography data of the camera with the associated measurement area. Especially the limited optical access as well as the curved geometry were challenging. Literature research was made in the field of image processing to find correct and accurate approaches to this problem. The research led to countless applications in the very up to date and constantly advancing field of computer vision. Possibilities for image processing and data evaluation with the help of programs such as OpenCV or MATLAB were investigated. The fundamental literature, apart from already implemented tools, was also consulted. Especially the book *"Multiple View Geometry in computer vision"*[16] proved to be very useful.

5.1 Custom-made MATLAB routine for the geometric mapping of measured infrared images

Due to the limited accessibility to the measuring area, the curved surfaces and a small field of view, the reference patterns described in section 4.1 were difficult to implement. Again a literature study was performed for solutions to combine image information and geometry. The DLT algorithm already theoretically explained in section 3.2.6 which is discussed by the book *"Multiple View Geometry in computer vision"*[16] was chosen. This section now covers the implementation of this coordinate transformation procedure in MATLAB up to the data visualization in Tecplot.

A concept for the development of software in MATLAB was worked out. The data of the thermal images had to be geometrically coupled with the associated measurement field. The most important parameters of the software are summarized in Figure 5.1 and are described in more detail in the following chapters.

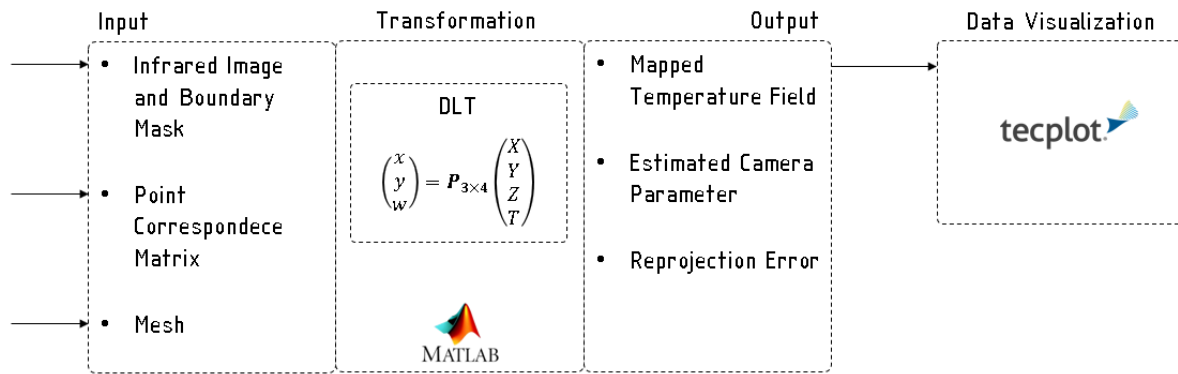


Figure 5.1: Block diagram of software concept

5.1.1 Input

Required inputs for the software:

- Infrared image of the measurement area
- Boundary mask to hide unneeded sections of the image
- Point correspondence of each single image
- A discrete mesh of the measurement area

Infrared Image and Boundary Mask

In order to exclude uninteresting or unusable regions in the captured images, a mask must be created in parallel for each image. This file describes the region of interest (ROI) and is a black and white *.png file. Gimp was used to create these masks in this work, but any image processing program can be used. All areas in black, more specific with the RGB code (0,0,0), are excluded for further calculations. Thus it was possible to use only certain areas of the images. Figure 5.2 shows an example of such a mask, the housing of the window was marked black. Temperature data in these areas are not usable and were therefore discarded.

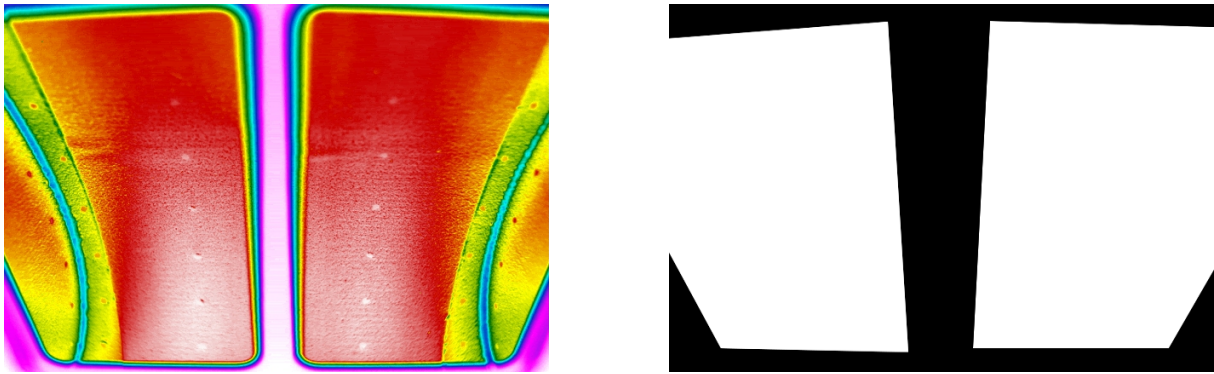


Figure 5.2: Image preparation. IR image showing the hub surface of the TCF and also the window frame (left). Boundary mask for the image. Regions in black will be excluded from the transformation (right).

Point Correspondence Matrix

The basic requirement for this algorithm are a set of point correspondences. This implies that the 3D coordinates of certain points in an image are known in space. In practice, 74 reference points were defined on the surface to be measured. The choice here was arbitrary, therefore favorable net points of the existing surface geometry were used. An important criteria taken into account for the density of the reference points was that at least six, optimally more than twelve points are visible per image. Figure 5.3 shows the defined reference points. The visualization of the points again demanded a distinct different emissivity of the points compared to the surface being measured. The practical implementation of this points was mentioned in the previous section and can be seen in Figure 6.15

A MATLAB user interface has been created to process this data. Figure 5.4 shows the layout of this GUI. IR images can be loaded, then specific reference points can be selected in a dropdown menu, which must then be identified with a crosshair in the image. In this way, the required correlations must be recorded for each image. Finally, the generated data can be exported to the relevant directory in form on a point correspondence matrix.

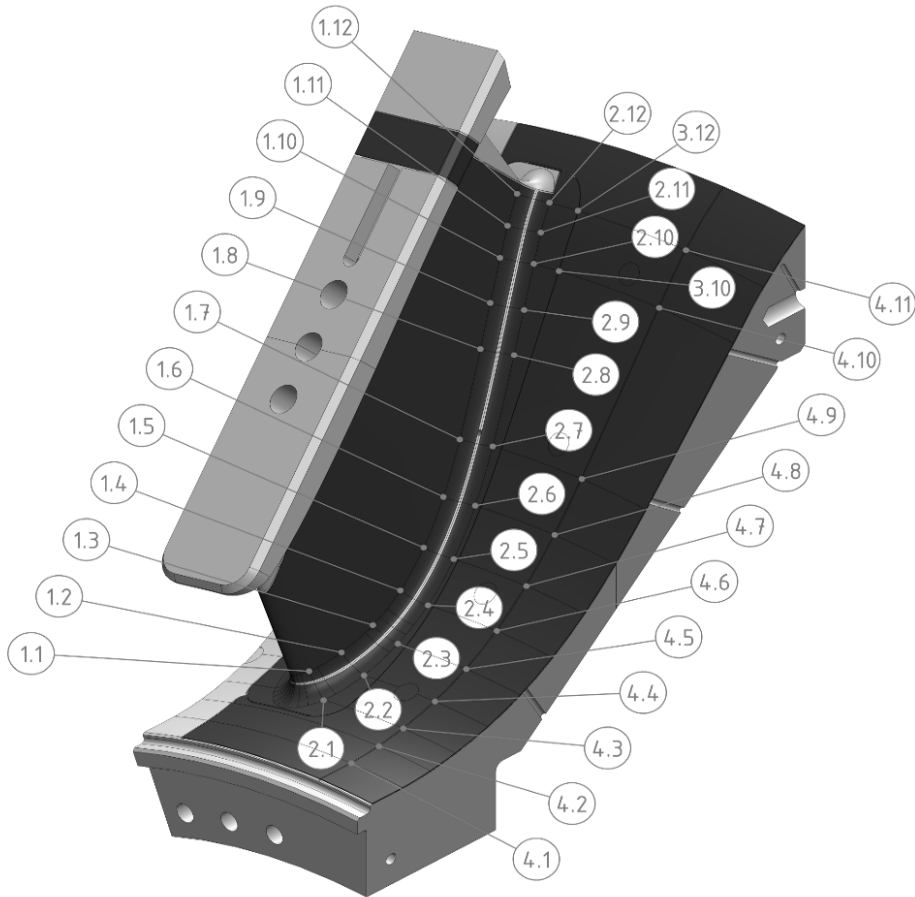


Figure 5.3: Reference points. Labeling of the defined reference points

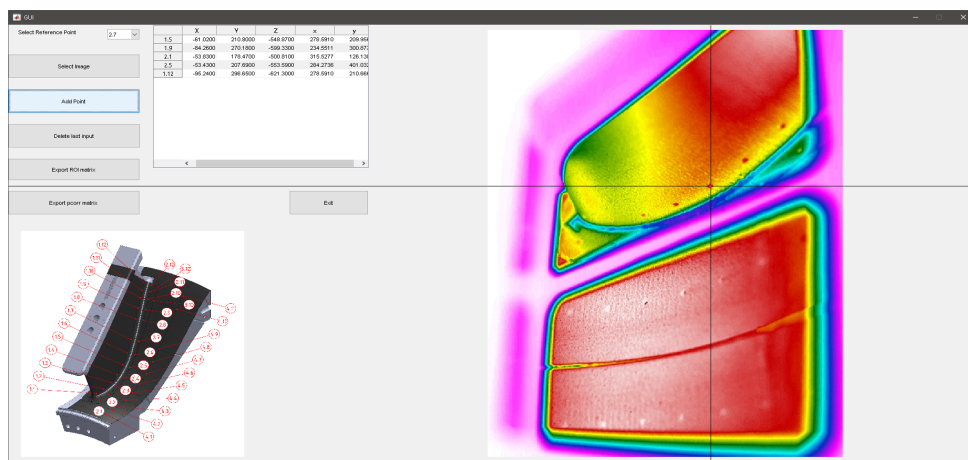


Figure 5.4: MATLAB user interface for input values

Mesh

In order to perform the following coordinate transformation, the surface had to be divided into discrete points. This discretization was done by meshing the surface with Ansys. A CFD - Fluent mesh with an element size of 0.5 mm was generated to achieve a sufficiently fine point distribution. In order to create a structured mesh and to increase the quality, the function "face meshing" was applied. The surface geometry and generated mesh is shown in figure 5.5. In this configuration it has 210586 nodes and 203619 elements, but can be adapted as needed. For importing it into the written MATLAB code, the mesh must be exported as a *.msh file and saved in the main directory. The correct output format (ASCII) must be ensured when exporting. The setting for this can be found in Ansys under options > mesh > export > format.

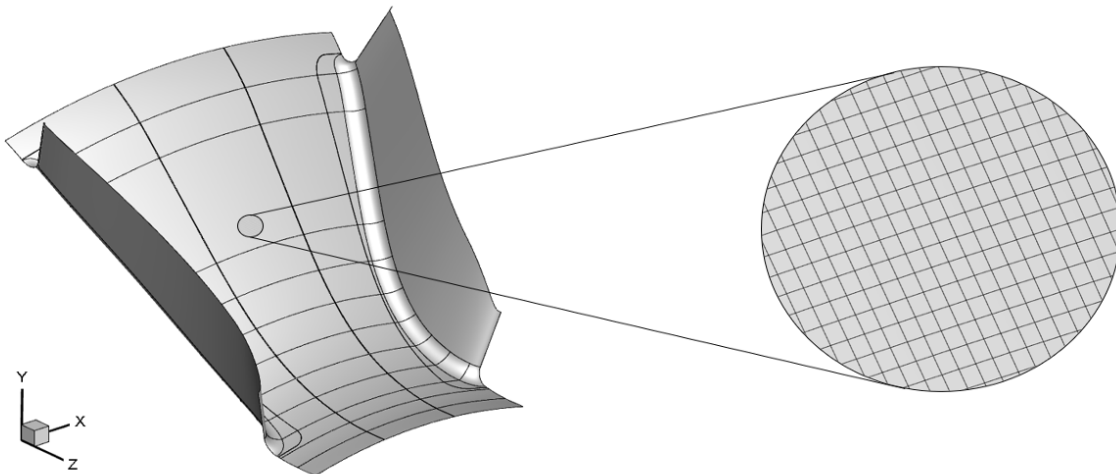


Figure 5.5: Surface geometry and generated mesh

5.1.2 Transformation

After the creation of all input parameters, the estimation of the camera matrix P as described in chapter 3.2.6 and its subsequent use for the mapping process will be explained.

Computation of the Camera Matrix

In the first step, a camera matrix has to be calculated for each image with the help of the associated point correspondences. The steps performed in the program are summarized in Figure 5.6. For more in-depth information, refer to the provided literature and the code in the appendix.

Objective

Given $n \geq 6$ world to image point correspondences $\{\mathbf{X}_i \leftrightarrow \mathbf{x}_i\}$, determine the Maximum Likelihood estimate of the camera projection matrix P .

Algorithm

- (i) **Linear Solution.** Compute an initial estimate of P using a linear method.
 - a) **Normalization:** Use a similarity transformation T to normalize the image points, and a second similarity transformation U to normalize the space points. Suppose the normalized image points are $\tilde{\mathbf{x}}_i = T\mathbf{x}_i$, and the normalized space points are $\tilde{\mathbf{X}}_i = U\mathbf{X}_i$.
 - b) **DLT:** Form the $2n \times 12$ matrix A by stacking the equations generated by each correspondence $\tilde{\mathbf{X}}_i \leftrightarrow \tilde{\mathbf{x}}_i$. Write \mathbf{p} for the vector containing the entries of the matrix \tilde{P} . A solution of $Ap = 0$, subject to $\|p\| = 1$, is obtained from the unit singular vector of A corresponding to the smallest singular value.
- (ii) **Denormalization.** The camera matrix for the original (unnormalized) coordinates is obtained from \tilde{P} as

$$P = T^{-1}\tilde{P}U$$

Figure 5.6: Summary of the transformation algorithm for estimating P from world to image point correspondences in the case that world points are accurately known. Adapted from [16, p. 181]

Mapping of Image Data

After estimating the camera matrix P and verifying the transformation quality using the camera parameters and a reprojections error, the relationship between image and space points is found. Each point in the measurement area is now assigned to the corresponding temperature data from the 640×480 pixel IR image.

This coordinate transformation can now be carried out for every single defined point in the measurement field. The individual points are taken from the mesh described previously and their associated image coordinates are calculated. Figure 5.7 shows this process schematically for one point marked in red. The image pixel information in the infrared image can then be assigned to the previously transformed mesh point.

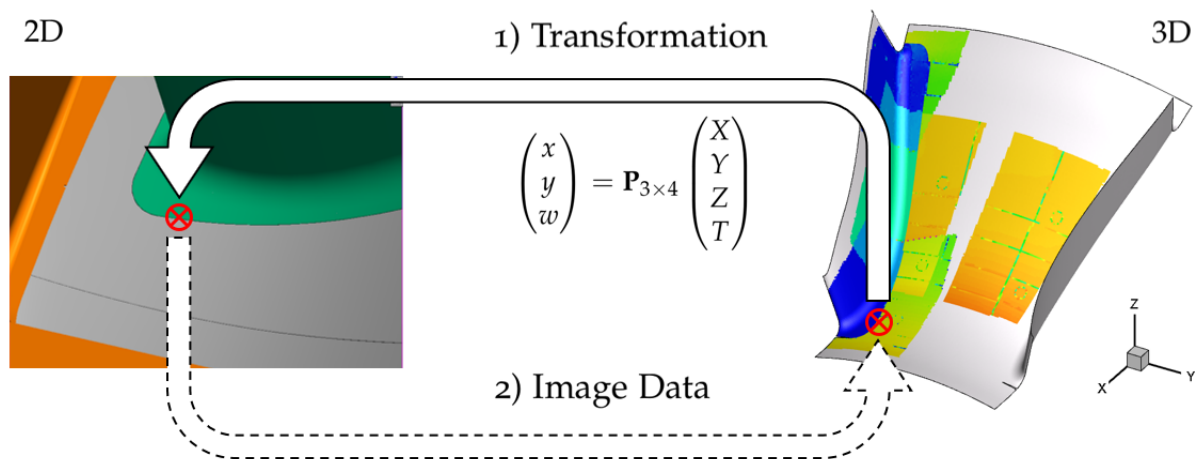


Figure 5.7: Transformation process. Each discrete mesh point can be transformed into two-dimensional image coordinates.

5.1.3 Output

This section describes which parameters are output in the program. This section of the program is of particular importance. Here data can be filtered, calibrated and converted before being exported as an output file. Especially in areas of overlapping of several recordings processing filters have to be implemented as outlook.

All data exported in the output.txt file can be displayed in many ways with the Tecplot data visulation tool. Figure 5.8 shows the section of the code that performs data postprocessing. Any number of columns can be appended to the output vector "tecplot" in line 9 by adapting the header in line 5 accordingly.

In addition to the exported temperature data for the visualization, data for the estimation of a measurement error were generated and stored. These data can be viewed after the transformation in Matlab. Important are the iteratively determined internal and external camera parameters, which give information about focal length, skew and principal point, as well as the position of the camera in space. Another quality criterion was introduced with the "reprojection error". The known reference points in space are transformed with the help of the determined camera matrix P and then geometrically compared with the manually read-in pixels described in section 5.1.1. The geometric deviation for each individual reference point is determined. The mean deviation of each of these points is stored as a value in pixels and indicates the mean reprojection error.

```

1      %% Export for Tecplot
2      %header
3      fid = fopen('tecplot.dat', 'w');
4      fprintf(fid, 'TITLE = "Temperature plot"\n');
5      fprintf(fid, 'VARIABLES = "X", "Y", "Z", "T"\n');
6      fprintf(fid, 'ZONE N = %d, E = %d, DATAPACKING = POINT,
           ZONETYPE = FEQUADRILATERAL\n', size(grid_mp,1), size(
           connectivity,1));
7      fclose(fid);
8
9      tecplot = grid_mp;
10     tecplot(:,4) = mergedTfield;
11
12     % write data
13     dlmwrite('tecplot.dat', tecplot, 'delimiter', '\t', '
           precision', 8, '-append')
14     dlmwrite('tecplot.dat', connectivity, 'delimiter', '\t', '
           precision', 8, '-append', 'roffset', 1)

```

Figure 5.8: Export for Tecplot

5.1.4 Data Visualization in Tecplot

The result of the MATLAB routine is a file that can be opened in Tecplot for visualization. Tecplot is very well suited to the display of flow quantities, but can also be used for the purposes required here for the representation of temperature, heat flow or film cooling effectiveness on the wall. Plots obtained with Tecplot can be observed in the results chapter (Figure 7.1).

6 Development of a TCF Test Rig for IR Measurements

In this following chapter all steps of the construction of a test bench are described in more detail. It started with the concept, then moved on to implementation and assembly and ended with the first commissioning runs.

6.1 Mechanical Design and Construction

Considering that the general limitations for the measurement in the turbine center frame (TCF) were given by geometry, optical access, concept of the heating foils and thermographic camera, as first step a test rig for experimental investigations was developed. During the construction it was important to realize a test bench as fast and simple as possible, therefore rapid prototyping methods were used for complex components in the area of the flow channel.

It should be noted that the aim was not to reproduce the flow situation exactly, but rather to make the best possible use of the resources available within the institute in order to carry out qualitative measurements on a test bench.

A concept for the planned setup was introduced. Figure 6.1 shows the main components planned for the test bench as well as the intended output parameters.

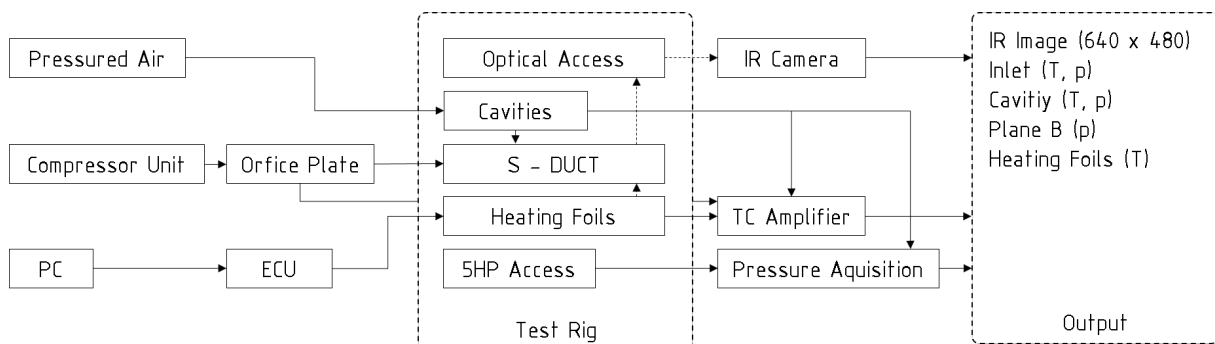


Figure 6.1: Block diagram of the test bench concept. Main components, instrumentation and output parameters.

6.1.1 Requirements

A subsonic compressor system existing at the institute for the generation of an air mass flow through the flow geometry was used. Instrumentation for the measurement of the volumetric flow and the temperature at the outlet of the compressor was already available and used in previously applied tests. These sensors were used for the following determination of the operating point during the experiments.

As already mentioned, the geometry was reproduced exactly by means of rapid prototyping, which also made possible the use of sensor accesses from the original geometry. The blind plug located at measurement plane B (see Figure 2.3) could therefore be used for measurements with a five hole probe or a pressure rake as in the original setup to provide data at the TCF inlet.

The instrumentation also included temperature measurements in the cavities as well as under the heating foils. The foils themselves were controlled by an electronic control unit (ECU) developed and provided by the manufacturer. The cavities were replicated to simulate their qualitative effects. Compressed air should be supplied. Also the optical access is geometrically exactly reproduced to check the accessibility of the defined measuring range and to determine and test possible camera positions in advance. The output parameters shown in Figure 6.1 were first of all an infrared image with a resolution of 640x480 pixel, as well as volume flow, pressure and temperature at the entry of the measured flow path. Data on the power supply of the heating foils should also be recorded.

In summary the requirements for the construction of this test rig were:

- Reproduction of the original geometry
- Heating foil placement
- Replication of the optical access
- Even inflow at the inlet as in the TTTF rig
- Replication of the cavity flow
- Cost-efficient and fast sourcing
- Using the resources available at the institute
- Simplified static HPT and LPT geometry

6.1.2 Given TCF Geometry

The given geometry shown in Figure 6.2 was provided by our research partner and set the baseline for the construction of a simplified test model for the recording of IR images and for the development of measurement methods. All geometries shown here are confidential and have been distorted for illustration. The optical access was designed for two planar windows in order to influence the flow at the shroud geometry as little as possible. The optical access was validated and approved by our research partner in the foreground during the design with the help of CFD and FEM calculations.

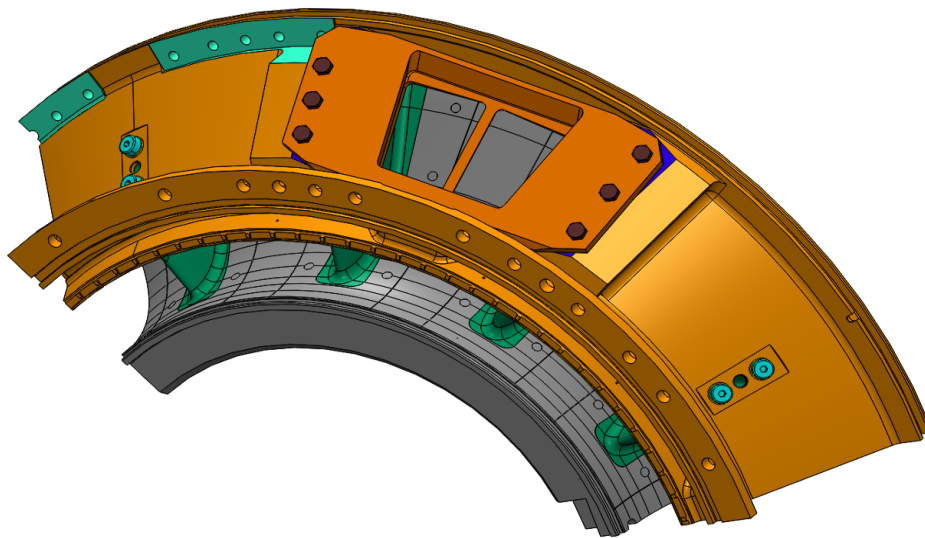


Figure 6.2: Given geometry. TCF geometry with optical access provided by the research partner.

6.1.3 Rapid Prototyping TCF

The first step in the design of the test rig was to simplify the provided geometry. An important requirement of the test bench was to maintain the original dimensions. It was then decided to design the test rig as a 45° sector in order to reproduce the optical access in the investigated channel in the best possible way.

Because of the complicated geometry the decision to use additive manufacturing as a cost-effective and fast solution was made. However, the size and the expected surface temperatures of the components placed high demands on 3D printing. The geometry was therefore trimmed at certain locations on the volume and divided into several components. Figure 6.3 shows the splitting into twelve separate parts. Holes for aligned pins were positioned on all resulting interfaces to define the geometric position in relation to each other in order to allow later assembly.

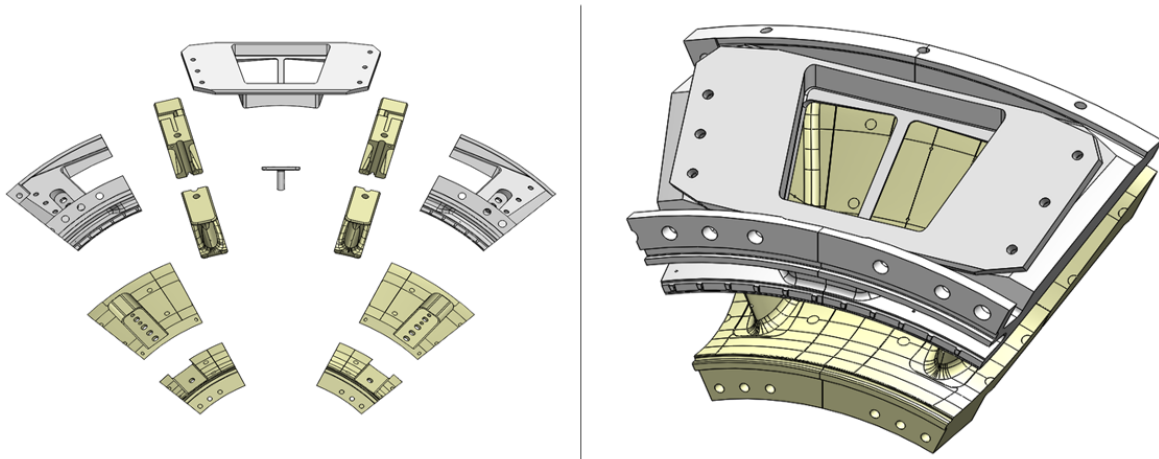


Figure 6.3: Geometry prepared for rapid prototyping. Stereolithography (STL) in yellow and Fused Deposition Modeling (FDM) parts in gray .

In Figure 6.3 you can see that two different 3D printing materials were used. The components shown in yellow are covered with heating foils so that they had to be designed for temperatures of up to 120°C. Stereolithography was used as an additive process using a high temperature resin for these parts. The components shown in grey represent the outer geometry of the flow channel and have to withstand less temperature, which led to the use of the more cost-effective Fused Deposition Modeling (FDM). The specifications of the materials used can be found in Table 6.1. After defining the 45° sector and splitting the parts for 3D printing, the individual components were adjusted in detail. Figure 6.4 summarizes these changes. Surface material was removed to compensate the thickness of the heating foils of 0.33 mm, the geometry was adapted for the cable routing of the heaters and channels for temperature sensors were added.

Table 6.1: Specifications of printing materials [15] [10]

Properties	High-Temp-Resin (STL)	GreenTEC-PRO (FDM)
Flexural modulus [MPa]	2620	4400
Flexural strength at break [MPa]	93.8	50
Elongation at break [%]	2.4	3.4
Heat Deflection Temp. @ 0.45 MPa [°C]	238	115
Heat Deflection Temp. @ 1.80 MPa [°C]	101	-
Notched impact strength [J/m ²]	24.2	4400
Thermal Expansion (0-150 °C) [$\mu\text{m}/\text{m}/^\circ\text{C}$]	74	-

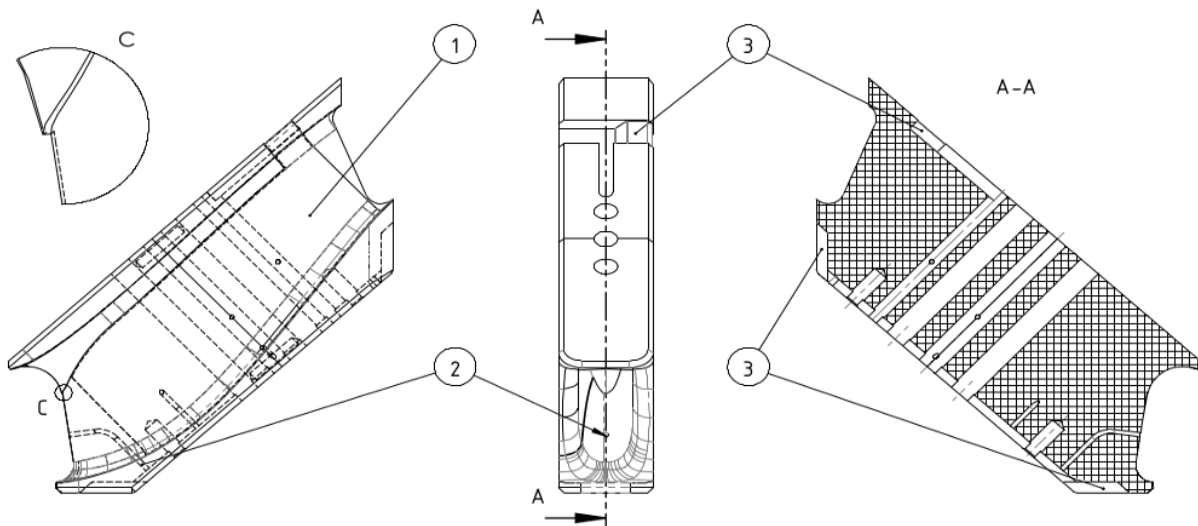


Figure 6.4: Adaptations strut geometry. 1: Adaptations for foil thickness of 0.33 mm; 2: Holes for thermocouples; 3: Cavities for solder joints and cabling of the heaters.

6.1.4 Defined Mounting

After the previous changes in the 3D printing geometry, the next step was to provide a reasonable fixture for the components. The basis for the test stand is a 40×80 mm aluminium profile, which on the one hand offers sufficient rigidity and on the other hand simplifies the assembly due to the multiply usable grooves. Figure 6.5 shows the definition of the printed parts. The surfaces marked in red represent a fixed and floating bearing arrangement. In the overall design, care was taken to avoid double fits and over-determinations.

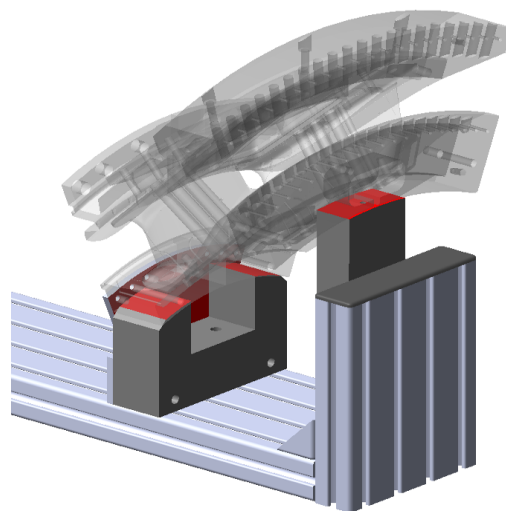


Figure 6.5: Defined mounting. Concept of a fixed and floating mounting.

6.1.5 Cavity Replication and Wake Generator

The next task was to design separate milled aluminium parts to replicate the cavities. The main focus here was on the simplest possible production using pocket milling. For the supply of the test stand with purge air, the compressed air of the facility with a maximum mass flow of 0.6 kg/s and 8 bar was used. During the design phase, care was taken to distribute the purge air as evenly as possible over the circumference of the cavities, using two symmetrical 1/4" ports per cavity.

Two FESTO one-way flow control valves type GR-1/2 were used to regulate the purge air and were connected upstream of the geometry. Figure 6.6 shows the volume flow range of these valves.

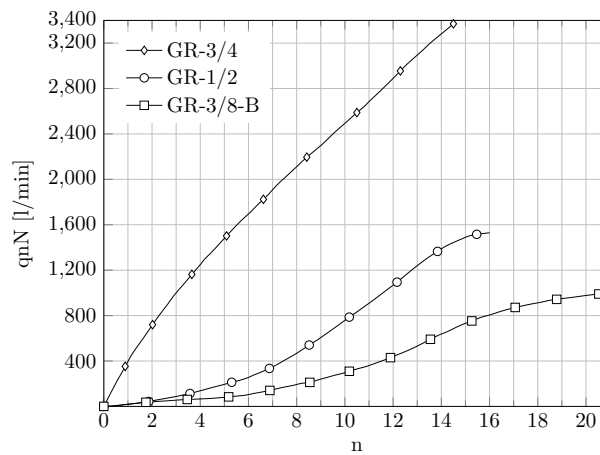


Figure 6.6: Standard nominal flow rate. q_{nN} at 6 bar \rightarrow 5 bar as a function of n spindle rotations. Data provided by the producer (Festo)[12]

Figure 6.7,6.8 shows the purge air guidance system of the adapted cavities highlighted in blue. The geometry at the cavity outlet has been retained.

The rods shown in Figure 6.7 were designed as interchangeable HPT wake generators in order to simulate wake flows on the heating foils later on. These inserts can be easily installed with or without pins.

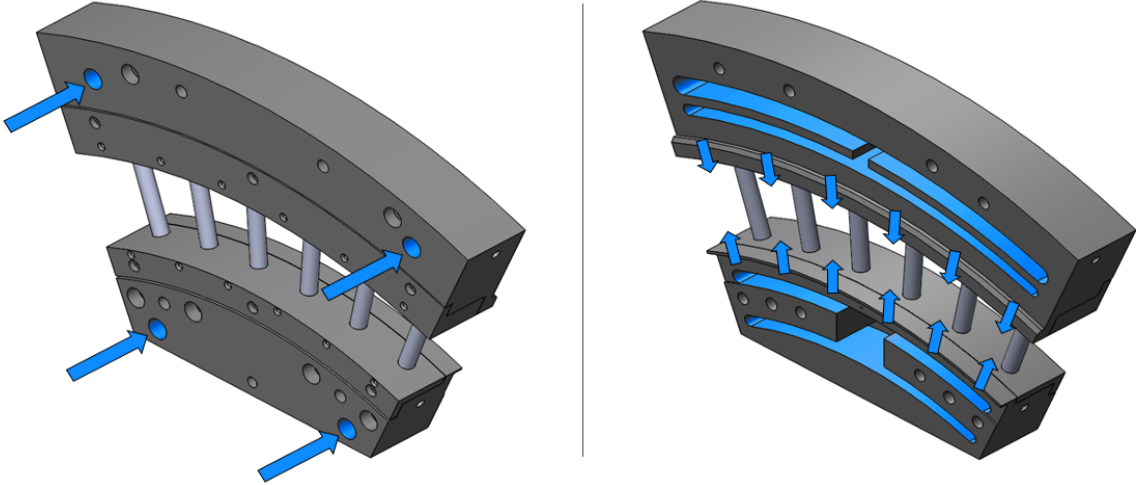


Figure 6.7: Cavity replication. Purge air guidance system highlighted in blue.

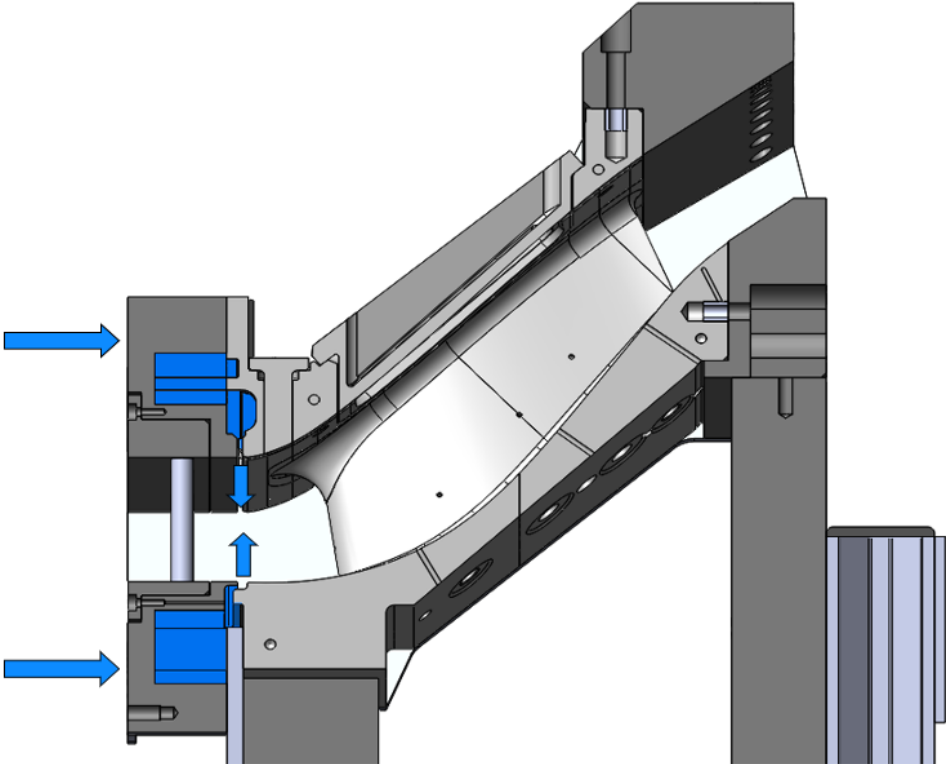


Figure 6.8: Cross-section of the purge air guidance system

6.1.6 Inlet Nozzle

The next requirement for the construction of the test bench was a uniform velocity distribution at the entrance of the sector rig. An existing subsonic compressor station at the institute was used to process the main air mass flow. This compressor delivers an estimated air mass flow of 1 kg/s. As there were no operating characteristics of this machine, this value was used for the first tests.

The challenge was to design a nozzle which connects the circular outlet cross-section of the compressor with the circular arc sector at the inlet of the test rig. The decision was made to separate the nozzle geometry into two sections, the cross-sectional transition was carried out in the front part of the geometry and the rear prismatic part of the nozzle was intended to calm the flow and ensure even flow conditions.

This geometry was developed iteratively using a simple CFD analysis. The boundary condition for the simulation was the previously defined mass flow of 1 kg/s at the inlet. The designed geometries were meshed automatically in a non-structured way (Figure 6.9), and refined on the wall to obtain qualitative results.

The results of the final geometry of the inlet nozzle are shown in Figure 6.10. As a result, a sufficiently smooth velocity profile at the outlet was achieved. The practical implementation of this nozzle as a sheet metal construction is shown in Figure 6.11. All designed sheets had to be developable for manufacturability. In order to avoid possible problems during production, communication was already established with the manufacturer of this nozzle during the design phase.

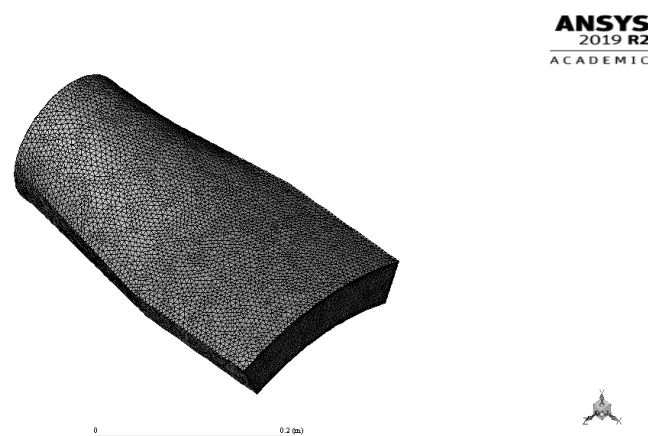
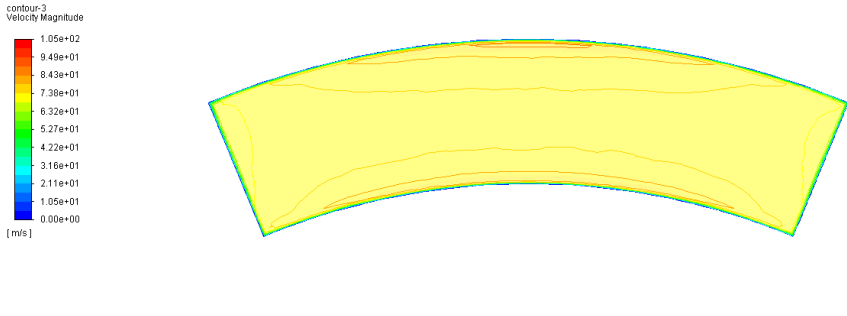


Figure 6.9: Inlet nozzle mesh. Unstructured mesh generated by ANSYS meshing.

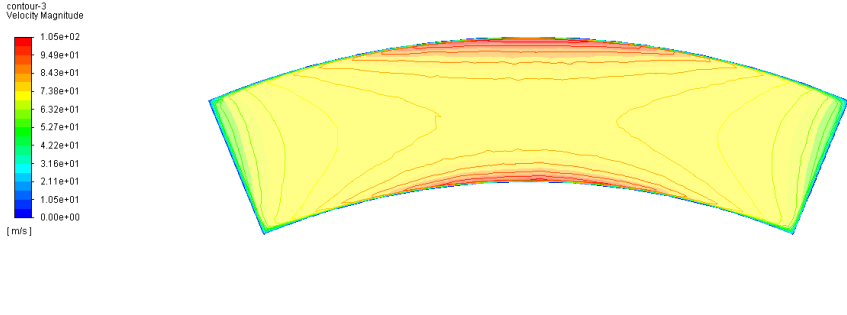


ANSYS
2019 R2
ACADEMIC



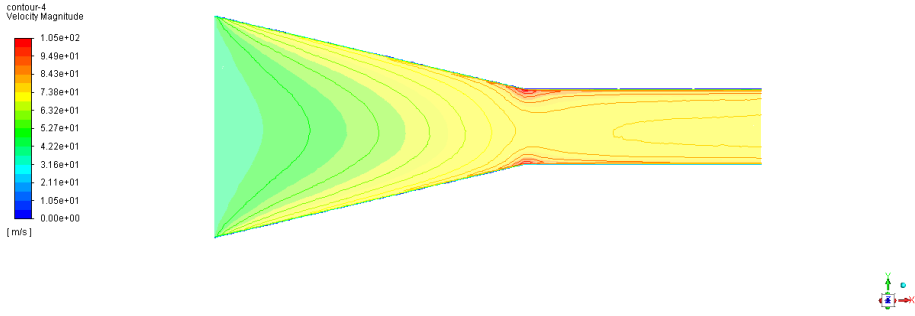
(a)

ANSYS
2019 R2
ACADEMIC



(b)

ANSYS
2019 R2
ACADEMIC



(c)

Figure 6.10: Velocity profiles for the optimized inlet nozzle. (a) Inlet sector rig, (b) Section in the transition area, (c) Crosssection. The simulation was performed with ANSYS 2019 R2 Academic

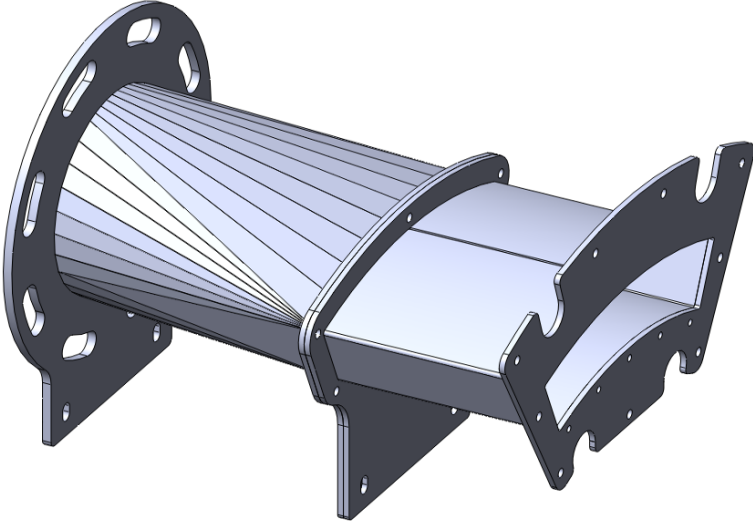


Figure 6.11: Nozzle sheet metal construction. Divided into two parts for cross-sectional transition and rectification.

6.1.7 Outlet

The last step in the construction was the simulation of a pressure difference in the field of measurement. In order to achieve a certain accumulation of the flow, a simple solution was searched for to replace the obstruction of the LPT. The decision to use cylindrical rods was made, in detail standard dowel pins were used. For the selection of the next best diameter, the volumetric blockage of the original LPT was measured in CAD and determined accordingly. Figure 6.12 shows the result of this design.

The results of the construction can be found in chapter 6.3.

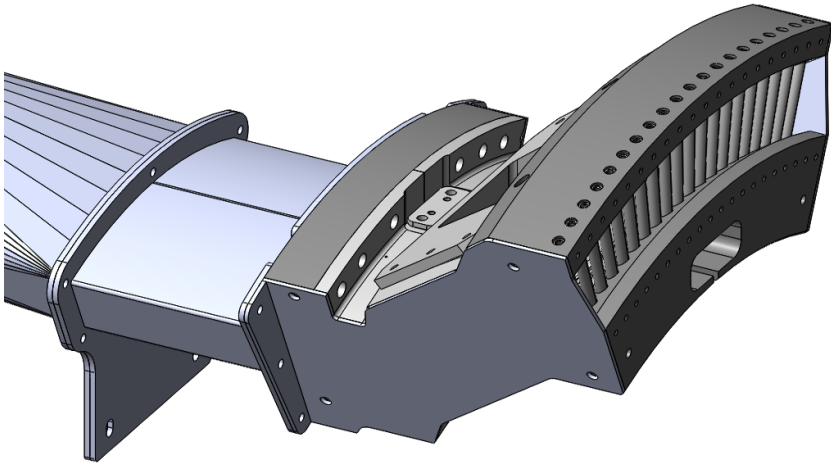


Figure 6.12: Outlet. Rod structures for flow accumulation.

6.2 Assembly

After the design was completed, quotations for all components were obtained, compared and ordered. The required parts could be separated into groups:

- Standard parts
- Sheet metal parts
- 3D printed parts
- Milled parts

The first step in the assembly process was to recombine the 3D printed parts into the entire geometry. Figure 6.13 shows the printed parts produced by stereolithography after a first alignment. The positioning pins and the neighbouring milled parts provided the reference. Irregularities in the printing process, such as slight distortion, were reworked and the parts then glued together with epoxy resin. In the course of gluing the split parts, all thermocouples provided were also fixed at the prepared locations (More details in the following instrumentation section). Threads were cut into the plastic at non-critical points, thread inserts were used at other positions.

After completing rework, the entire test stand was passed on to ATT Advanced Thermal Technologies. The heating foils developed by them were then applied precisely. The modifications to the print parts helped to position the foils. Figure 6.14 shows the printed geometry with the six heating foil segments applied. All irregular edges and transitions on the surface were smoothed with heat-resistant silicone before coating. The reference points required for later image processing were masked by ATT.

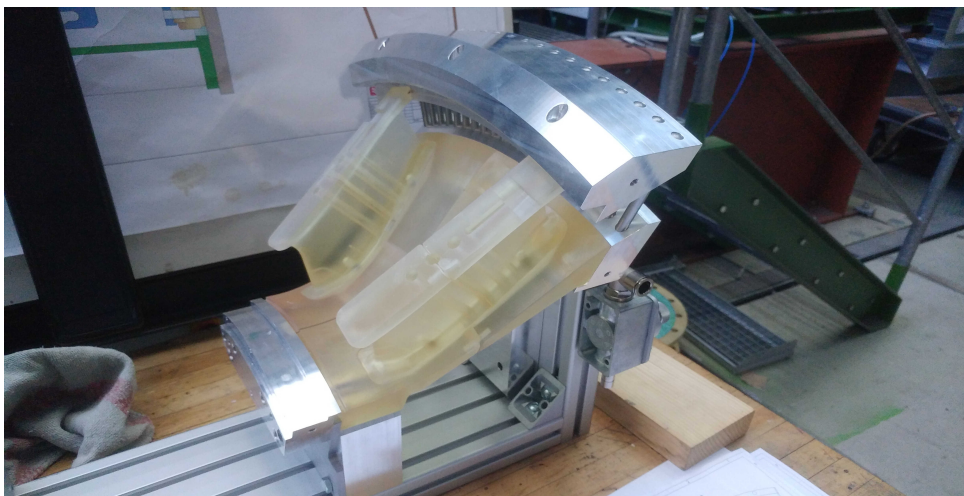


Figure 6.13: 3D printed TCF geometry. First alignment of the printed parts before glueing.

Figure 6.14 shows the printed geometry with the six heating foil segments applied. All irregular edges and transitions on the surface were smoothed with heat-resistant silicone before coating. The reference points required for later image processing were masked by ATT.

The correct surface coating is the basis for quality thermographic measurements on surfaces. The NEXTEL[®] Velvet-Coating 811-21 [26] was used because of its excellent properties for this usage. This coating offers an angle insensitive emissivity over a wide range. Figure 6.15 shows the surface after application of the coating.

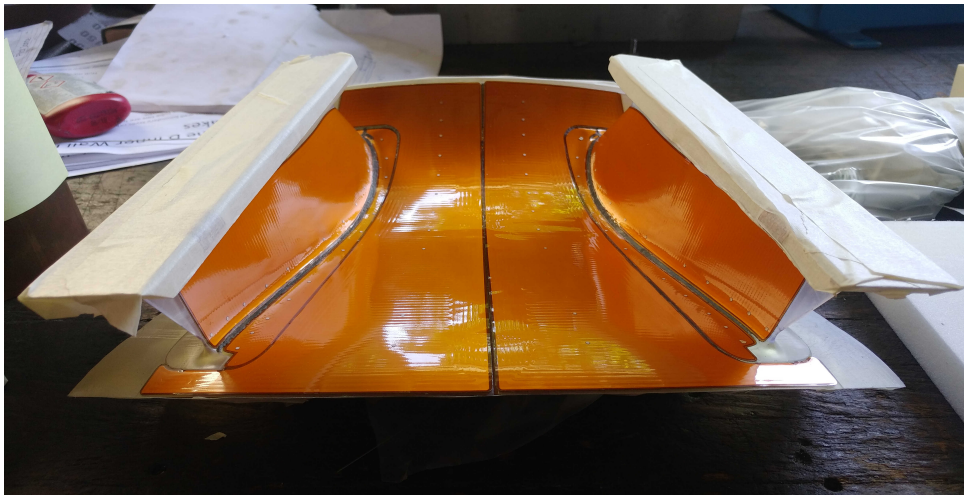


Figure 6.14: Heating foils. Heaters applied to the TCF geometry.

Figure 6.15 shows the test rig after painting and wiring. All cables for the power supply of the foils are led through the strut geometry to the inside.

In order to quantify errors during the application of the foil, an attempt was made to measure the points using a 3-axis milling machine at the institute using the available tools (Figure 6.16). The results of this measurement are summarized in Table 6.2. In Figure 6.17 the rig was assembled for first commissioning test.

Table 6.2: Measurement of reference points

point	defined point [mm]			measured point [mm]			deviation [mm]		
	X	Y	Z	X	Y	Z	ΔX	ΔY	ΔZ
1.1	-61.95	184.66	-502.95	-61.6	185.37	-502.50	-0.30	-0.71	-0.45
1.2	-58.98	188.35	-513.28	-58.92	189.05	-513.29	-0.07	-0.70	+0.01
1.3	-58.04	193.65	-525.12	-58.01	194.41	-525.16	-0.04	-0.76	+0.04
...

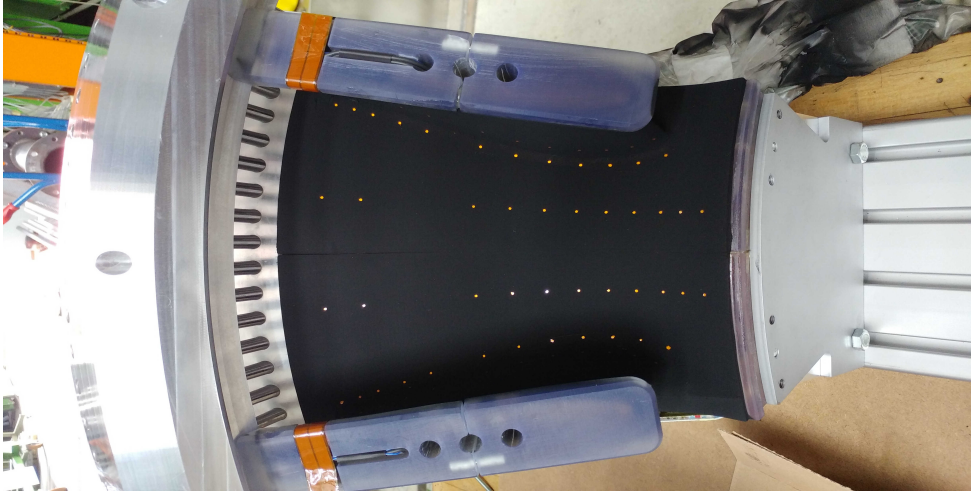


Figure 6.15: Reference Points on the coated TCF geometry

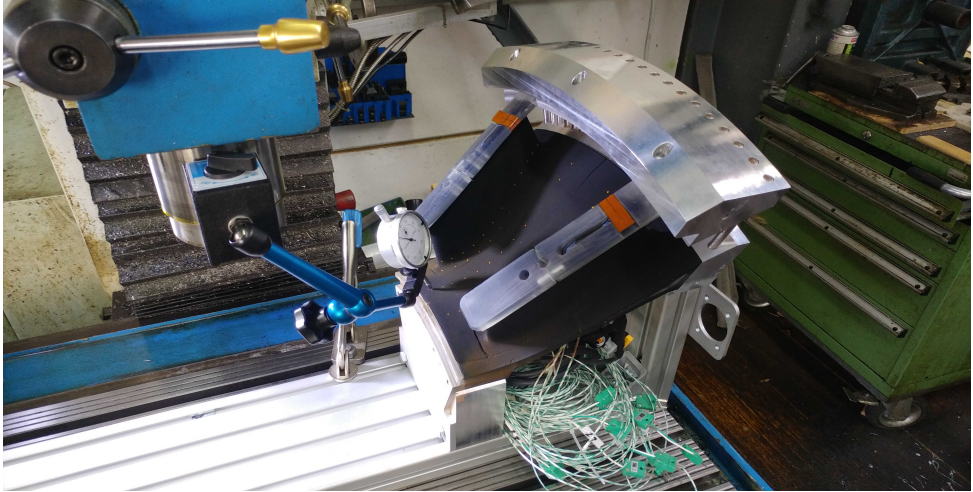


Figure 6.16: Measurement of the actual point coordinates

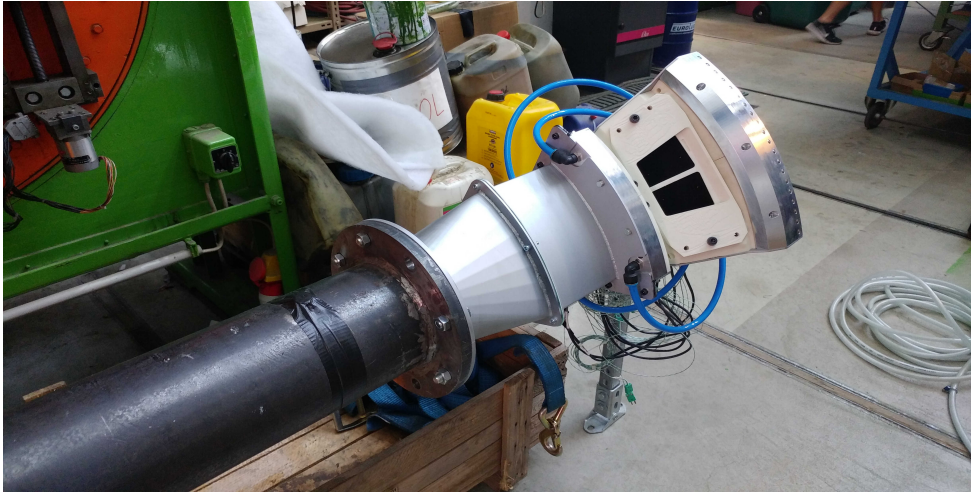


Figure 6.17: Assembled and connected test rig

6.3 Main Components

Figure 6.18 shows the cross-section of the test rig and all its components. The main flow inlet (1) is connected to our existing subsonic compressor station by a 150 mm diameter tube to supply the rig with compressed air. A following nozzle (2) and rectifier (3) ensure uniform inflow conditions at the inlet. The subsequent test section of the rig consists of a 45° sector of an engine-representative turbine centre frame (TCF).

At the entrance a replaceable insert with rods (5) was provided for the replication of HPT wake structures.

Two struts with a pitch of 30° then form the flow channel to be investigated (8). This S-shaped duct was equipped with custom-made heating foils at the hub geometry and at the side walls of the struts. These heating foils are supplied with a known heat flux distribution. The generated surface temperature with heated foils and flow can now be measured by thermography through a barium fluoride (BaF₂) optical access (9). The surface to be measured was coated with a special paint-coating. This coating from Nextel (NEXTEL® Velvet-Coating 811 – 21 [26]) has particularly good emissivity properties and is commonly used for thermography measurements.

Another feature of the rig is the replication of the purge flow at the hub and shroud geometry (Figure 6.18; Pos.4,6). While the design and placement of needle valves for the

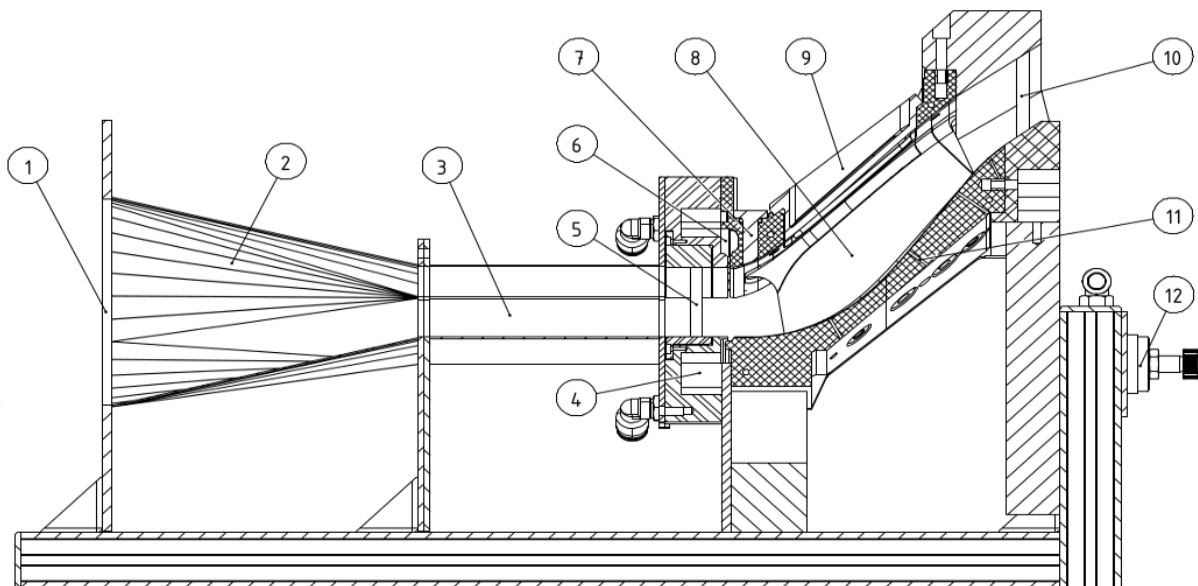


Figure 6.18: Test rig cross section. 1: inlet; 2: nozzle; 3: rectifier; 4: hub cavity; 5: wake rods; 6: shroud cavity; 7: blind plug; 8: strut geometry with heating foils; 9: optical access; 10: blockage rods (LPT); 11: 3D printed TCF geometry adapted for heating foils and thermocouples; 12: throttle valve for purge air.

purge air supply was still part of this work, the conditioning of purge air was developed outside this thesis. A general schematic flow path of the test bench can be seen in Figure 6.19.

For the recording of pressure profiles and temperatures at the inlet at operating point conditions, the original geometry of the measuring port at the 3D printed geometry was preserved (Figure 6.18; Pos.7). Measurement devices for pressure and flow recording in this test rig designed and constructed in this thesis was available at the TTTF and was used in this thesis. A list of the instruments used is provided in Table 6.3.

Table 6.3: Provided instruments.

Instrument	Description
Pressure transducer	Scanivalve <i>DSA3218</i>
Five-hole probe	Manufactured by the IST, Aachen University
Temperature Acquisition	VTI Instruments Corp. EX1032A
Orifice plate	Flow rate measurement

The outlet geometry (Figure 6.18; Pos.10 LPT) is simplified on rod structures for a similar flow blockage compared to the large test bench.

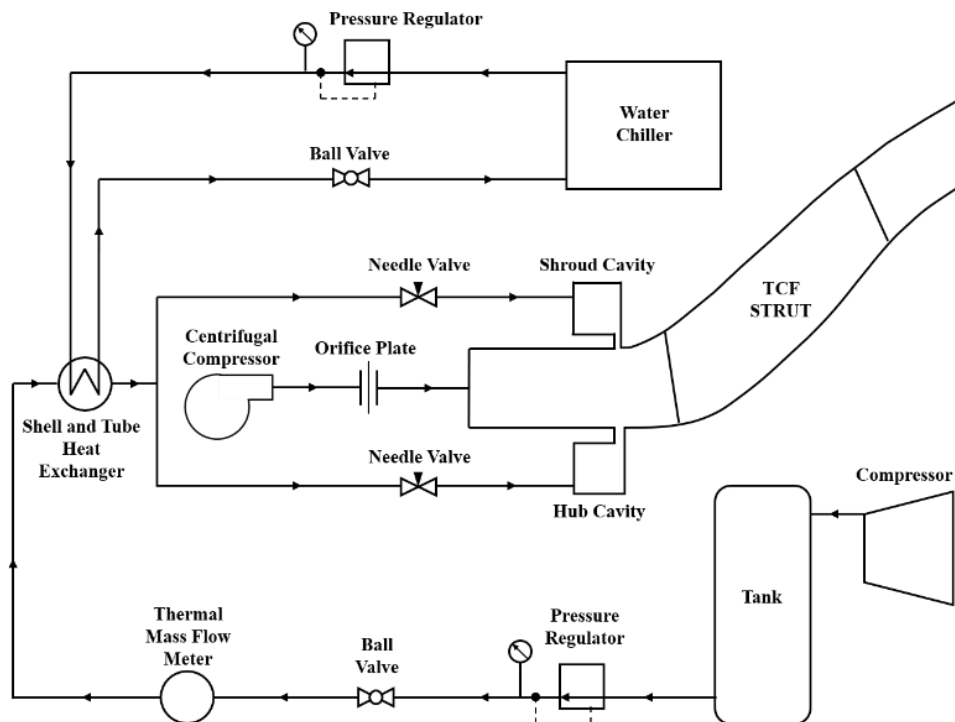


Figure 6.19: Schematic diagram of mainstream and purge flow networks

The main component dimensions and their different views are shown in Figure 6.20.

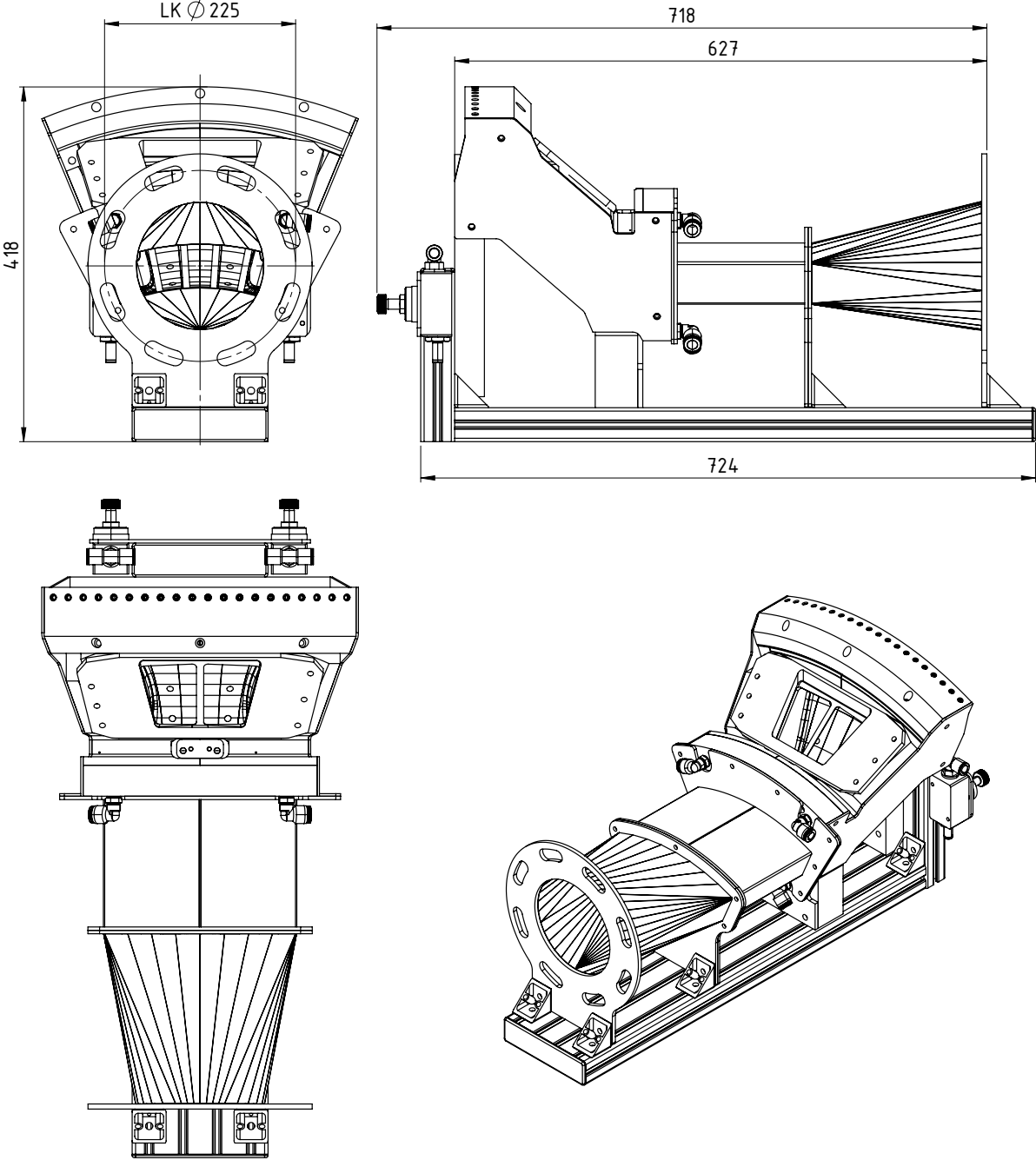


Figure 6.20: Test rig CAD sketch with basic dimensions

6.4 Instrumentation

The test rig was instrumented with thirteen thermocouples in the region of the strut and hub geometry under the heating foils to provide additional reference temperatures to the thermographically measured surface temperature. Figure 6.21 shows the positions of the built-in temperature probes and Table 6.4 shows their specifications.

The signal of the thermocouples is acquired using a VTI Instruments Corp. EX1032A acquisition system with an uncertainty of ± 0.2 K provided by our research partner.

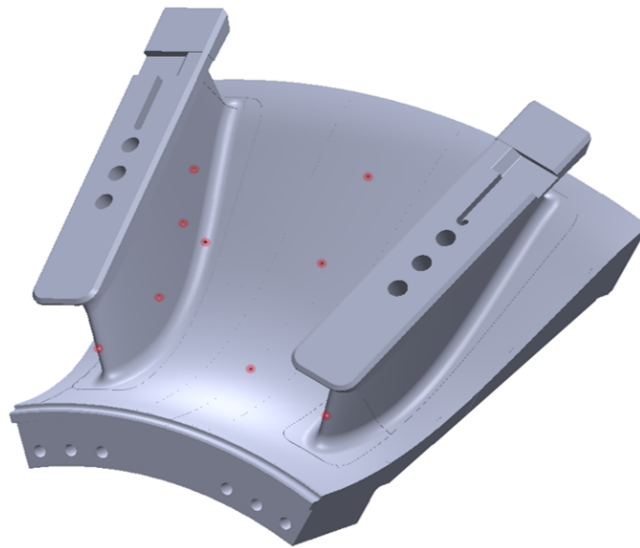


Figure 6.21: Thermocouple positions

Table 6.4: Thermocouple specifications.

Manufacturer	RS
Stock No.	621-2170
Type	Cable thermocouple Type K hot junction
Temperature range	-50°C to 1000°C
Temperature accuracy	$\pm 1.5^{\circ}\text{C}$ at $-40^{\circ}\text{C} < T < 375^{\circ}\text{C}$
Insulation	Glass fiber
Section	0.07 mm^2
Cable length	2000 mm
Standard	DIN 60584
Time constant at 63%	0.7 sec
Junction diameter	0.3 mm

6.4.1 Thermocouple Calibration

The thermocouple calibration was performed using a block calibrator shown in Figure 6.22 (see table 6.5 for specifications) and a calibrated PT-100 reference thermometer. The thermocouples were heated to several temperatures in the range of 40 to 130°C under ambient conditions, then the temperature was maintained steady and compared to the reference temperature. The resulting calibration curves for the temperature range just described are shown in the appendix.



Figure 6.22: Block Calibrator. Images courtesy of [31]

Table 6.5: Block calibrator specifications. [31]

Manufacturer	Omega
Measuring zone	0 to 50 mm from base of well
Depth of well in insert	114.3 mm
Temperature range	20°C above ambient to 425°C
Temperature accuracy in measuring zone	±0.3°C
Temperature uniformity in measuring zone	±0.2°C at 300°C
Temperature uniformity in measuring zone	±0.6°C at 450°C
Temperature stability after 1 hr	±0.06°C at 450°C
Display resolution	0.1°C
Heat up rate	15 minutes; 20°C to 400°C
Cool down rate	25 minutes; 400°C to 100°C

6.5 Commissioning Test

A 16-channel, Scanivalve *DSA3218* differential pressure transducer with a range of ± 2.5 psi (± 0.17 bar) and accuracy of $\pm 0.08\%$ of the full scale was used for the pressure measurements to determine the operating point and the first commissioning runs. The specifications are listed in Table 6.6.

For the mass flow at the inlet, pressure measurements were carried out on an orifice plate. The position of the mass flow measurement is shown schematically in previous Figure 6.19. The maximal main stream mass flow of the subsonic compressor was reached at about 0.54 kg/s , which led to an inlet Mach number of $M = 0.08$ and a Reynolds number of $Re_c = 4.25 \times 10^5$ based on the strut chord length.

Further pressure measurements were carried out in plane B by a traversable five-hole probe (manufactured and calibrated by the IST, Aachen University) to validate flow conditions at the inlet. Pressure measurements were taken in different radial locations with two mass flow rates. The mass flow rate R_m represents the ratio between purge and main mass flow. Figure 6.23 shows the position of measurement plane B in two views.

The results summarized in Figure 6.24 show total pressure, total temperature, axial and circumferential velocity along the measurement axis shown before. The results were plotted along a dimensionless radius representing the channel height at the inlet. The inlet nozzle designed in section 6.1.6 produces a velocity profile matching the requirements provided by the companies involved. The measured total pressures showed constant values across the cross-section of the channel with an expected pressure drop close to the hub and shroud wall which also met the expectations.

Table 6.6: Pressure sanner specifications. [33]

Name	Scanivalve <i>DSA3218</i>
Full scale long term accuracy	$\pm 0.005\%$
Channel sampling speed	850 Hz
Sensor pressure range	$\pm 2.5 \text{ psi}$
Static accuracy	$\pm 0.08\%$
Operating Temperature	0°C to 60°C

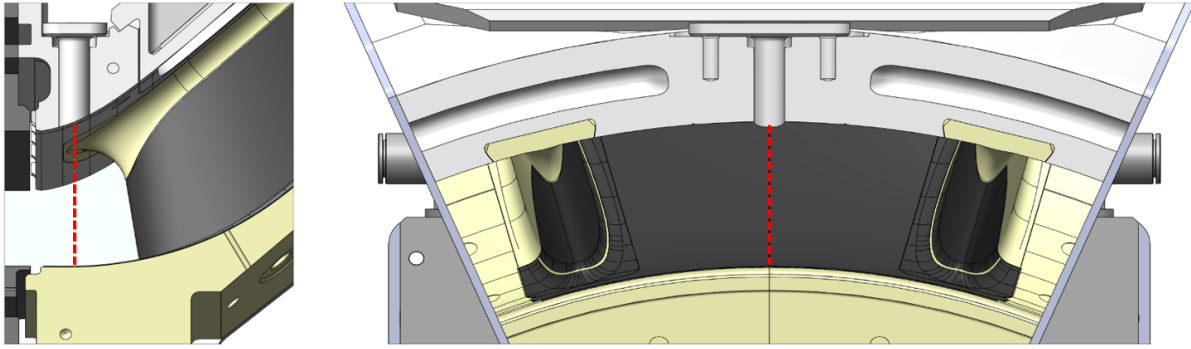


Figure 6.23: Five-hole probe measurement position. Measurements taken in plane B along the red dashed line in the center of the flow channel.

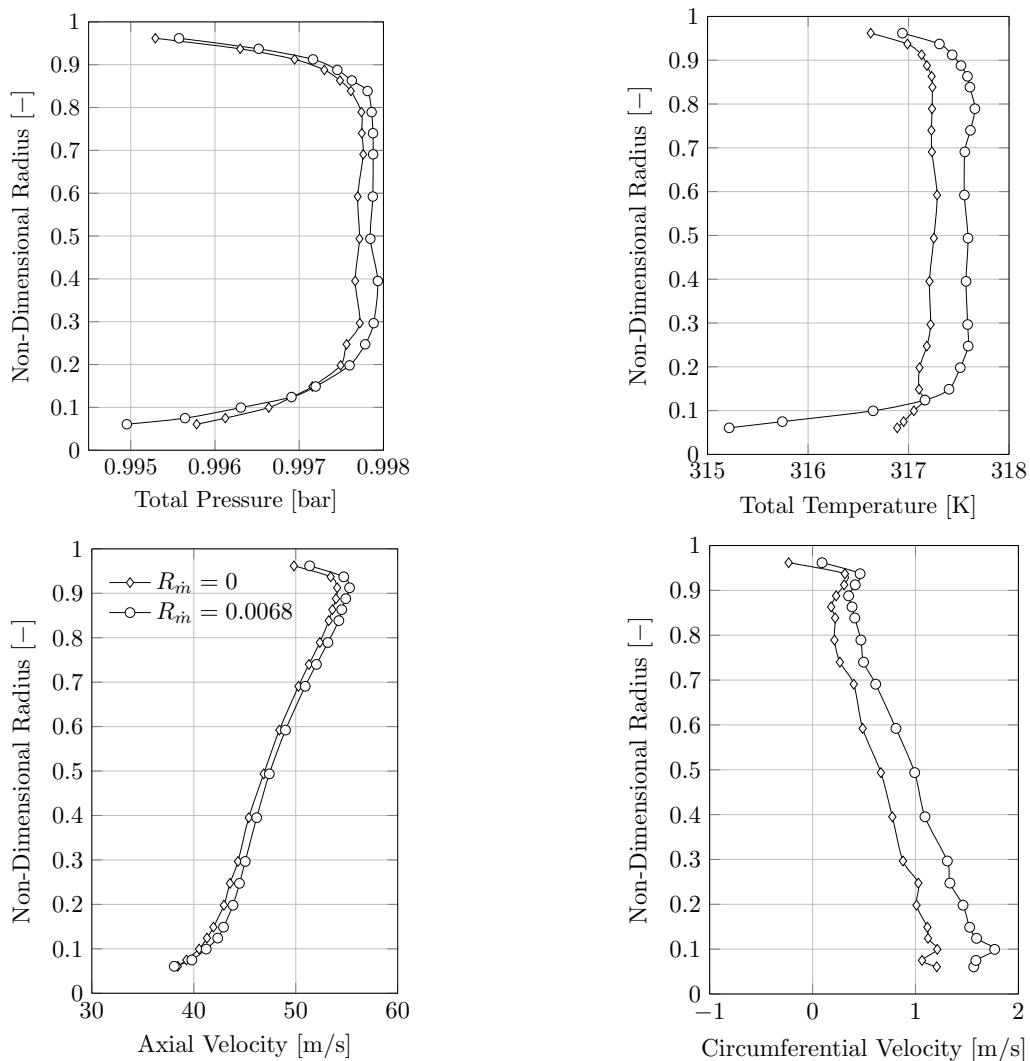


Figure 6.24: Five-hole probe measurement results. Total pressure, total temperature, axial and circumferential velocity in plane B with and without purge flow.

7 Results and Discussion

In this chapter, the quality of the developed image mapping procedure and its effect on the measurement accuracy of temperature measurements in the TCF will be discussed. For the evaluation a series of tests were performed on the designed test rig. The recorded infrared images were then postprocessed for validation and discussed with regard to error estimation.

Parts of this thesis are submitted to the ASME Turbo Expo 2020 conference. The thermographic recordings presented in this section are taken from the heat transfer analysis carried out in this manuscript, but were recorded and analysed by the author of this thesis. A special focus was placed on the errors inherent to this method proposed by the author.

All data for the following analyses were taken from a specific test case, the operating point settings used for this purpose are listed in Table 7.1. For a more detailed description of these values, please refer to the commissioning of the test rig in chapter 6.5.

Table 7.1: Operating conditions

Mass flow rate main , \dot{m}_M	0.54 kg/s
Mass flow rate purge , \dot{m}_P	0.00184 kg/s
Free-stream mach number at inlet, M	0.08
Reynolds number, Re_c	4.25×10^5
Mass flow ratio, $R_{\dot{m}}$	0.0034
Electrical power density of the heaters, p	5700 W/m ²

7.1 Transformation of two Representative IR Recordings

The quantification of the transformation quality is now to be discussed using two transformed temperature fields. These two recordings show parts of the more difficult to access strut side wall and the hub geometry. All essential aspects of the developed post-processing method are discussed in this example and have to be considered for the general application of this method.

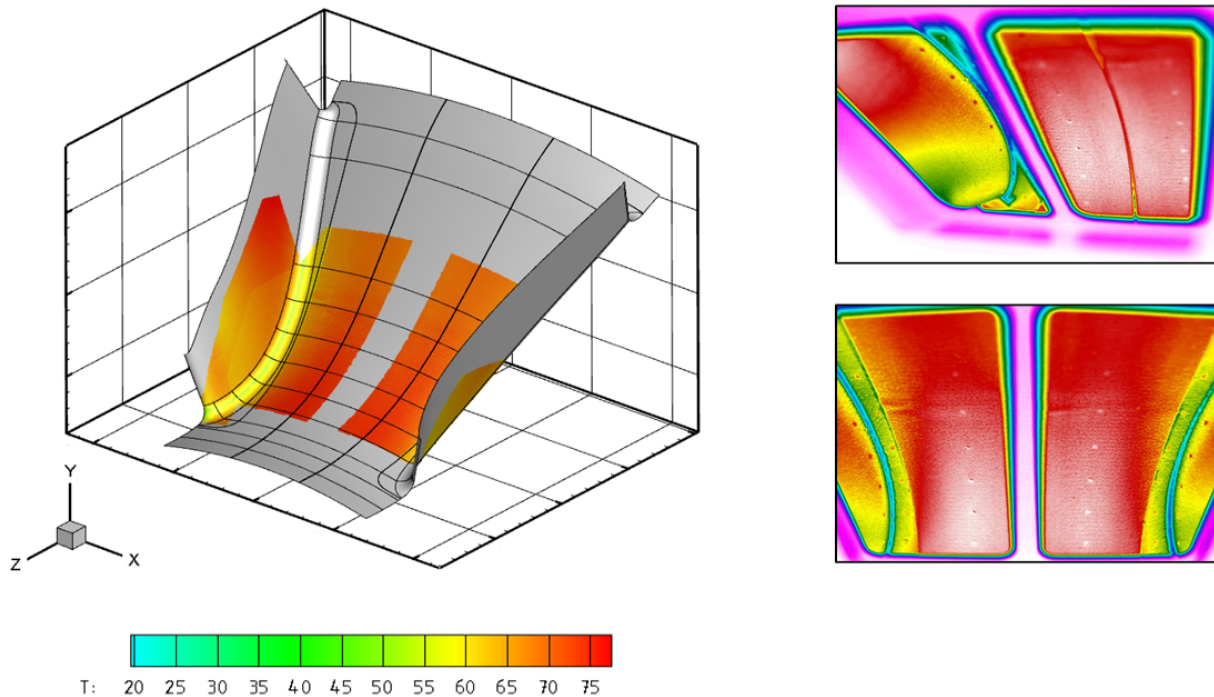


Figure 7.1: Data visualisation of IR images (Temperature scale in Celsius).

Figure 7.1 illustrates the data visualization as a three-dimensional temperature field of two mapped IR images (a) and (b). Essential areas of the two-dimensional images are clearly recognizable in the three-dimensional field, excluding irrelevant or unusable areas such as the recognizable outlines of the window frame or blurred areas.

In Figure 7.2, an adapted nonlinear color map makes important areas of the measurement more visible. Since the complete detection of the temperature field by a limited optical access is only possible by several single images, there are challenges in areas of overlapping. Since temperature values from several two-dimensional thermographic images are available for these overlaps, suitable averaging procedures must be provided here. Within the scope of this work, temperatures in intersection areas were the mean value of all available temperatures without any weighted filters, which leads to recognizable discontinuities (Figure 7.2, (a)). Temperature jumps of about 0.3 K were consequently occurred. The

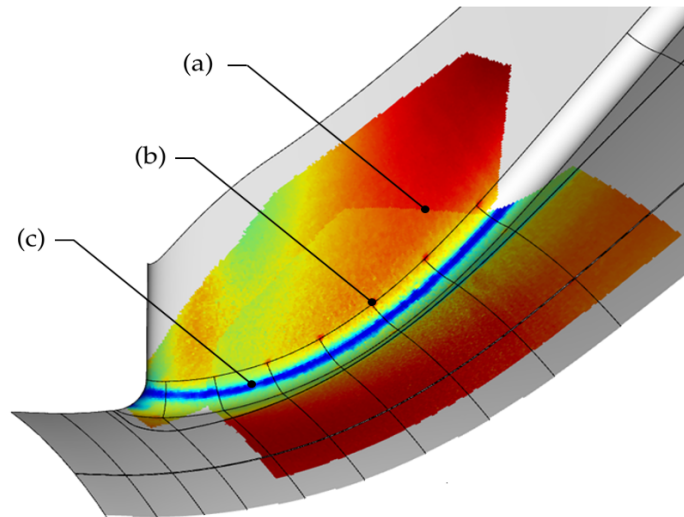


Figure 7.2: Significant areas of the merged temperature field. (a) Overlapp, (b) Reference point, (c) Heater joints

development of further weighted averages at the region of borders was envisioned in the Matlab routine, but was not carried out within the scope of this work.

Further areas that cannot be used without post-processing are the necessary reference points (Figure 7.2, (b)), which have different emissivity values than the surface measured. Temperature measurements at these locations are thus shifted by up to 10 Kelvin. Since the position and the surrounding temperatures are known, these areas can be reworked and made usable with additional post-processing.

All blue marked areas and their influenced environment in Figure 7.2 (c) are to be rejected. These areas contain the joints of the heating elements that are related to the heater design. No heating power is delivered here.

7.2 Spatial Mapping Error

In order to quantify the quality of the transformation, data about the calculated virtual camera parameters and a reprojection error are obtained by the Matlab routine for each individual image. The focal length, skew, principal point and reprojection error of the image are shown in table 7.2 for the two discussed images.

For a better understanding of the reprojection error mentioned in section 3.2.7, this error will now be explained using one of the two discussed images. Figure 7.3 (b) shows the manually selected reference points as green circles. From these selected points and the

Table 7.2: Transformation quality. Estimated intrinsic parameters and reprojection error in pixel units.

	f_y	f_x/f_y	skew	x_0	y_0	min	max	mean error
image (a)	1601.8	1.032	-19.4152	296.2	354.0	0.291	1.273	0.766
image (b)	1312.1	1.048	-17.6105	201.1	349.9	0.1647	2.550	0.949

known 3D coordinates of them in space, a connection between image and object coordinates could be established with the Direct Linear Transformation (DLT) algorithm. Subsequently, the object coordinates of the reference points were brought into the image plane with this obtained transformation matrix. The transformed reference points from the spatial coordinates are marked as red crosses in Figure 7.3.

The Euclidean distance between transformed object points (red cross) and manually selected image points (green circle) is defined as the reprojection error.

Figure 7.3 (a) shows the largest reprojection error for this case with an offset of 2.55 pixel. The statistical evaluation of all reference points is shown in Figure 7.3 (c), where the blue bar indicates the largest error that has just been discussed.

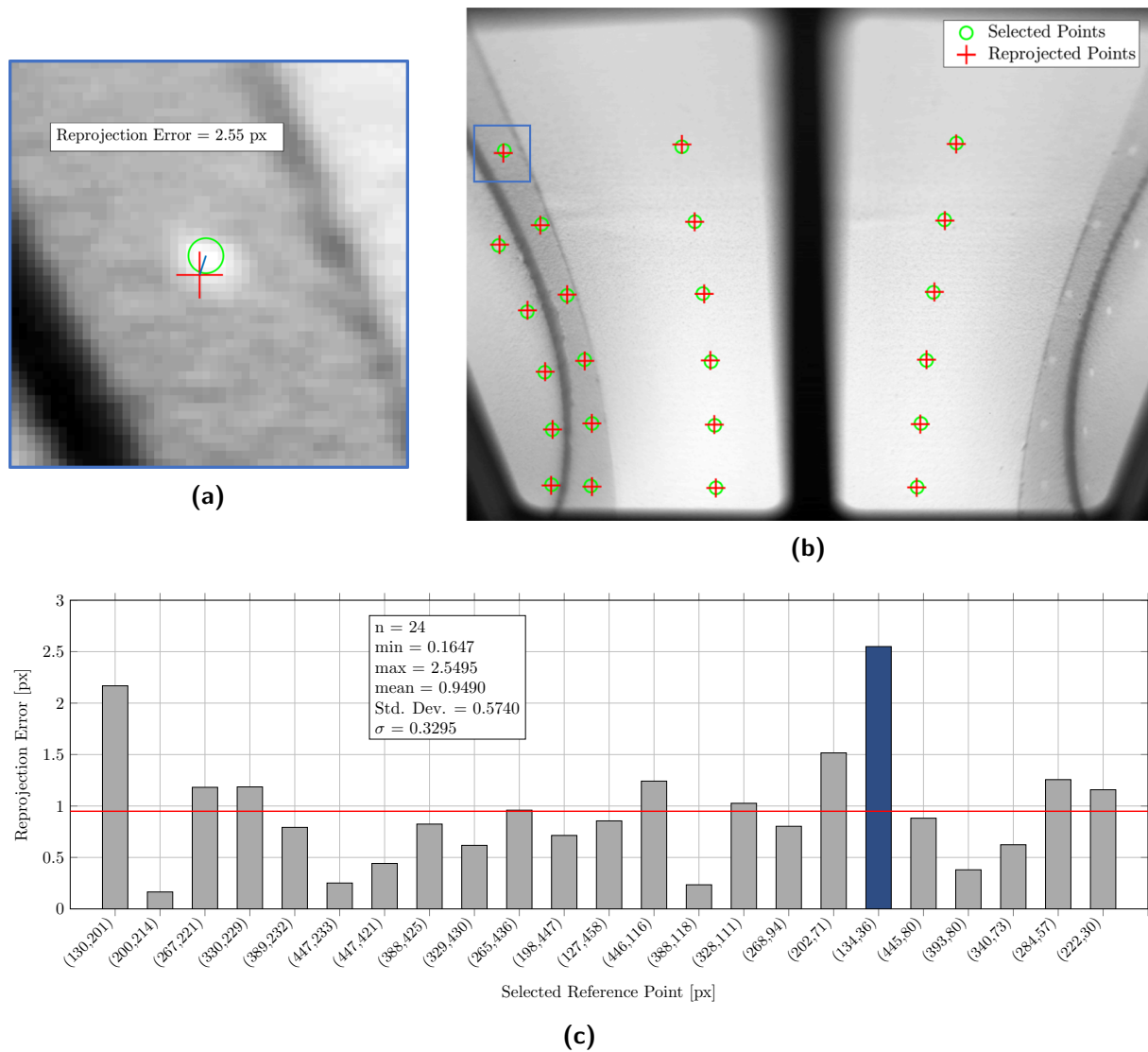


Figure 7.3: Reprojection Error. (b) Infrared image with manually selected reference points (green) and transformed spatial reference points red; (a) Euclidean distance between selected and transformed point; (c) Statistical evaluation of reprojection errors.

7.3 Influence of Spatial Error on Temperature Measurement Accuracy

In order to determine the effect of the spatial error of the mapping algorithm on the temperature measurement, the temperature gradients occurring in the measurement area had to be examined first. For this purpose, high gradient areas and measurement situations were selected. Figure 7.4 (a) presents an infrared image of the leading edge of the strut geometry. Especially in this area, the largest gradients occur in the experimental setup due to flow separation phenomena. For better orientation, reference is once again made to Figure 7.2, which shows exactly this transformed thermography image on the side wall.

For the following discussions, two temperature profiles along a straight line with the utmost possible changes to the image were recorded and observed more closely. The two measurement lines are marked in blue and cyan in Figure 7.4 (a).

The temperature profiles in Figure 7.4 (c) must now be discussed. There are strong gradients along the cyan line, but these are irrelevant because of the features already discussed in section 7.1, such as the impact of the heaters. Temperature measurements in these regions are not representative and cannot be used for further calculations.

For further considerations, the measured blue temperature profile 7.4 (c) on the strut side wall is used. An average gradient of about $0.025K/px$ between pixels 50 and 180 can be calculated immediately for the trend line. These small gradients would mean that a misalignment of one pixel would lead to temperature variations that are no longer noteworthy. Very small pixel steps can lead to much higher gradients. To evaluate the gradient, the curve was numerically differentiated using the following formula (right-hand side quotient):

$$f'(x) \approx \frac{f(x+h) - f(x)}{h}$$

The results of this derivation with a step size of $h = 1$ px are shown in Figure 7.4 (d). One can see that the temperature values along the line can change up to 0.55 K/px. A reprojection error of only 1 px can lead to errors of more than 0.5 Kelvin, whereby these high gradients are due to the noise of the temperature value. When discussing the gradients in 7.4 (d) the noise inherent to the signal is increased due to differentiation of the signal. Possible reasons for this noise are degradation by flow or contamination of the matt Nextel coating by the lubricated compressed air. Figure 7.4 (b) clearly shows the rough structure of the coating even in infrared. For further examination, this effect must be considered and, if possible, corrected by smoothing the signal.

Figure 7.4 (e) summarizes the differentiation with different step widths. The maximum temperature gradient decreases as the step width of the differentiation increases. The noise in the temperature plot is smoothed with increasing step width.

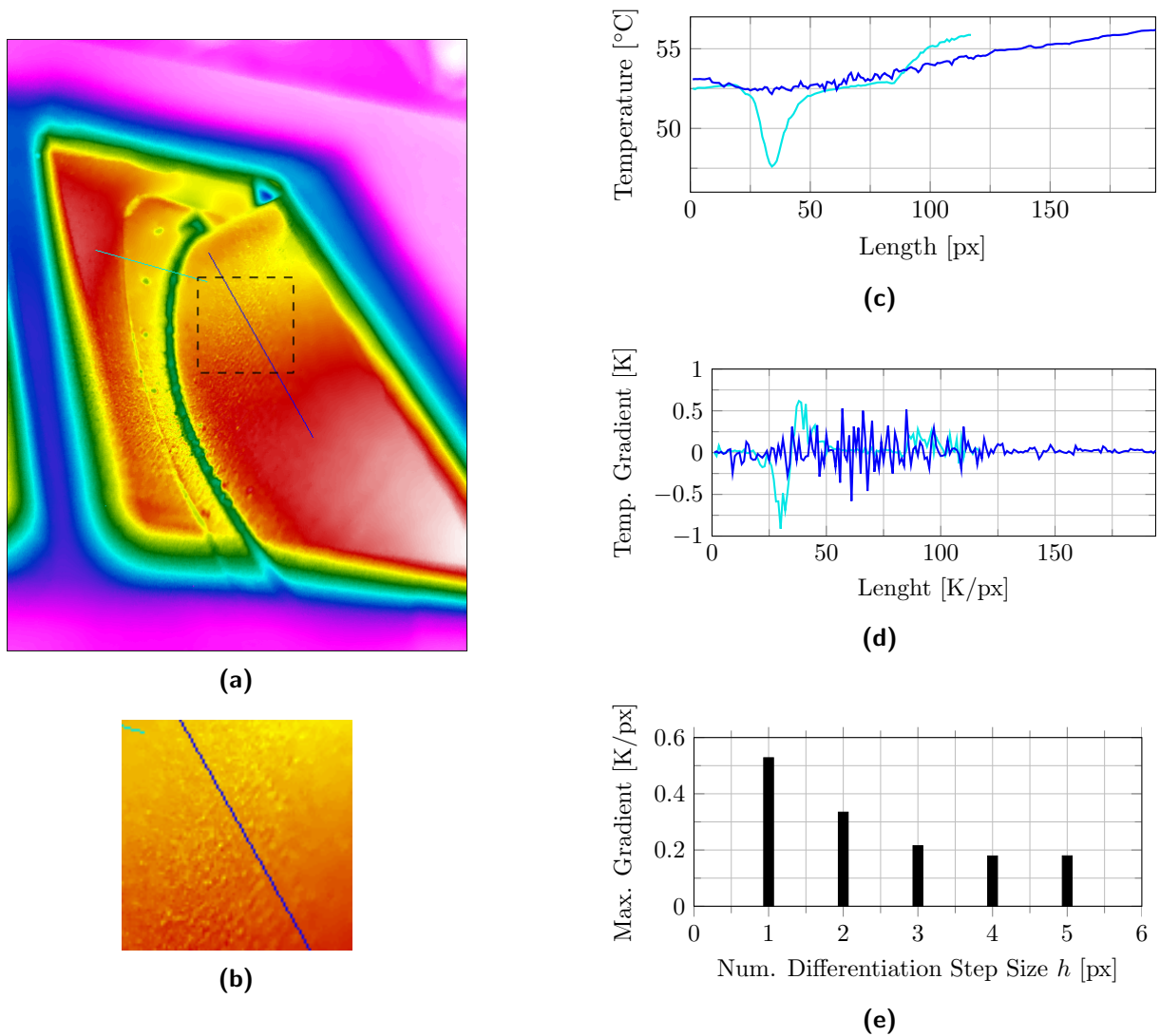


Figure 7.4: Occuring Temperature Gradients. (a) Infrared Image with lines of interest; (b) Surface structure visible in the IR band. The section plotted is indicated by a square in (a); (c) Temperature profiles; (d) Temperature gradients; (e) Maximum gradients regarding different numerical differentiation

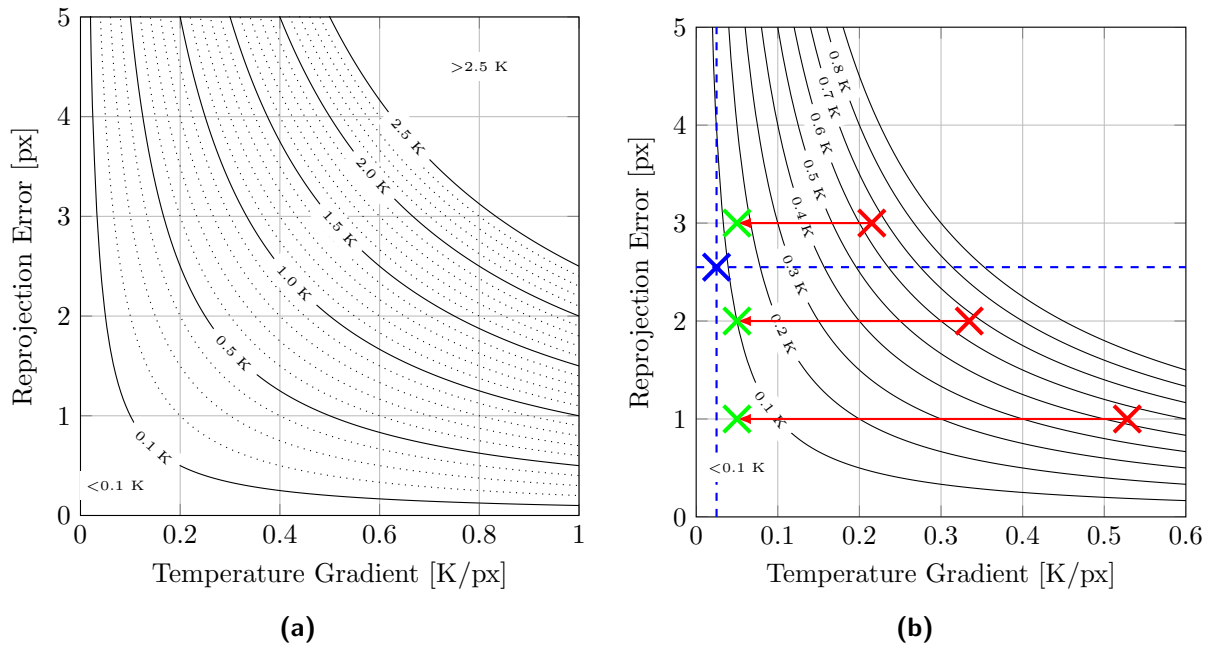


Figure 7.5: Temperature error caused by misalignment of the provided mapping algorithm.(a) Error estimations plot; (b) Example of error estimation

To get an impression of the relationship between reprojection error (in pixel) and temperature measurement error (in K), the reprojection error was plotted over the expected temperature gradient in Figure 7.5 (a). This graph makes it possible to estimate the measurement error. Gradients can be estimated as before from the infrared images, which can be used for individual measurement error estimations in different locations.

Figure 7.5 (b) shows the application of the previously determined values for the reprojection error and discussed local temperature gradients in such a diagram. The maximum reprojection error of 2.55 px shown in Figure 7.3 was entered as horizontal, the estimated gradient of the temperature trend line from figure 7.4 (c) as vertical with 0.025 K/px. In the first estimation temperature deviation results below ± 0.1 K (blue marker) due to local misalignment of the mapping algorithm.

However, the previously discussed noise in the temperature profiles might lead to significantly higher errors. The maximum gradients determined in Figure 7.4 (e) for the respective disposition were entered in red. Temperature deviations of about ± 0.65 K might then occur if no smoothing is performed.

A reduction of the temperature noise on gradients in the regions of 0.05 K/px, which would still correspond to twice the expected actual temperature gradient, would lead to temperature deviations of about ± 0.1 K due to misalignment.(green markers)

7.4 Influence of Depth of Field (DoF) in Thermography

In the last part of the results chapter, the influence of depth of field (DoF) in thermography on the measurement of temperature fields will be mentioned and discussed.

An optical system such as that used in conventional cameras in the visible range, as well as in cameras in the infrared range, should almost always be able to image a complete field. The imaging of a single point is rather the exception. The consequence of this is that areas in an image are more or less focused. An offset from the focus plane leads to an increasing circle of confusion (CoC) at the sensor plane. Detailed data on the used camera and lens and its field of view (FoV) can be found in the Appendix. From these values, the size of the circle of confusion at the sensor can be calculated with trigonometry and the following equation:

$$\frac{1}{f} = \frac{1}{s_o} + \frac{1}{s_i}$$

With an estimated object distance of approximately 500 mm, a given focal length of 24.6 mm, an offset of 20 mm to the focal plane and a detector pitch of 17 μm produced a circle of confusion diameter of approximately 3 pixel. With an offset of 100 mm from the focus plane, thus with extreme blurriness, a circle of confusion of 18 pixel resulted.

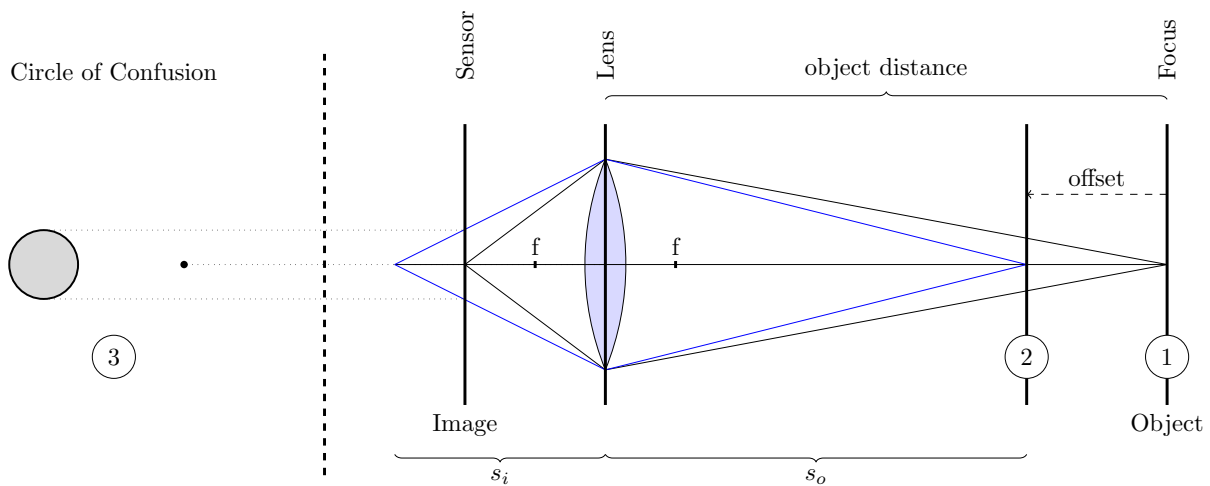


Figure 7.6: Principle of Depth of Field. Object point in full focus (1) and with and offset to the focus plane (2) lead to different circle of confusion (3) at the sensor plane.

Figure 7.7 shows the data evaluations performed to illustrate the just mentioned effect of depth of field and the circle of confusion. Temperature images were compared focussed and not focussed. First of all, it is noticeable that, similar to photography in the visible range, fine structures are strongly blurred. In order to evaluate the effects of DoF in detail, focused and unfocused temperature profiles were recorded along the same line. The lines of interest were intentionally placed over reference points to indicate the same line in the image and to indicate strong gradients.

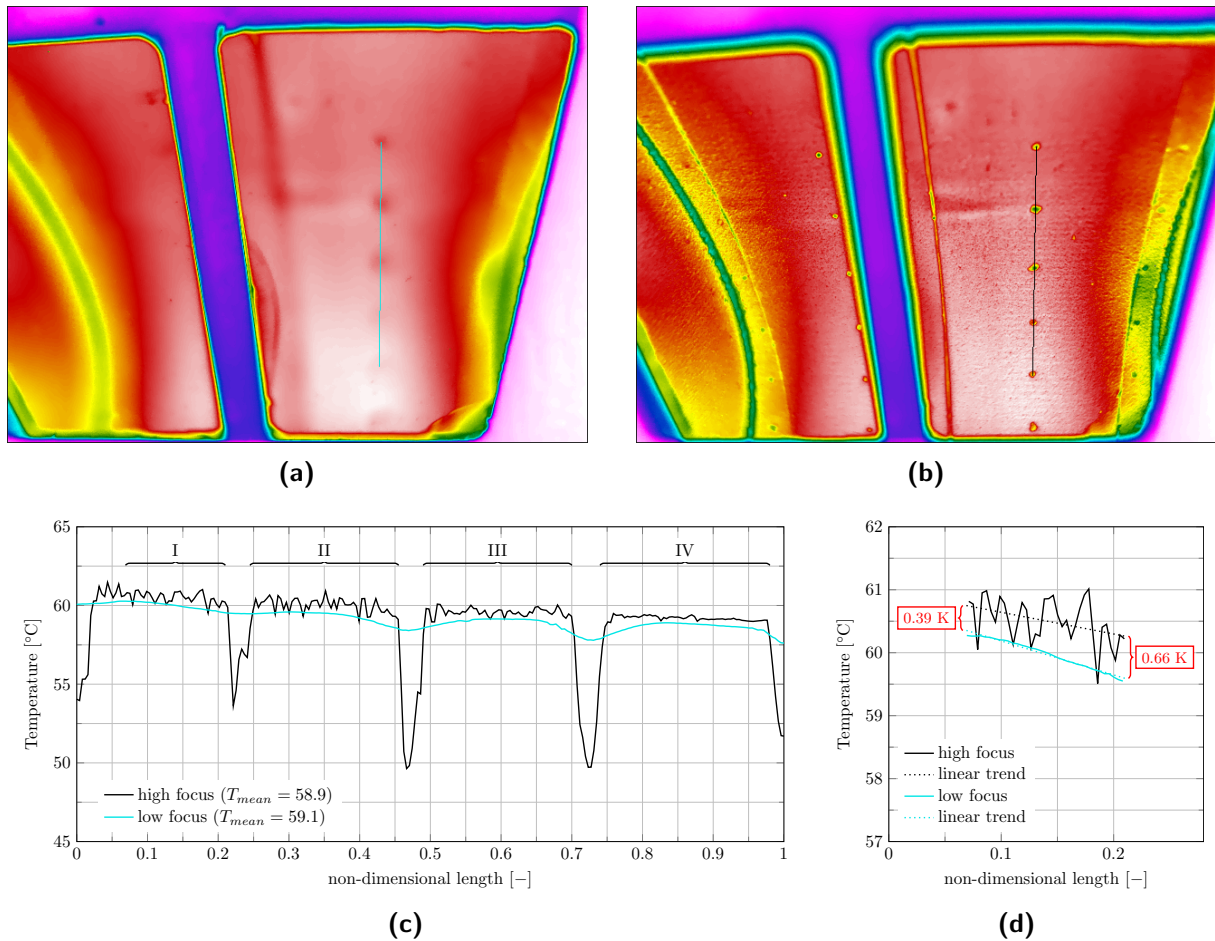


Figure 7.7: Effect of Depth of Focus on Measurement Accuracy. Infrared images with low focus (a) and high focus (b) marked with lines of interest that were investigated. Temperature plot (c) along the marked lines in (a) and (b). Trend lines of the two temperature measurements in region I (d).

Figure 7.7 (c) shows these temperature curves in black and cyan. The temperature peaks in the ranges of the reference points are immediately noticeable. These temperature differences were considered by a different emissivity at the points, in order to be able to detect these also in a thermographic recording.

The blurring appears to act as a low-pass filter. Structures with strong gradients are smoothed. The effect of a decreasing DoF is well illustrated in Figure 7.7 (b). The focal

diameter decreases from bottom to top. This decrease of the focus can also be seen in a decrease of the signal noise in the ranges I to IV. Areas I and II are most strongly focused, fine structures such as the rough surface already discussed in section 7.3 are captured. In region IV this noise is strongly smoothed.

Another important effect is the general offset (decrease) of the signal amplitude when no optimal focusing is possible. Figure 7.7 (d) shows region I in detail, a trend line was calculated from both temperature plots. The result of this detailed consideration is a decrease in temperature with a decrease in sharpness of focus. The two images show extreme values between perfectly focused and totally unfocused. In this example, unfocused images underestimate the mean temperature by 0.39 to 0.66 K.

8 Conclusion and Outlook

Throughout this thesis, a concept for the measurement of temperature fields in a TCF was developed. The feasibility study of this work included the construction of a test bench for the realization of experiments, the development of postprocessing concepts for the thermographic measurement data and the estimation of influencing factors. The work was carried out together with a research partner, whereby the ongoing development process was constantly communicated through regular telephone conferences and meetings.

The installed test rig provides a simplified hands-on model to obtain experience in thermographic temperature capture methods under near engine realistic operation conditions regarding the geometry and limited optical access. The choice of materials, coatings and instruments used can be validated and modified for further investigations.

Figure 8.1 shows a generated temperature field, which represents a concluded result of this work. This temperature field is the basis for determining the required parameters such as heat transfer and film cooling effectiveness of the TCF for continuing applications. The feasibility of temperature measurements in the defined measuring region using several images has been shown, however, the limitations of this method should now be addressed:

Because the DLT algorithm is an approximation method, the mapping quality depends significantly on the quality of the images. The first possible source of error is the manual definition of the reference points (described in section 5.1.1). Since each individual reference point has to be defined by hand, utmost caution is required. An incorrectly assigned reference point or sloppy detection of the points quickly lead to very distorted transformations and thus to an inappropriate result. Particularly with few reference points (only just above the minimum of six in the image) and with very steep camera angles, caution is required. Indicator for the quality of each single image is the reprojection error. In addition, camera parameters with heavily modified estimates also indicate a poor transformation.

The experiments have shown that problems can occur with the mapping of the measurement images, especially in the front (Figure 8.1, I) and rear (Figure 8.1, IV) areas of the measurement field, which are difficult to access and the number of visible reference points is low.

The influence of the spatial error by the mapping algorithm on the temperature measurement was estimated in section 7.3. In region III the accessibility is optimal and the probability of bad projections is low. In addition, low temperature gradients occur at the

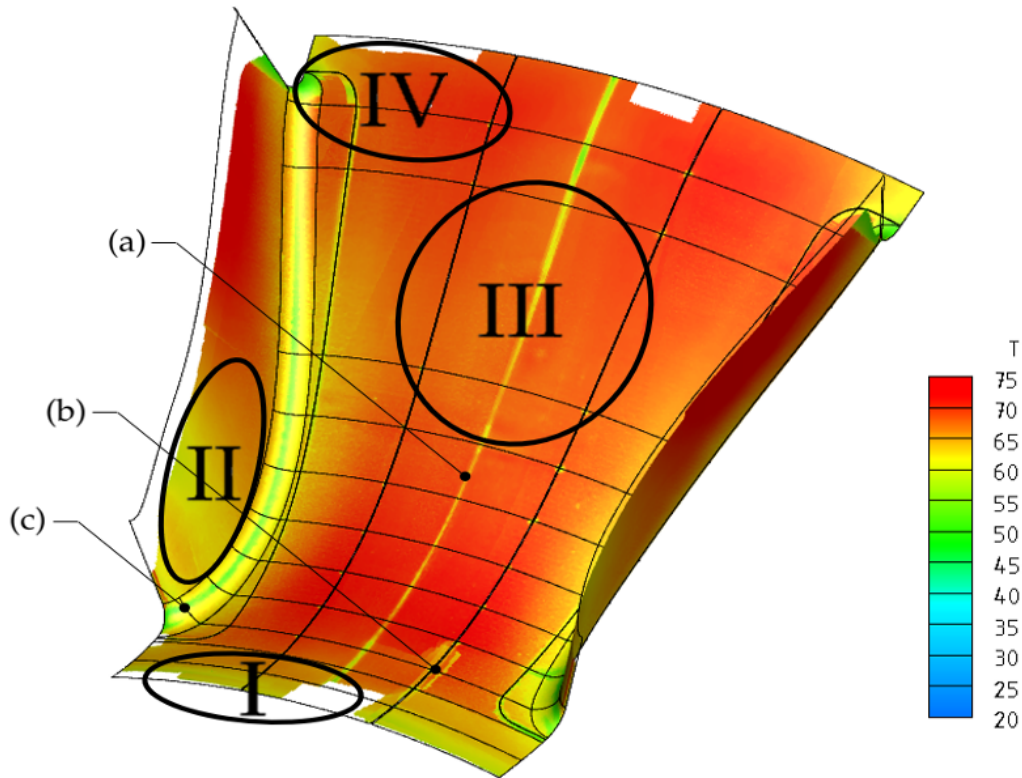


Figure 8.1: Temperature distribution TCF geometry. (Temperature scale in Celsius); I-IV Regions of interest; (a)&(c) Unusable temperature structures due to the joints of the heating foils; (b) Error due to overlapping multiple images

TCF hub in this region. The effects on the temperature measurement are below $\pm 0.1K$. In the area I and IV there are higher reprojection errors due to steep camera angles. Error estimations in these ranges will lead to values of influencing factors of $\pm 0.3K$ due to higher reprojection errors. In area II, the influence of the spatial error is certainly strongest, since on the one hand the temperature gradients and on the other hand the reprojection at the steep side walls are highest. Nevertheless, the post-processing of the 2D images can reduce the predicted influence of up to $\pm 0.6K$ to the required $\pm 0.1K$.

Additionally, the positions and number of the attached reference points should also be discussed once again, especially on the side walls of the struts, additional reference points would positively influence the transformation.

A further point that emerged from the tests is the necessary post-processing of the generated temperature field. Filters for the overlapping of several images (Figure 8.1, (b)) and the removal of incorrectly measured temperatures in the area of the reference points and the joints of the foils (Figure 8.1, (a)(c)) should be considered.

The feasibility of the measurement using heated foils on the surface was proven, but improvements in the design of the foils are quite plausible. On the one hand, the uniformity of the introduced heat flux and, on the other hand, the maximum performance of the introduced foils should be discussed again in order to increase the measurement accuracy.

All experiences gained from this thesis will be used for the realisation of a future planned measurement campaign at the TTTF Rig at the Technical University of Graz and shared with the research partner. Important conclusions regarding geometry preparation, measurement instrumentation and measurement procedures can be planned more efficiently.

Within the context of an ongoing dissertation by Patrick Jagerhofer, this work will be continued immediately. At the moment first measurements for publications presented at ASME Turbo Expo 2020 are being carried out in the test rig, which are dedicated to heat transfer in a TCF. Especially the film cooling effectiveness and the heat transfer coefficient in this engine component are of interest. The measured and geometrically assigned temperature fields resulting from this thesis form the basis for further calculations.

Above all, the development of suitable calibrations to increase the measurement accuracy and the time-consuming development of postprocessing algorithms can now be carried out in advance for the planned TTTF measurement campaign.

List of Figures

1.1	World Air Traffic Growth	1
1.2	Global CO ₂ Emission	2
1.3	Modern two-shaft high-bypass turbofan engine GE9X	3
1.4	Modern engine concepts	4
1.5	Conventional Propulsion System Fundamentals	5
2.1	GENx engine	7
2.2	Turbine Center Frame	7
2.3	Schematic initial specification	8
2.4	FLIR TC650SC	10
2.5	Spectral transmission of optical materials.	10
2.6	Structural design of the heater	11
3.1	The electromagnetic spectrum	15
3.2	Spectral radiation emittance	17
3.3	Reflection, absorption and transmission	18
3.4	Spectral radiant emittance of three types of radiators	18
3.5	General thermographic measurement situation	19
3.6	Pinhole camera geometry	21
4.1	Checkerboard pattern	27
4.2	Checkerboard pattern for Camera Calibration	27
4.3	Camera Calibration Tool	28
4.4	Directional observation	31
5.1	Block diagram of software concept	33
5.3	Reference points	35
5.4	MATLAB user interface	35
5.5	Surface geometry and generated mesh	36
5.6	Summary of the transformation algorithm	37
5.7	Transformation process	38
5.8	Export for Tecplot	39
6.1	Block diagram of the test bench concept	40
6.2	Given geometry	42
6.3	Geometry prepared for rapid prototyping	43

6.4	Adaptations strut geometry	44
6.5	Defined mounting	44
6.6	Standard nominal flow rate	45
6.7	Cavity replication	46
6.8	Cross-section of the purge air guidance system	46
6.9	Inlet nozzle mesh	47
6.10	Velocity profiles	48
6.11	Inlet nozzle sheet metal construction	49
6.12	Outlet	49
6.13	3D printed TCF geometry.	50
6.14	Heating foils	51
6.15	Reference Points on the coated TCF geometry	52
6.16	Measurement of the actual point coordinates	52
6.17	Assembled and connected test rigons	52
6.18	Test rig cross section	53
6.20	Test rig CAD sketch with basic dimensions	55
6.21	Thermocouple positions	56
6.22	Block Calibrator	57
6.23	Five-hole probe measurement position	59
7.1	Data visualisation of IR images	61
7.2	Significant areas of the merged temperature field.	62
7.3	Reprojection Error	64
7.4	Occuring Temperature Gradients	66
7.5	Teperature error caused by misalignment of the provided mapping algorithm	67
7.6	Principle of Depth of Field	68
7.7	Effect of Depth of Focus on Measurement Accuracy	69
8.1	Temperature distribution TCF geometry	72

List of Tables

1.1	Modern engine concepts	4
2.1	Camera specifications	9
6.1	Specifications of printing materials	43
6.2	Measurement of reference points	51
7.1	Operating conditions of test rig	60
7.2	Transformation quality	63

References

- [1] Tommaso Astarita and Giovanni Maria Carlomagno, *Infrared Thermography for Thermo-Fluid-Dynamics*. 2013, ISBN: 978-3-642-29507-2.
- [4] Willy J. G. Bräunling, *Flugzeugtriebwerke: Grundlagen, Aero-Thermodynamik, ideale und reale Kreisprozesse, thermische Turbomaschinen, Komponenten, Emissionen und Systeme*, ser. VDI-Buch. Berlin: Springer Vieweg, 2015, ISBN: 978-3-642-34539-5.
- [16] Richard Hartley and Andrew Zisserman, *Multiple View Geometry in Computer Vision*. 2nd ed. West Nyack: Cambridge University Press, 2004, OCLC: 1044713766, ISBN: 978-0-511-18618-9.
- [26] Eric Tang Kwor and Simone Matte, “Emissivity measurements for nextel velvet coating”, presented at the 15th European Conference on Thermophysical Properties, vol. 33, Würzburg, Germany, 1999, pp. 1087–1092. DOI: [10.1068/htwu385](https://doi.org/10.1068/htwu385).
- [27] G.E. Moore, “Cramming more components onto integrated circuits”, in *Proceedings of the IEEE*, vol. 86, 1998, pp. 82–85. DOI: [10.1109/JPROC.1998.658762](https://doi.org/10.1109/JPROC.1998.658762).
- [37] Stefan von Hoesslin, Martin Stadlbauer, Juergen Gruendmayer, and Christian J. Kähler, “Temperature decline thermography for laminar–turbulent transition detection in aerodynamics”, in *Experiments in Fluids*, vol. 58, 2017. DOI: [10.1007/s00348-017-2411-1](https://doi.org/10.1007/s00348-017-2411-1).
- [38] William L. Wolfe, *The infrared handbook*. ERIM, 1993, ISBN: 978-0-9603590-1-1.
- [39] Stefan Zerobin, “Aerodynamic performance of turbine center frames under the presence of high-pressure turbine rotor purge flows”, PhD thesis, Graz University of Technology, Graz, 2018, 174 pp.

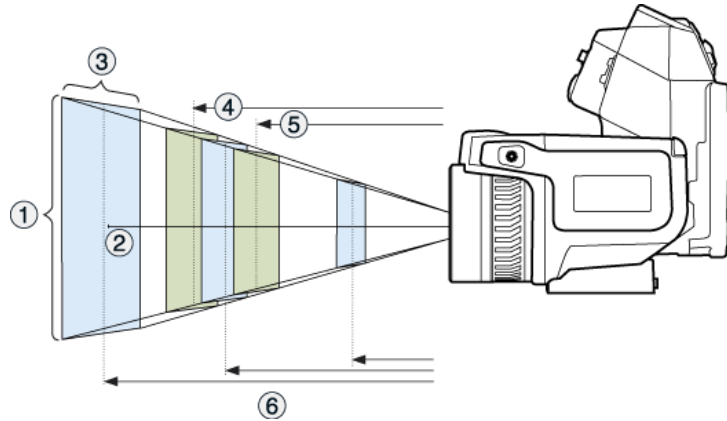
Online Sources

- [2] ATMmasterplan. (2019). SESAR — eATM portal, atmmasterpan.eu, [Online]. Available: <https://www.atmmasterplan.eu/> (visited on 11/04/2019).
- [3] GE Aviation. (2013). Ge9x_airflow, aibonline.com, [Online]. Available: https://www.aibonline.com/sites/default/files/uploads/2014/08/ge9x_airflow-2013.jpg (visited on 08/24/2019).
- [5] CleanSky. (2019). Welcome to the clean sky — clean sky, cleansky.eu, [Online]. Available: <https://www.cleansky.eu/> (visited on 08/21/2019).
- [6] Bundesministerium für Wirtschaft und Energie. (2019). Luftfahrtforschungsprogramm (LuFo), bmwi.de, [Online]. Available: <https://www.bmwi.de/Redaktion/DE/Artikel/Technologie/luftfahrttechnologien-02.html> (visited on 11/03/2019).
- [7] Alan Epstein. (2015). The pratt & whitney PurePower geared turbofan engine, [Online]. Available: <https://academieairespace.com/wp-content/uploads/2018/05/prattw.pdf>.
- [8] ESEA. (2019). EASA.e.110 — LEAP-1a & LEAP-1c series engines, esea.europa.eu, [Online]. Available: <https://www.easa.europa.eu/documents/type-certificates/engine-cs-e/easae110> (visited on 08/25/2019).
- [9] —, (2019). EASA.IM.e.093 — PW1100g-JM series engines, esea.europa.eu, [Online]. Available: <https://www.easa.europa.eu/documents/type-certificates/engine-cs-e/easaime093> (visited on 08/25/2019).
- [10] Extrudr. (2019). GREENTEC PRO natur, extrudr.com, [Online]. Available: https://www.extrudr.com/de/produkte/catalogue/green-tec-pro-natur_2286/ (visited on 09/12/2019).
- [11] FAA. (2019). Modernization of u.s. airspace, faa.gov, [Online]. Available: <https://www.faa.gov/nextgen/> (visited on 11/04/2019).
- [12] Festo. (2018). One way flow control valves GR GRA, festo.com, [Online]. Available: https://www.festo.com/cat/xdki/data/doc_engb/PDF/EN/GRX-VFOI_EN.PDF (visited on 09/11/2019).
- [13] Flir. (2019). FLIR t650sc high resolution handheld infrared camera — FLIR systems, flir.com, [Online]. Available: <https://www.flir.com/products/t650sc/> (visited on 05/14/2019).
- [14] —, (2019). Thermal imaging for r&d / science applications, flir.com, [Online]. Available: http://www.nbn.at/fileadmin/user_upload/Vertretungen/FLIR/T1030sc/RND_004_EN_nbn.pdf (visited on 04/22/2019).

- [15] Formlabs. (2018). Material data sheet, formlabs-media.formlabs.com, [Online]. Available: https://formlabs-media.formlabs.com/datasheets/High_Temp_Technical.pdf (visited on 09/12/2019).
- [17] Patrick Hoeveler. (2019). In the middle: The turbine center frame for large aircraft engines, aeroreport.de, [Online]. Available: <https://aeroreport.de/en/innovation/in-the-middle-the-turbine-center-frame-for-large-aircraft-engines> (visited on 08/24/2019).
- [18] ICAO. (2019). Air transport, passengers carried — data, worldbank.org, [Online]. Available: <https://data.worldbank.org/indicator/IS.AIR.PSGR> (visited on 05/22/2019).
- [19] —, (2019). Air transport, registered carrier departures worldwide — data, worldbank.org, [Online]. Available: https://data.worldbank.org/indicator/IS.AIR.DPRT?end=2017&most_recent_value_desc=true&start=1970&type=points&view=chart&year=2013 (visited on 05/23/2019).
- [20] —, (2019). Carbon offsetting and reduction scheme for international aviation (CORSIA), icao.int, [Online]. Available: <https://www.icao.int/environmental-protection/CORSIA/Pages/default.aspx> (visited on 08/21/2019).
- [21] —, (2019). CO2 emissions (kt) — data, worldbank.org, [Online]. Available: <https://data.worldbank.org/indicator/EN.ATM.CO2E.KT?contextual=default> (visited on 05/23/2019).
- [22] —, (2019). ICAOEnvironmental, icao.int, [Online]. Available: https://www.icao.int/environmental-protection/Documents/ICAOEnvironmental_Brochure-1UP_Final.pdf (visited on 05/23/2019).
- [23] Infratec. (2019). Branchen & Applikationen, www.infratec.de, [Online]. Available: <https://www.infratec.de/thermografie/anwendungsgebiete/> (visited on 05/05/2019).
- [24] CFM international. (2019). CFM LEAP, evolution.skf.com, [Online]. Available: <http://evolution.skf.com/wp-content/uploads/2016/11/16-4-aerospace-fig-9.jpg> (visited on 05/22/2019).
- [25] ITTM. (2019). ITTM - transonic test turbine facility, tugraz.at, [Online]. Available: <https://www.tugraz.at/institute/ittm/capabilities/test-rigs/transonic-test-turbine-facility/> (visited on 08/25/2019).
- [28] MTU. (2019). GENx turbofan engine, mtu.de, [Online]. Available: https://www.mtu.de/fileadmin/DE/7_News_Media/2_Media/Broschueren/Engines/GENx.pdf (visited on 09/12/2019).

- [29] —, (2019). PW1000G, mtu.de, [Online]. Available: <http://www.mtu.de/de/engines/zivile-triebwerke/narrowbody-and-regional-jets/gtf-triebwerksfamilie/> (visited on 05/22/2019).
- [30] Romain Muller and Patricia Pelfrene. (2010). Creating innovative air transport technologies for europe, acare4europe.org, [Online]. Available: <https://www.acare4europe.org/sites/acare4europe.org/files/document/Create-Final-Report-October-2010.pdf> (visited on 05/23/2019).
- [31] omega. (2019). Users guide block calibrator, omega.com, [Online]. Available: <https://assets.omega.com/manuals/M2890.pdf> (visited on 08/09/2019).
- [32] Philip Ronan. (2007). EM_spectrum, wikimedia.org, [Online]. Available: https://upload.wikimedia.org/wikipedia/commons/f/f1/EM_spectrum.svg (visited on 03/26/2019).
- [33] Scanivalve. (2019). DSA3218-PTP pressure scanner, Scanivalve, [Online]. Available: <http://scanivalve.com/products/pressure-measurement/ethernet-intelligent-pressure-scanners/dsa3218-ntp-pressure-scanner/> (visited on 11/05/2019).
- [34] ShalomEO. (2019). Barium fluoride (BaF₂) windows for thermal imaging applications, shalomeo.com, [Online]. Available: <http://www.shalomeo.com/product/infrared-optics/infrared-windows/baf2-windows-34.html> (visited on 08/09/2019).
- [35] PIKE Technologies. (2019). Choice of window materials for transmission sampling of liquids in the mid-IR spectral region, piketech.com, [Online]. Available: https://www.piketech.com/skin/fashion_mosaic_blue/application-pdfs/CrystalChoiceForTransmission.pdf (visited on 08/09/2019).
- [36] Inc The MathWorks. (2019). Single camera calibrator app - MATLAB & simulink - MathWorks deutschland, mathworks.com, [Online]. Available: <https://de.mathworks.com/help/vision/ug/single-camera-calibrator-app.html> (visited on 10/30/2019).

Field of View Calculator



T650sc. 1: VFOV, 2: IFOV, 3: HFOV, 4: DOF far, 5: DOF near, 6: D

Camera: 55904-7823; FLIR T650sc 25° (incl. Wi-Fi)
 Lens: T197922; IR lens, f=24.6 mm (25°) with case
 Close focus: 250 mm
 Hyperfocal distance: 20.55 m

D	0.30	0.40	0.50	0.60	0.70	
HFOV	0.13	0.18	0.22	0.27	0.31	m
VFOV	0.10	0.13	0.17	0.20	0.23	m
DOF near	0.30	0.39	0.49	0.58	0.68	m
DOF far	0.30	0.41	0.51	0.62	0.73	m
IFOV	0.21	0.28	0.35	0.41	0.48	mm

Legend:

D = Distance to target in meters

HFOV = Horizontal field of view in meters

VFOV = Vertical field of view in meters

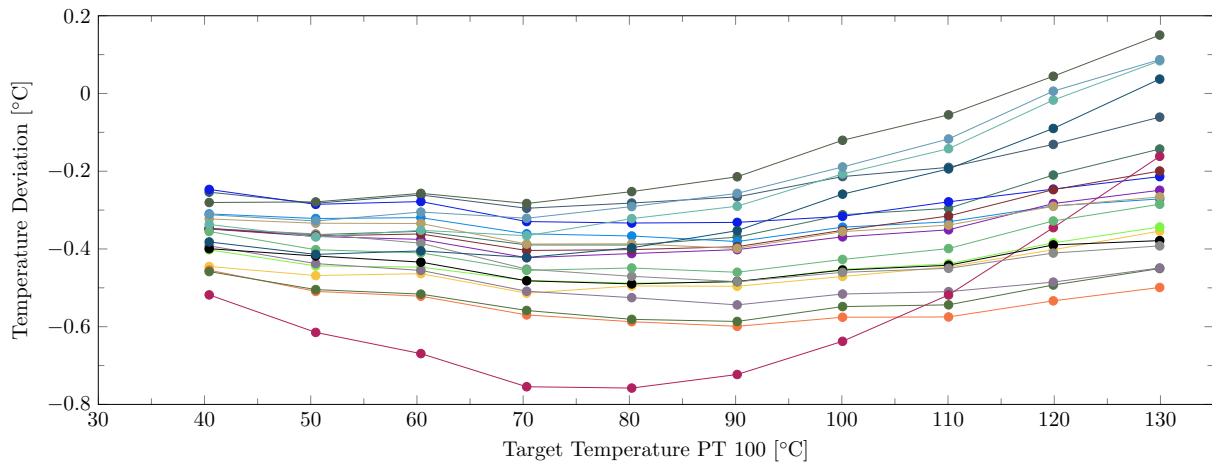
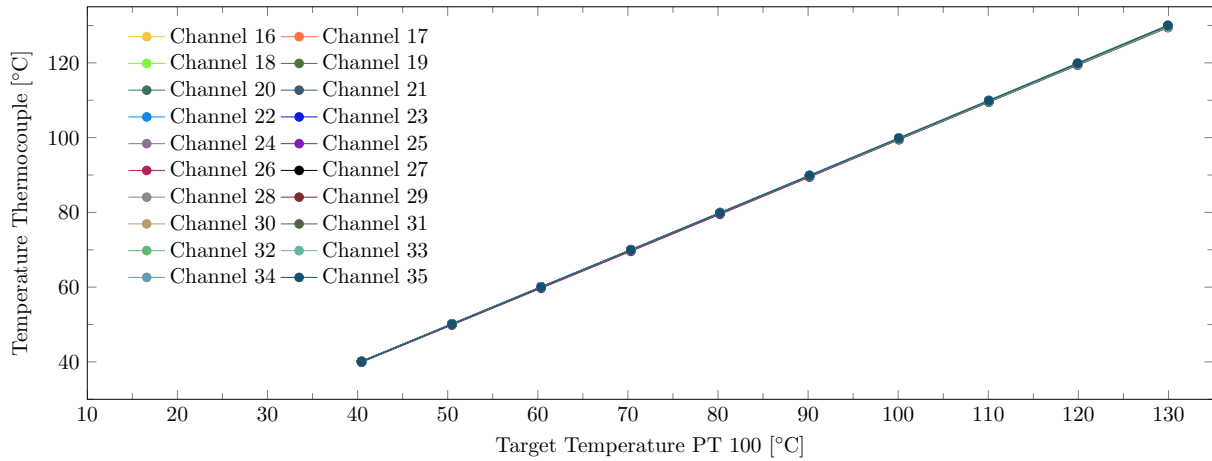
DOF near = Depth of field near limit in meters

DOF far = Depth of field far limit in meters

IFOV = Instantaneous field of view (size of one detector element) in millimeters

https://flir.custhelp.com/app/utils/fl_fovCalc/pn/55904-7823/ret_url/%252Fapp%252Ffl_download_datasheets%252Fid%252F10

Thermocouple Calibration Curves



Thermocouple Calibration. Temperature of each channel at different calibration temperatures (top) and temperature deviation of each channel to the reference PT100 temperature. (bottom)